Systematic Investigation of the Effects of Hydrophilic Porosity on Boiling Heat Transfer and Critical Heat Flux

By

Melanie Tetreault-Friend

B.Eng., Mechanical Engineering
McGill University

SUBMITTED TO THE DEPARTMENT OF NUCLEAR SCIENCE AND ENGINEERING IN PARTIAL FULFILLMENT OF THE REQUIREMENTS FOR THE DEGREE OF

MASTER OF SCIENCE IN NUCLEAR SCIENCE AND ENGINEERING

AT THE

MASSACHUSETTS INSTITUTE OF TECHNOLOGY

SEPTEMBER, 2014

Signature of author: Signature redacted
Melanie Tetreault-Friend
Department of Nuclear Science and Engineering
August 21, 2014

Certified by: Signature redacted
Jacopo Buongiorno
Associate Professor of Nuclear Science and Engineering
Thesis Supervisor

Certified by: Signature redacted
Thomas McKrell
Research Scientist for Nuclear Science and Engineering
Thesis Co-supervisor

Accepted by: Signature redacted
Mujid S. Kazimi
TEPCO Professor of Nuclear Engineering
Department Committee on Graduate Students

Systematic Investigation of the Effects of Hydrophilic Porosity on Boiling Heat Transfer and Critical Heat Flux

By

Melanie Tetreault-Friend

Submitted to the Department of Nuclear Science and Engineering on August 21, 2014 in partial fulfillment for the degree of

MASTER OF SCIENCE IN NUCLEAR SCIENCE AND ENGINEERING

ABSTRACT

Predicting the conditions of critical heat flux (CHF) is of considerable importance for safety and economic reasons in heat transfer units, such as in nuclear power plants. It is greatly advantageous to increase this thermal limit and much effort has been devoted to studying the effects of surface characteristics on it. In particular, recent work carried out by O'Hanley [6] demonstrated the separate effects of surface wettability, porosity, and roughness on CHF, and found that porous hydrophilic surface coatings provided the largest CHF increase, with a 50-60% enhancement over the base case. In the present study, a systematic investigation of the effects that the physical characteristics of the hydrophilic layers have on heat transfer was conducted. Parameters experimentally explored include porous layer thickness, pore size, and void fraction (pore volume fraction). The surface characteristics are created by depositing layer-by-layer (LbL) thin compact coatings made of hydrophilic SiO_2 nanoparticles of various sizes. A new coating was developed to reduce the void fraction by using polymers to partially fill the voids in the porous layers. All test surfaces are prepared on indium tin oxide - sapphire heaters and tested in a pool boiling facility at atmospheric pressure in MIT's Thermal-Hydraulics Laboratory. Results indicate that CHF follows a trend with respect to each parameter studied and clear CHF maxima reaching up to 114% enhancement are observed for specific thickness and pore size values. ZnO_2 nanofluid-generated coatings are also prepared and their boiling performance is compared to the boiling performance of the engineered LbL coatings. The results highlight the dependence of CHF on capillary wicking and are expected to allow further optimization of the nanoengineered surfaces.

THESIS SUPERVISOR: Jacopo Buongiorno, Ph.D.
TITLE: Associate Professor of Nuclear Science and Engineering

THESIS CO-SUPERVISOR Thomas McKrell, Ph.D.
TITLE: Research Scientist for Nuclear Science and Engineering

ACKOWNLEDGEMENTS

I would first like to thank Professor Jacopo Buongiorno for his support, patience, and invaluable input throughout this project. I learned a tremendous amount and I feel privileged to have had him as supervisor.

I would also like to extend my personal gratitude to Dr. Tom McKrell who was an incredibly large resource for all of my experimental work. It was a great joy to work with him over the past two years and I would like to thank him for keeping engineering fun.

Thank you Dr. Hyomin Lee and Rosanna Lim who both guided me throughout my adventures in LbL. They provided numerous suggestions to improve my experiments and were always happy to sit down with me and brainstorm technical issues. Thank you also to Professor Robert Cohen and Professor Michael Rubner giving me access to their labs, for sharing all of their technical knowledge and for their creative insight in developing the nanoengineered surfaces.

A huge thanks to Dr. Shiahn Chen for your support and patience with the FIB and SEM in the CMSE. All your help greatly improved the quality of my work.

I want to acknowledge the Fonds de recherche du Québec – Nature et technologies and the National Sciences and Engineering Research Council of Canada for their financial support through their graduate research fellowship programs, and to Areva NP for their financial and technical support for this project.

I owe a special thanks to the members of my research group and of the Green Lab including Guanyu Su, Carolyn Coyle, Andrew Richenderfer, Matteo Bucci, Reza Azizian, Bren Phillips, and Eric Forrest. I am grateful to have had such a fantastic group to work with. Thanks to you, I will always remember not to pour liquid nitrogen in my ears or drink the nanofluids.

I must thank Helen Liu for being such an exceptional UROP and exceeding all of my expectations. Your help and assistance in my experimental work was greatly appreciated. I wish you all the best in your continuation at MIT and with all your future endeavors.

Thank you Professor John Lee. You taught me the fundamentals and inspire me to always keep learning.

Finally, a special thanks to my brother Michael for inspiring me to become an engineer. Thank you mom for supporting me throughout all of my crazy endeavors over the years and always believing in me. And last but certainly not least, thank you Xavier. An entire thesis would not fully express my appreciation for the love and support you have given me.

Table of Contents

LIST OF FIGURES

LIST OF TABLES

1. Introduction

1.1. Motivation

Boiling is an effective heat transfer mechanism due to its large amount of energy removal capabilities from latent heat of vaporization and enhanced mixing. It is therefore a common heat transfer mechanism in a wide variety of applications such as electronic devices, refrigeration systems, pipe stills, water-cooled nuclear reactors and fossil power plants. The interaction of the fluid with the interface affects the heat transfer performance. Hence, the surface can be engineered to achieve enhanced performance. In addition, boiling is limited by some upper limit value known as critical heat flux (CHF). CHF marks the point at which liquid supply to the heat transfer surface is restricted by the establishment of a continuous vapor film on the surface [1]. CHF is the value of the heat flux at which the transition from nucleate boiling to film boiling occurs. Beyond this point, the surface temperature dramatically increases, for a given heat flux. Film boiling is undesirable because the significant temperature increase can severely weaken or damage the surface material. For nuclear reactor applications, increasing the CHF value allows to increase the safety margins or safely operate at higher power densities, ultimately leading to better economics for electricity generation [2]. It is therefore advantageous to increase this thermal limit.

The second most important figure of merit for the heat transfer surface is the heat transfer coefficient (HTC), which characterizes the convective heat transfer from the surface to the fluid. It is the ratio of the heat flux to the temperature difference between the heat transfer surface and the boiling fluid. It is an important parameter in determining the effectiveness of the heat transfer surface.

Extensive work has been carried out to investigate the effects of surface characteristics on CHF by modifying surfaces using various chemical or mechanical treatments and subsequently testing them in pool boiling experiments. Studies investigating the effects of roughness date back as early as 1931 [3]. More recently, Wang [4] studied the effects of microstructured surfaces with a wide range of well-defined surface roughnesses on CHF in pool boiling experiments. Other studies have involved nanofluid boiling to create nanoporous layers on heat transfer surfaces. In such cases, nanoparticles are added to a fluid in low concentrations to create a nanofluid. During nucleate boiling, the nanoparticles in the nanofluid randomly deposit onto the surface. The resulting porous coating has been associated with significant CHF enhancement of up to 200% [5].

Despite the numerous investigations which have been carried out, the effects of surface features on CHF are still not fully understood and engineers and scientists have not yet come to a general consensus on the topic. Conflicting results have even been observed in some instances. It has been reported that porous deposits on heat transfer surfaces both enhance and decrease CHF [1]. In most cases, observations have been made and general trends have been deduced, but the exact underlying physical mechanisms have not been fully elucidated and CHF enhancement cannot be accurately predicted and quantified.

1.2. Objectives

Previous work carried out by O'Hanley [6] demonstrated the separate effects of surface wettability, porosity, and roughness on CHF and HTC. Porous hydrophilic surfaces were determined to be the most successful surfaces at enhancing CHF. The objective of this research is to further conduct a systematic study of the effects of porous layer thickness, pore size, and porosity (pore volume fraction) on CHF and HTC. This research will yield additional insight into the effects of surface characteristics on CHF and HTC, and also allow for further optimization of the engineered surfaces.

2. Background and Previous Research

In this chapter, the fundamental theory of boiling relevant to this research is reviewed. An overview of various surface engineering techniques for CHF enhancement and their results are presented. The basic concepts of layer-by-layer deposition, the surface engineering technique used in the present study, are explained along with some pertinent applications for this investigation.

2.1. Boiling Heat Transfer

2.1.1. Boiling Nucleation Theory

Vapor formation occurs at an interface when the liquid temperature is above the saturation temperature. This temperature difference is known as liquid superheat. For vapor nucleation to take place, certain superheat requirements must be satisfied. Beginning with mechanical equilibrium of a vapor nucleus, we find that

$$p_g - p_f = \frac{2\sigma}{r^*} \tag{2.1}$$

where p_g is the vapor pressure inside the vapor nucleus, p_f is the fluid pressure corresponding to the saturation temperature T_{sat}, σ is the surface tension, and r^* is the radius of the nucleus. The corresponding liquid superheat is given by

$$(T_g - T_{sat}) = \Delta T_{sat} = \frac{RT_gT_{sat}}{Jh_{fg}M} ln\left[1 + \frac{2\sigma}{p_f r^*}\left(1 + \frac{v_f}{v_g}\right)\right] \tag{2.2}$$

Where M is the molecular weight, R is the universal gas constant, J is the mechanical equivalent of heat, h_{fg} is the latent heat of vaporization, T_g is the vapor temperature, v_f is the liquid specific volume, and v_g is the vapor specific volume. Nucleation may occur either homogeneously or heterogeneously. In the case of homogeneous nucleation, clusters of vapor molecules must agglomerate in the homogeneous liquid to form a vapor nucleus of the size of the critical radius. On the other hand, heterogeneous nucleation occurs when foreign materials are present and act as preferential sites for vapor formation. In particular, we consider heterogeneous nucleation at solid surfaces. The Gibbs free energy of formation $\Delta G(r^*)$ is reduced by a factor φ in the presence of a

flat surface. Heterogeneous nucleation is therefore energetically more favorable than homogeneous nucleation for a given superheat. The factor φ is a function of the liquid contact angle θ [7-8] and is given by the expression

$$\varphi = \frac{2 + 2cos\theta + cos\theta sin^2\theta}{4} \tag{2.3}$$

where the contact angle θ characterizes the wettability of a surface, i.e. the degree of contact of the fluid with the surface as illustrated in Figure 2-1.

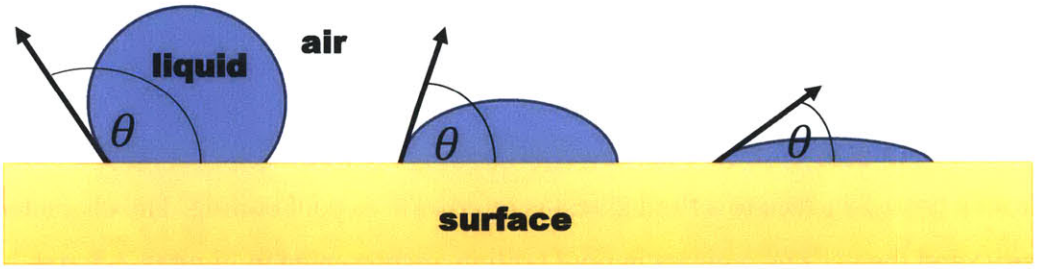

Figure 2-1 Liquid droplets on a flat surface with varying degrees of wettability.

From Eq. 2.3, we see that if $\theta = 0$ (completely wetting), $\varphi = 1$ and there is no reduction in the free energy of formation. If the surface is completely non-wetting then $\theta = 180°$, $\varphi = 0$, and no superheat is required for nucleation. A high wettability therefore deactivates the nucleation sites on the heat transfer surface and decreases the boiling heat transfer coefficient. Wettability plays an important role in boiling efficiency.

However, the superheats required in practice are much lower than those expected from the reduction of the free energy at a solid surface. The reason for this is due to the presence of pits and cavities in the surface. These defects significantly reduce the energy required to create a stable vapor bubble and serve as nucleation sites (Fig. 2-2). Typically, a small gas pocket will be contained within a cavity on the heat transfer surface and will grow a vapor bubble which will then detach and carry away a large amount of heat through agitation, evaporation, and removal of the thermal boundary layer. This type of heterogeneous nucleation only requires a few degrees of surface superheat for the onset of nucleate boiling (ONB). Typically, the nucleation sites are on the order of 0.1-10μm. Furthermore, these microcavities affect the surface heat flux for a given

wall superheat, i.e. the heat transfer coefficient. In certain cases, surface characteristics may increase the minimum film boiling temperature due to the increase in surface roughness and wettability [9].

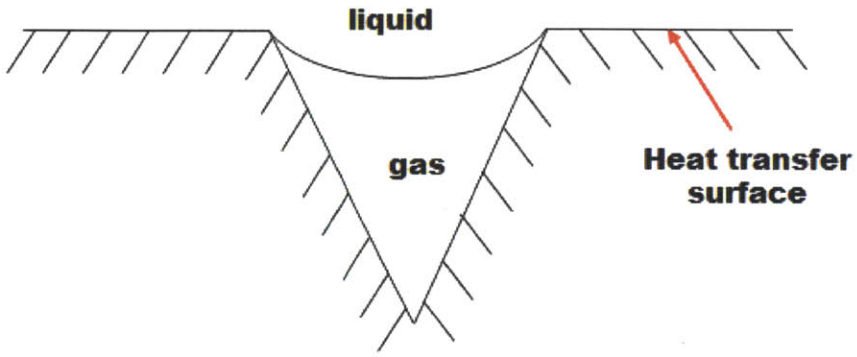

Figure 2-2 Active nucleation site with trapped gas

2.1.2. Pool Boiling

Boiling from a heated surface to a fluid at rest is referred to as pool boiling. The characteristic pool boiling curve and the various regimes in pool boiling are presented in Figures 2-3 and 2-4. At low heat fluxes below point A in Figure 2-3, heat transfer to the fluid occurs via natural convection.

Heat flux and temperature will increase until the onset of nucleate boiling occurs at point A. Between points A and B, bubbles form and detach from the surface under the effect of buoyancy, removing a more significant amount of heat due to the large heat of vaporization required for phase change.

As the surface temperature is further increased, boiling occurs more vigorously, until the unstable transition boiling regime is reached at point C. Large vapor pockets are generated at the surface and the heat transfer coefficient drops dramatically due to the low thermal conductivity within the vapor layer. At this point, the vapor layer will collapse as the heat flux is reduced and the surface will be rewetted until the temperature at the surface is sufficiently increased for stable film boiling to occur.

The film boiling regime occurs when a stable vapor film covers the surface. Vapor is released at regular intervals from the vapor film in the form of large bubbles. At this point, heat transfer is mainly achieved by convection and radiation through the vapor film.

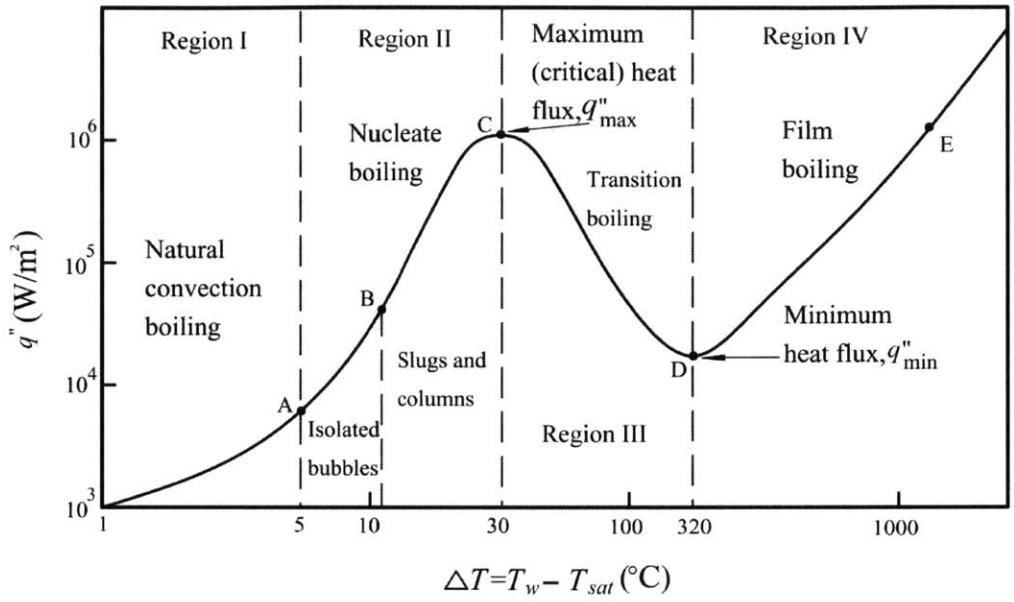

Figure 2-3 Characteristic pool boiling curve. Adapted from Thermal-Fluids Central [10].

As previously discussed, nucleation sites play a crucial role in boiling heat transfer. This implies that heat transfer correlations are surface-dependent. Accurately characterizing surfaces is highly complex, which has made the task of developing theoretical correlations describing nucleate boiling problematic. Rohsenow proposed the dimensionless relationship [1]

$$Nu = \frac{1}{C_{sf}} Re^{(1-n)} Pr^{-m} \tag{2.4}$$

Where the Nusselt Number $Nu = hL/k$ is the ratio of the convective to the conductive heat transfers for some characteristic length L, where h is the heat transfer coefficient and k is the thermal conductivity. Many possible characteristic parameters could be chosen to fit the dimensionless relationship. For example, Rohsenow chose the superficial liquid velocity towards the surface for the Reynolds number. This gives an expression relating the heat flux, the wall superheat, and the fluid properties:

$$\frac{c_{pf}\Delta T_{sat}}{h_{fg}} = C_{sf}\left[\frac{q''}{\mu_f h_{fg}}\left(\frac{\sigma}{g(\rho_f - \rho_g)}\right)^{1/2}\right]^n \left[\frac{c_p \mu}{k}\right]_f^{m+1} \tag{2.5}$$

The constant C_{sf} depends on the liquid surface combination. It is generally recommended to carry out pool boiling experiments for each specific application in order to determine an appropriate value for C_{sf}. Alternatively, tabulated values exist for common liquid surface combinations. Empirical correlations such as the one presented in Eq. 2.5 carry large uncertainties. [11].

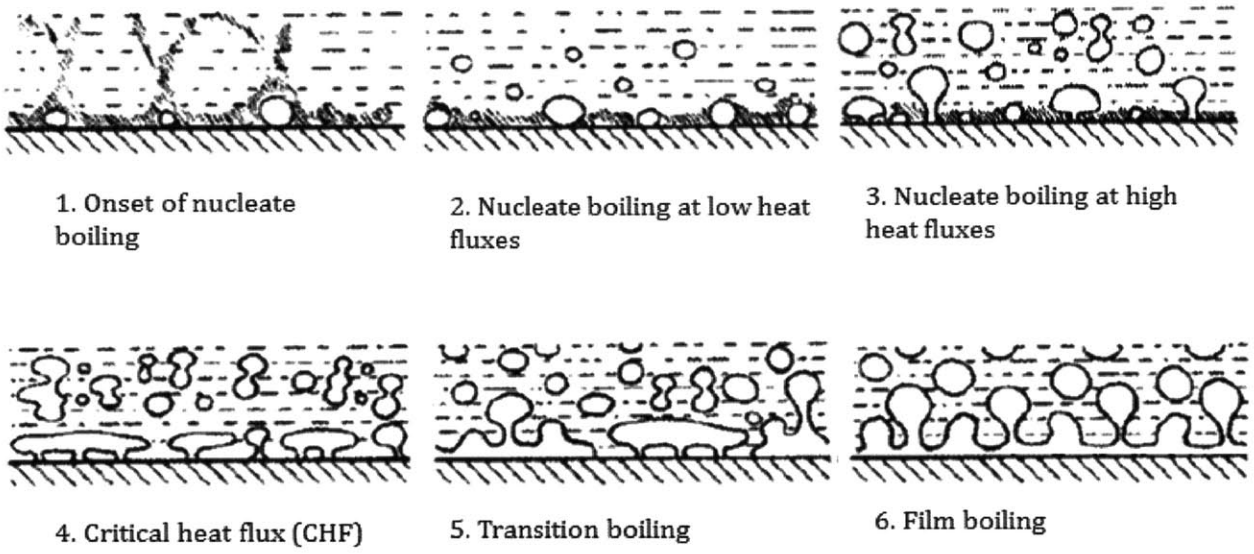

Figure 2-4 Pool boiling regimes. Adapted from Collier [1]

2.1.3. Critical Heat Flux

The full boiling curve presented in Figure 2-3 can only be obtained in experiments where the temperature of the heat transfer surface can be controlled. However, it is generally more common to control the heat flux through the surface than it is to control the temperature. In such cases, if the heat flux remains unchanged or is further increased beyond point C, the location of CHF on the boiling curve, the path followed on the boiling curve will transition directly from point C to E, skipping transition boiling completely. This implies that the temperature of the surface suddenly jumps from approximately ~130°C to >1000°C. This sudden temperature increase causes catastrophic material failure in most cases.

The underlying CHF mechanism has not been fully elucidated. However, it has been linked to significant vapor coverage of the heat transfer surface, suspending the liquid above it and preventing the surface from being rewetted [9], as shown in Figure 2-4. Zuber developed an

idealized model in which adjacent vapor jets form Helmholtz instabilities which interact and limit the vapor flux from the surface [1]. He obtained an expression to predict the CHF value

$$q''_{crit} = Kh_{fg}\rho_g^{1/2}[\sigma g(\rho_f - \rho_g)]^{1/4} \tag{2.6}$$

Where the coefficient $K = \pi/4$ and q''_{crit} depends only on the fluid properties. However, this analysis only holds for pure non-metal liquids on large well-wetted horizontal upward facing surfaces. It is therefore limited to very specific cases since the geometry and surface characteristics will alter the value of q''_{crit}. Models subsequently developed therefore attempt to integrate the effects of surface characteristics to obtain more accurate results and further elucidate the underlying physics describing CHF.

Polezhaev and Kovalev developed a model which accounts for the effects of porosity on CHF. It is a semi-empirical model expanding on Zuber's work. During boiling, the working fluid above the porous coating is drawn in via capillary forces to the bottom of the porous layer along the narrow channels. Vapor formed by phase change is released through larger channels and the vapor and liquid inside the porous coating flow countercurrently. Heat flows from the wall through the porous structure to the meniscus of the liquid. Vaporization therefore takes place inside the porous layer from the surface of stationary menisci. The structure is idealized as a system of cylindrical capillaries with ideal cohesion. The expression obtained is

$$q_{CHF} = 0.52\varepsilon^{2.28}h_{fg}\left[\frac{\sigma\rho_f\rho_g}{(\rho_f + \rho_g)R_{bg}}\right]^{1/2} \tag{2.7}$$

Where ε is the porosity in the layer, and R_{bg} is the breakthrough radius determined experimentally. It is important to note that this model does not account for wettability effects on the surface. O'Hanley [6] provides a thorough review of relevant models which account for wettability and/or roughness.

2.2. Surface Characteristics

2.2.1. Porosity

Porosity (void fraction) is a measure of the empty space in a material and is defined as the volume of the voids to the total volume in the material. There exist various packing arrangements for spheres, each having different porosities. For example, the lowest theoretically achievable porosity for monodispersed spheres (spheres of identical size) is given by

$$1 - \frac{\pi}{3\sqrt{2}} \approx 0.260$$

Two regular lattice arrangements will yield this void fraction. They are face-centered cubic (fcc) and hexagonal close-packed (hcp). For any other type of packing arrangement, the porosity will be higher than this limiting value. Several models exist which describe the various types of close sphere packing. For example, very loose random packing will give a porosity 0.44, and poured random packing will be around 0.375 to 0.391. For a bi-modal distribution of spherical particles, this number can go down to 0.1-0.15. For a fully polydisperse system, the porosity will approach zero because in the limit of full polydispersion, there should always be a particle small enough to fill the gap between two larger particles.

If a given packing method or manufacturing process is performed consistently and is readily repeatable, the resulting void fraction should remain constant when averaged over a sufficiently large region. In addition, for the same packing method, the porosity will remain the same for monodispersed distributions of different particle sizes. This means that a porous coating containing 1 μm particles will have the same porosity as a porous coating containing 50 μm particles if they are both packed the same way. This concept is fairly simple but may appear counterintuitive at first. We can compare this idea to packing cubes of different sizes in a regular lattice such that the void fraction is 50% (Figure 2-5). If we reduce the size of the cubes, they will still occupy 50% of the total volume.

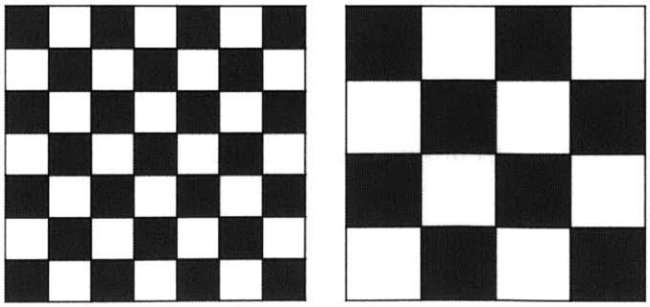

Figure 2-5 Illustration demonstrating a constant void fraction of 50% for two different cube sizes arranged in a regular lattice.

Porous-layer coatings have been associated with significant CHF enhancements. Liter and Kaviany [11] attribute this enhancement to a combination of effects such as the extended

surface area, the capillary wicking which draws the liquid down to the surface, and the pore distribution which affects the vapor escape paths. In general, it is agreed that the liquid supply and vapor escape occur in counterflow through the porous layer. When the heat flux is increased, the liquid supply rate must increase to accommodate the increase in evaporation. They are limited by the liquid and vapor flow resistances within the pores, which consequently imposes a limit on the CHF value in any evaporating system. They note however that due to the high complexity of the phase-change processes in the porous structure, no analytical models have accurately captured these processes under such conditions without using several empirical constants.

O'Hanley et al. [12] identified a set of governing variables assuming that the effects of surface features are driven by capillary wicking. They determined that the governing π-groups are ε and β themselves, the ratio D_p/L, and the pore Reynolds number

$$Re_p \equiv \frac{\rho_f \sigma D_p}{\mu_f^2}, \tag{2.8}$$

where ε is the void fraction, D_p is the effective pore diameter, L is the effective pore length, β is the intrinsic contact angle , σ is the surface tension, μ_f is the fluid viscosity, and ρ_f is the fluid density. They believe a suitable form for a CHF model or correlation should account for these parameters.

2.2.2. Roughness

Surface roughness characterizes the texture of a surface. It is a measure of the vertical deviations of a surface from an ideal, smooth surface. Roughness has been associated with significant CHF enhancements and extensive research on this effect has been carried out as early as 1960 by Berenson [17]. There exist several parameters to quantify these deviations. One-dimensional parameters include the arithmetic average roughness R_a, the root mean squared of the arithmetic average R_{rms}, and the average distance between the highest peak and the lowest valley R_z. In the present investigation, we restrict our measurements to R_a, defined mathematically as

$$R_a = \frac{1}{L}\int_0^L |z(x)|dx$$

and illustrated in Figure 2-6. *z(x)* is the vertical distance from the mean *M*, and *L* is the distance over which roughness is measured.

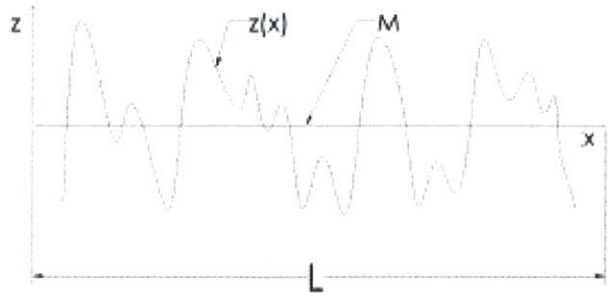

Figure 2-6 Arithmetic average roughness R_a. Adapted from O'Hanley [6].

2.2.3. Wettability

We end with a brief discussion on surface wettability which has been introduced in section 2.1.1. Wettability has also been noted to affect the dependence of nucleate boiling heat flux on the wall superheat. Surfaces with higher wetting capabilities reduce nucleation which shifts the boiling curve to the right.

In the present study, the wetted surfaces are engineered with porous features and therefore affect the contact angle of wetting liquids with respect to their smooth ideal counterparts. Two common regimes exist: Wenzel and Cassie. The former regime is generally associated with the wetting of rough, hydrophilic surfaces. In such cases, roughness makes the surface *more* hydrophilic compared to a smooth surface of the same material. In the latter regime (Cassie), the liquid droplet will simply sit above the surface features. This regime is associated with chemically heterogeneous surfaces. Both regimes are illustrated in Figure 2-7.

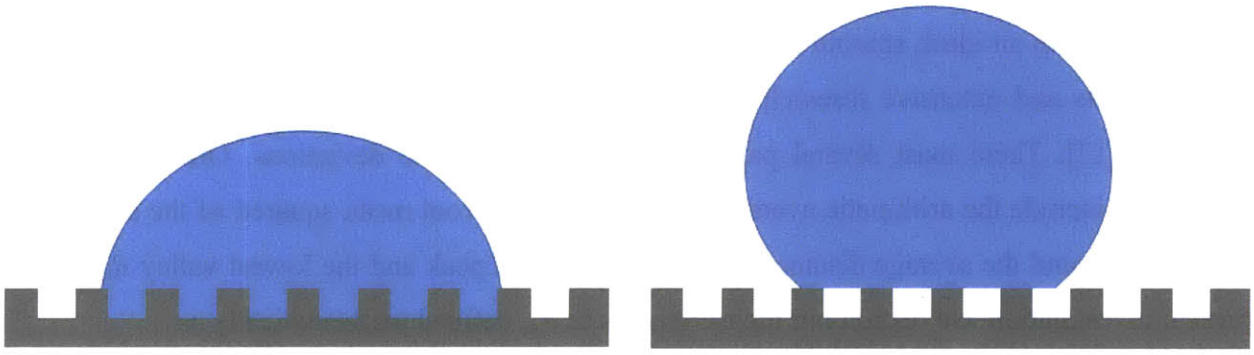

Figure 2-7 Wenzel regime (left) and Cassie regime (right).

2.3. Surface Engineering

2.3.1. Surface Engineering Methods for Nucleate Boiling

A number of methods to modify surfaces for nucleate boiling have been investigated. Researchers discovered in the first half of the twentieth century that surface roughness could improve nucleate boiling performance which instigated a plethora of research on the subject of surface engineering. Webb [3] outlines many of the important techniques developed in the past century. In 1931, Jakob and Fritz [18] first investigated the effects of sandblasted surfaces and surfaces with machined grooves, but reported only small improvements which decayed over time. In the following years, researchers such as Berenson [17] studied surfaces roughened with emery paper and reported heat flux enhancements up to 600%. In the years between 1955 and 1965, extensive studies provided significant insight in the fundamental understanding of nucleation sites and the characteristics required to form stable vapor traps.

In later years, surface engineering for nucleate boiling studies were extended to investigate the effects of surface wettability and porosity characteristics. Surface treatments to create roughness include abrasive treatments, grooves, knurling, and chemical etching. Arrays of small Teflon spots and porous sintered metallic coatings have been used to create hydrophobic (non-wetting) areas on surfaces. Methods to create porous coatings include electroplating and metal spray coatings. An alternate method to enhance a surface's performance is to attach a nucleation promoter such as a cover sheet, wires, or screens [1, 17].

In more recent years, attention has shifted towards nanoengineered surfaces. In particular, nanoporous surfaces have been achieved via a technique referred to as nanofluid boiling. Nanofluids are engineered colloidal suspensions of nanoparticles. Kim et al. [19] carried out pool boiling experiments with water-based nanofluids containing Al_2O_3, ZrO_2, and SiO_2 at concentrations ranging between 0.001% and 0.1%. They reported a porous layer buildup upon boiling and a CHF increase of up to 50%. They also did a survey of similar experiments and noted that CHF enhancements of up to 200% were reported in the literature. In these studies, the contact angle of the boiling surface was significantly reduced following the porous layer formation. The CHF enhancement was attributed to the high surface wettability.

The major drawback of this method of creating nanoporous surfaces via nanofluid boiling is the randomness of the porous layer buildup and the difficulty in controlling the features of the porous layer such as thickness and void fraction.

Hwang and Kaviany [20] investigated pool boiling on thin uniform porous coatings using brazed copper particles. The particle diameters range between 40-80 μm and the film thicknesses are between 3 and 5 times the particle size. They observed an average CHF increase of approximately 80% with respect to uncoated surfaces. They postulate that the underlying mechanism explaining this enhancement is due to a change in the wavelength of Helmholtz instabilities in Zuber's model previously discussed. Kim et al. [21] also investigated the effects of microporous surfaces on nucleate boiling and CHF in saturated FC-72, a highly-wetting dielectric perfluorocarbon. They used a platinum wire as their test heater with a dielectric DOM microporous coating. The porous coatings are 17.5 μm thick and the particles in the coating are 8-12 μm in size. They also reported significant CHF enhancement and attributed this to an increase in hydrodynamic stability, as described in Zuber's model.

Surfaces engineered with carbon nanotubes have also been investigated. Ahn et al. [22] coated silicon wafer substrates with vertically aligned multiwalled carbon nanotubes (MWCNT) "forests" by chemical vapor deposition (CVD). The forests were 9 and 25 μm in height and both the pitch and diameter of the MWCNTs varied from 8-16 nm. The pool boiling experiments were carried out using the refrigerant PF-5060 as the working fluid. They reported a CHF enhancement around 25% for the 25 μm height forests, and almost no enhancement for the 9 μm height forests.

Ujereh et al. [23] studied the effect of CNT arrays on nucleate boiling and heat transfer as well, using FC-72 as the working fluid. The CNTs were produced using an iron catalyst and the growth was achieved on a titanium underlayer. The arrays contained CNTs 50 nm in diameter, 20-30 μm, and were arranged in either grid patterns or island patterns, or were uniformly distributed on the substrate. The grid pattern was based on the instability wavelength derived for Zuber's model. The array pitch selected was around 5 mm, half the instability wavelength, and was chosen in order to study the possibility of manipulating the wavelength. The island arrays consist of sparsely distributed CNTs with small clusters. 45% CHF enhancement was achieved using the uniform coating, 26% enhancement was achieved with the grid pattern, and 15% for the island pattern.

Nanowires have also been engineered onto surfaces to improve boiling performances and enhance CHF. These rough surfaces have the potential to be surperhydrophilic, have significantly more pores and cavities than other surfaces, and effectively increase the total heat transfer area and provide a fin effect for improved heat transfer. Most importantly, they provide wicking structures which enhance surface rewetting. Chen et al. [24] fabricated Si nanowire coated surfaces using a wafer scale aqueous electroless etching technique. The Si nanowires have 20-300 nm diameters, are 40-50 μm long and are vertically aligned. They also prepared surfaces with Cu nanowires with an electroplating technique. The Cu nanowires have 200 nm diameters, and are 40-50 μm long. They reported CHF values of ~200 w/cm^2, a 143% enhancement with respect to their bare heaters. It is postulated that the large enhancement may be attributed to high nucleate site density, superhydrophilicity, and enhanced capillary pumping.

Most recently, O'Hanley et al. [12] investigated the separate effects of wettability, roughness, and porosity on CHF by systematically testing 9 different combinations of these three parameters. The features were engineered on sapphire substrates. Rough surfaces were created by implanting micro-posts via photolithography. The posts are 15 μm in height, 20 μm in diameter, and are aligned at a 500 μm hexagonal pitch. The porosity was controlled by depositing nanoparticles using a layer-by-layer assembly method. The particles deposited are hydrophilic, 50 nm diameter SiO_2 nanoparticles, and the coatings are ~1 μm thick. Finally, the wettability was controlled by depositing smooth uniform layers of hydrophilic silica or hydrophobic fluorosilane by Electron Beam Physical Vapor Deposition (silica) or Chemical Vapor Deposition (fluorosilane). They reported that roughness and intrinsic wettability do not affect CHF. Hydrophobic porosity greatly *decreases* CHF. And finally, that hydrophilic porosity greatly *increases* CHF (~60% enhancement). They note that their results and previous studies still agree with the hypothesis that CHF enhancement is caused by capillary wicking. However, they postulate that in previous studies, surface features described as rough are also coupled to porosity, which has led to inaccurate conclusions. It is believed that traditional measures of roughness are not suitable correlating parameters and should be replaced by parameters pertaining to porosity, namely void fraction, pore diameter, and effective pore length.

2.3.2. Layer-by-Layer Assembly

Layer-by-Layer (LbL) assembly provides a method to engineer nanoporous coatings and control the surface characteristics [25]. LbL deposition is achieved by alternately depositing layers of oppositely charged materials. The intermolecular interactions allow the layers of material to adsorb to the substrate. As can be seen in Figure 2-8, a substrate is alternately dipped in polyelectrolytes of opposite charge. At each step, the charge is reversed, allowing the following polyelectrolyte to adsorb via electrostatic forces.

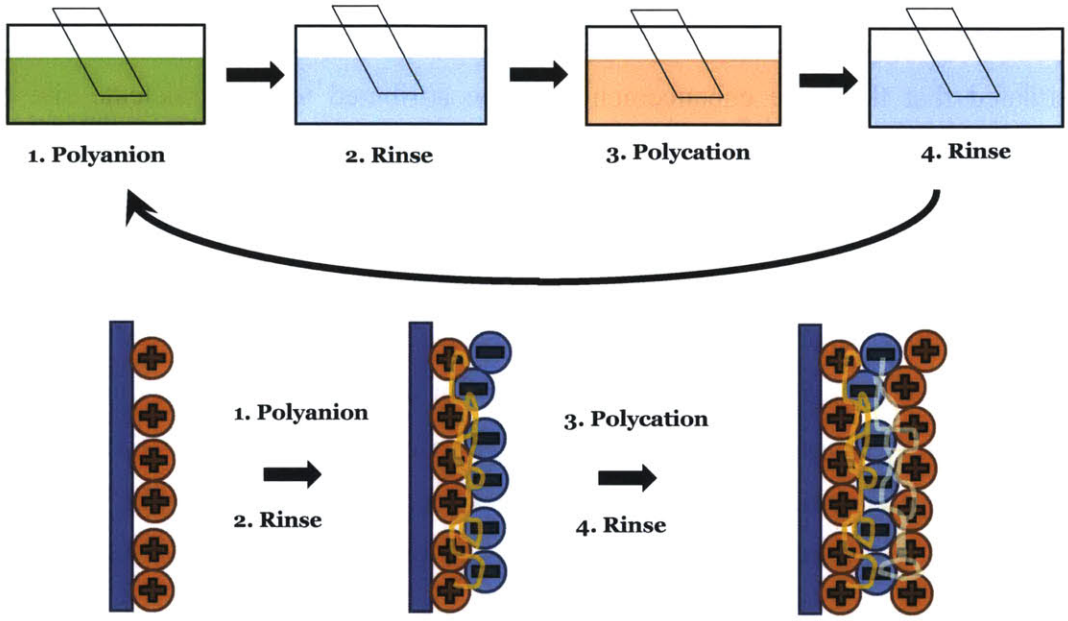

Figure 2-8 Layer-by-layer assembly process

The process described involves sequentially dipping substrates into polyelectrolyte solutions, however alternate methods of obtaining LbL assemblies include spin coating and spraying [26-27]. Furthermore, polyelectrolyte solutions include both polymer solutions and nanoparticle solutions.

LbL is a relatively simple processing method which allows to control the structure of the porous layer by varying the assembly conditions such as the pH of the polyelectrolyte solutions [28-29]. Coatings are smooth and homogeneous, unlike the nanofluid deposited porous layers which are random and irregular. The wettability can be controlled by selecting appropriate polyelectrolytes in the assembly [29]. The surface morphology can be modified by adding materials such as nanoparticles to the multilayer thin films.

Polyelectrolytes can be classified into two categories: strong polyelectrolytes and weak polyelectrolytes. The classification is made based on the pH-dependence of their degree of ionization. Strong polyelectrolytes are fully ionized at any pH. On the other hand, the degree of ionization of weak polyelectrolytes highly depends on the pH of the solution. Consequently, the charge density of the polymers may readily be manipulated. In addition, their interaction with oppositely charged species may also be altered. It is therefore possible to control the assembly structure and obtain specific features by adjusting the pH to vary the charge in weak polyelectrolytes. Shiratori and Rubner carried out a detailed study of the effects of pH on the assembly of weak polyelectrolytes PAH and PAA [28]. They were able to develop a map of the average thickness per bilayer for different pH conditions (Figure 2-9) which varied between a few angstroms to 160 Å.

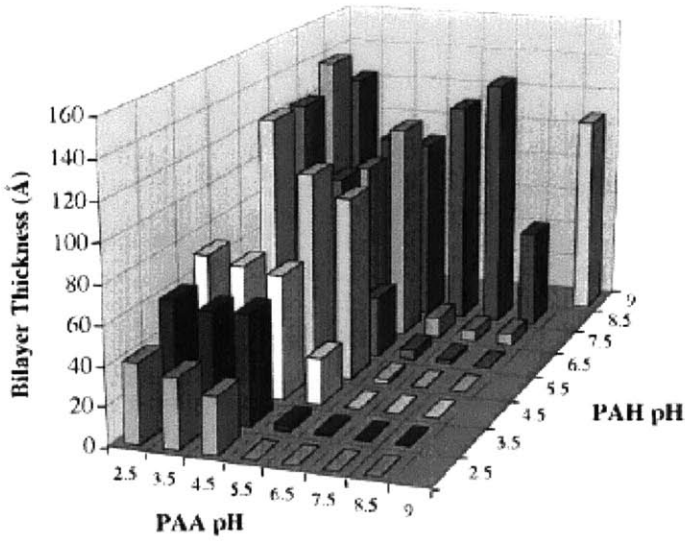

Figure 2-9 Complete pH matrix showing the average incremental thickness contributed by a PAH/PAA bilayer as a function of dipping solution pH. Adapted from Shiratori and Rubner [28]

The roughness varied less dramatically than the thickness, between a few angstroms and approximately 50 Å. DeRocher et al. later carried out experiments to investigate layer-by-layer coatings in nanofluidic devices [30]. They were able to assemble uniform polyelectrolyte multilayers of PAH and SPS in confined nanochannels and reported a linear trend between number of bilayers and thin-film thickness. Polyelectrolyte thin-films in nanofluidic devices can be used to functionalize the surfaces for various applications.

It is also possible to control the wettability of the assembly by adjusting the pH of the polymer solutions for specific polyelectrolyte combinations. Yoo et al. [29] studied the pH-dependence of the wettability and per bilayer thickness for sequentially adsorbed layers of PAH and PAA weak polyelectrolytes. They reported advancing contact angle measurements ranging between 0°-50°. For a single bilayer of PAH/PAA at pH 2.5 and with the polyanion as the outermost layer, they obtained contact angles <5° and bilayer thicknesses on the order of a few angstroms. It is therefore possible to engineer surperhydrophilic surfaces without adding considerable thickness. This is of particular interests since it is possible to modify the wettability of surfaces with nano-features without significantly altering the original surface morphology. Figure 2-10 shows how the contact angle varies with the number of layers of PAH/PAA.

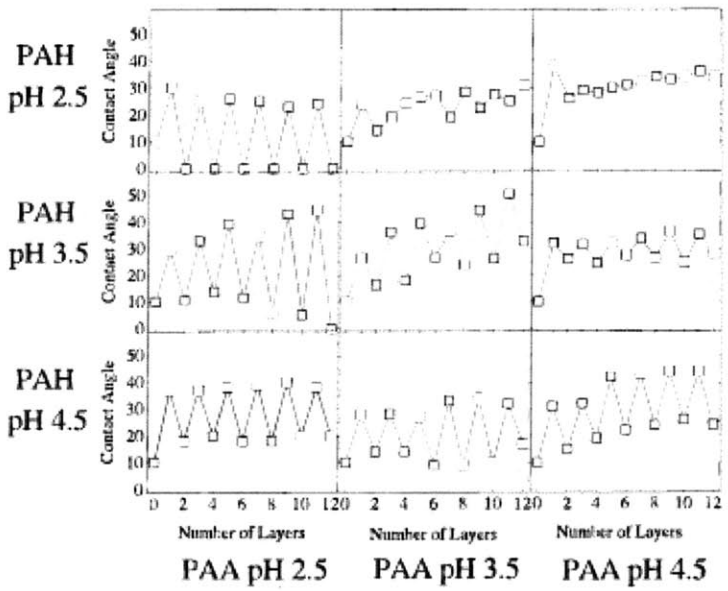

Figure 2-10 Contact angles measured from films containing a different number of adsorbed layers of PAH/PAA as a function of variations in the pH of the polyion dipping solutions. Even numbers represent films with PAA as the outermost layer whereas odd number films have PAH as the outermost layer. Adapted from Yoo et al.[29]

Another effective and useful feature in layer-by-layer assemblies is the ability to incorporate nanoparticles in multilayer thin-films to create nanoporous coatings. This is a convenient way to modify surface morphology that has been extensively studied [31-32]. Unlike porous coatings generated by nanofluid boiling, LbL coatings are homogeneous. The structure and properties of the porous coating can be modified by varying the pH and the size of the nanoparticles. Applications of nanoporous multilayers include antifogging coatings [33], and photovoltaic devices [34].

Most layer-by-layer applications focus on polymer multilayers. However, it is also possible to assemble multilayers of oppositely charged nanoparticles without polymers. The method was in fact developed in 1966 by Ralph K. Iler at DuPont [35]. Iler successfully assembled negatively charged silica particles with positively charged boehmite fibrils onto glass substrate. He also reported a correlation between the pH of the solutions and the structure and properties of the nanoparticle assemblies.

In summary, by combining the different LbL techniques discussed in the section, it is therefore possible to engineer a coating to desired thickness, void fraction, pore size, wettability, and roughness values.

3. Test Matrix

Porosity has been found to significantly enhance the boiling performance of heater surfaces. The three main surface parameters that characterize porous layers are the pore size, the thickness of the porous layer, and the void fraction (volume of voids over the total volume ratio). To investigate the effects of each of these surface parameters, a reference coating is selected as a starting point. From this starting point, each parameter is varied individually while all other parameters are kept constant. As noted in Chapter 2, O'Hanley et al.[12] found that hydrophilic porosity greatly increases CHF. The porous coating used in their study is approximately 1 μm-thick, has a 50% - 60% void fraction, is composed of 50 nm silica particles, and is fabricated using LbL deposition. In addition, the surfaces are smooth and superhydrophilic. The reference point in this study is identical, with the exception of 20 nm silica particles instead of 50 nm particles because the thickness can be controlled more readily with the smaller particles.

The pore size is known to be on the same order of magnitude as the particle size. The pore sizes investigated were therefore selected based on the available nanoparticles and the overall structure of the porous layer. For example, for a 1 μm-thick coating, the maximum particle size is not greater than 1 μm. The thicknesses chosen were limited by the fabrication method. The thickness was therefore increased up to a few microns. The thickness study was also repeated with a different particle size (50 nm) over a smaller thickness range to verify the trend. Finally the porosity of the reference coating is ~60%. The porosity was then decreased to 40% and 20%. The complete test matrix is presented in Table 3-1.

*Table 3-1 Test Matrix for Separate Effects Investigation. *Case 2 appears three times in the test matrix. ** Case 7 appears twice in the test matrix.*

	Case #	Pore Size (~Particle Size) (nm)	Layer Thickness (um)	Void Fraction (%)	R_a (μm)	Static contact angle
Effect of layer thickness	1	20	~0.5	~50-60	≈0	<5°
	2*	20	~1	~50-60	≈0	<5°
	3	20	~2	~50-60	≈0	<5°
	4	20	~2.5	~50-60	≈0	<5°
	5	20	~3.5	~50-60	≈0	<5°
	6	50	~0.5	~50-60	≈0	<5°
	7**	50	~1	~50-60	≈0	<5°
	8	50	~2	~50-60	≈0	<5°
Effect of pore size	9	6	~1	~50-60	≈0	<5°
	10	10	~1	~50-60	≈0	<5°
	2*	20	~1	~50-60	≈0	<5°
	7**	50	~1	~50-60	≈0	<5°
	11	100	~1	~50-60	≈0	<5°
Effect of void fraction	2*	20	~1	~50-60	≈0	<5°
	12	20	~1	~40	≈0	<5°
	13	20	~1	~20	≈0	<5°

4. Experimental Methods

The experimental methods involve coating manufacturing, verification, and testing. The process begins with bare heaters. The surface of these heaters are then nanoengineered with the porous coatings outlined in the test matrix. The porous layers are verified using a variety of surface analysis techniques to ensure that their features (thickness, roughness, porosity, pore size, and overall structure) match the objectives of the test matrix. Finally, the nanoengineered heaters are tested. Here, each step in this process is described in detail.

4.1. Heater Design

The ITO-sapphire heaters used in this study are supplied by Diamond Coatings and have been used in previous studies on the effects of nanoengineered surfaces on CHF. The sapphire is optical quality and has a scratch-dig specification of 40-20. Its hardness facilitates surface feature verification discussed in subsequent sections. The sapphire substrate of the heater is a 50.8mm square wafer, 0.25mm in thickness, with a nano-smooth polish. A 2cm wide and 700nm thick layer of ITO with a resistivity of <10Ω/sq. is positioned at the center of the substrate. The ITO conductive film serves as a resistive heating element and also provides an IR signal, as it is IR opaque, that is used to spatially determine the temperature of the boiling surface. Two 2.04cm by 2cm silver pads are positioned at each edge of the ITO band. They serve as contact points to attach electrodes to the heater and thus provide power for direct current (DC) resistive heating. The heater design is presented in Figure 4-1.

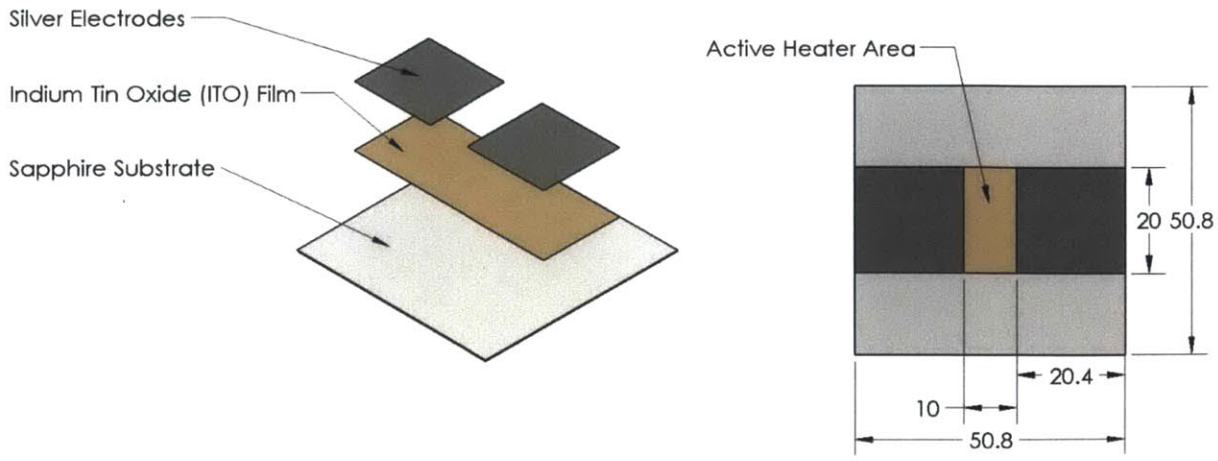

Figure 4-1 ITO sapphire heater - dimensions in mm. Adapted from O'Hanley. [6]

The nanoporous layers are engineered on the side opposite the ITO film by controlled deposition of nanoparticles. The engineered surface is therefore on the inside of the pool, in contact with the boiling fluid, while the ITO side of the heater is outside the pool. This inverted heater configuration eliminates corrosion from the electrodes that would otherwise occur from exposure with water in the pool. The surface temperature measurement is obtained using an infrared (IR) camera aimed at the ITO side of the heater substrate, and the temperature at the surface of the engineered side is calculated from the heat conduction equation.

4.2. Surface Fabrication

4.2.1. Layer-by-Layer Assembly

The desired surface characteristics are created using a technique called Layer-by-Layer (LbL) deposition developed by Prof. Cohen in the Chemical Engineering department and Prof. Rubner in the Materials Science and Engineering Department of MIT [31,32,33]. A more in-depth description and summary of the underlying theory involved in the method are outlined in Chapter 2. Briefly, it consists in alternately dipping a substrate in positively and negatively charged solutions of nanoparticles and polymers. The charge difference allows the particles to diffuse onto the surface of the substrate and create a bilayer. The nanoparticles used in this study are made of hydrophilic SiO_2 nanoparticles, rendering the porous coatings superhydrophilic.

Monodispersed nanoparticles assemble in a loose packed fashion to approximately 50% of the total volume. Therefore, the pore size is of the order of the particle diameter. LbL enables creation of a very smooth porous layer such that the average roughness R_a is on the order of nanometers and is therefore negligible.

4.2.1.1. Surface Preparation and Plasma Treatment

The substrate must first be adequately prepared for the assembly to ensure a better adhesion and maximize durability since sapphire is not an ideal surface for LbL assembling. In addition, when the surface is prepared using an appropriate procedure for the surface type, the initial conditions of the surface are always the same and the coating is more readily predictable and repeatable. The substrate to be coated is thus first thoroughly rinsed with deionized (DI) water and dried with compressed air. It is subsequently cleaned in an oxygen-plasma cleaner for two minutes at the highest power setting under 150mTorr vacuum to remove surface contaminants and to restore its intrinsic wettability.

Photons released from the excited molecules of an ionized low pressure oxygen gas have enough energy to break most organic bonds of surface contaminants. For this application, plasmas are weakly ionized and the ions are thus near the ambient temperature.

Dirt and oil make a surface more hydrophobic. Hence, the dirt on the irradiated surface combines with plasma particles and is removed from the surface (Figure 4-2). The gas adsorption layer is removed and the layer appears at the surface, making it more hydrophilic. This initial surface condition is preferred for LbL deposition.

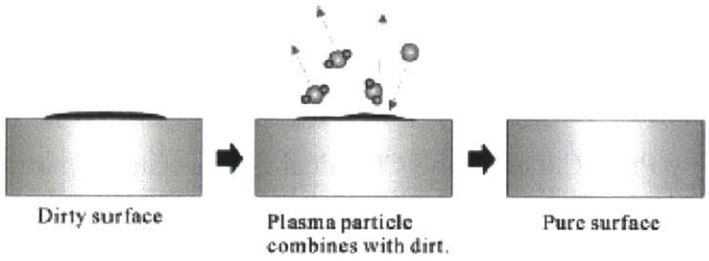

Figure 4-2 Reaction of a surface by plasma irradiation. Adapted from Takata, Y., et al. [36]

A Harrick Plasma Plasmaflo was used for this application, shown in Figure 4-3.

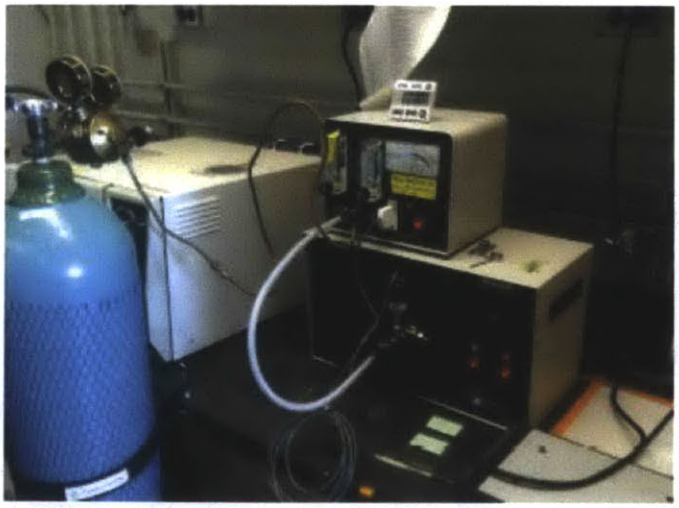

Figure 4-3 Harrick Plasma Plasmaflo Adapted from O'Hanley [6].

4.2.1.2. Layer-by-Layer dipping procedure

The general assembly process for one bilayer is depicted in Figure 4-4. These steps are carried out by a Zeiss HMS Programmable Slide Stainer (Figure 4-5).

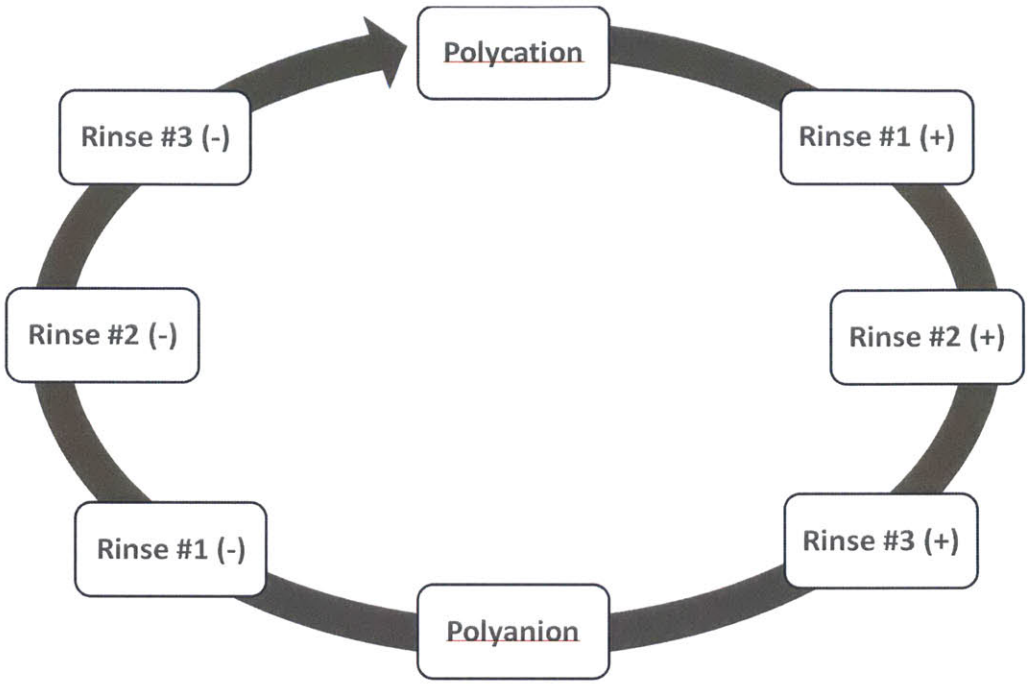

Figure 4-4 Flow chart depicting assembly process for a single bilayer.

Figure 4-5 Zeiss HMS Programmable Slide Stainer

The heaters used in this application are fairly large compared to typical substrates used in LbL applications. When dipped in typical 0.5 L baths, the coatings were not uniform and not readily repeatable. For this reason, the setup was modified to accommodate larger 1L baths which provide better circulation around the bigger substrates and more uniform coatings. In addition, each bath is positioned on individual stir plates with a stir bar inside which lightly stirs the solution without creating vortices at the surface. The stirrers are particularly important when using larger nanoparticles (~100 nm) since they are heavier and tend to settle more rapidly.

4.2.1.3. Pore Size

Layer-by-layer deposition of spherical nanoparticles yields a loosely packed assembly of nanoparticles. The void fraction (porosity) generally ranges between 50% and 60% for all the particle sizes studied. The size of the voids (pores) however does vary with the particle sizes and is in fact on the same order as the particle size (shown in the SEM/FIB images in the results in the following chapter). In addition, the roughness is also on the order of the particle size. Thus, a coating comprised of 50 nm particles will have both voids and roughness (R_a) on the order of 50 nm.

The study of the effects of pore size was carried-out by selecting a nanoparticle size on the order of the desired pore size for each case in the test matrix. The specific sizes were therefore limited by commercial availability of nanoparticles. The nanoparticles used in this study are summarized in Table 4-1.

Table 4-1 List of nanoparticle products used and suppliers.

Particle Size	**Commercial Product Used**
6 nm	NYACOL NexSil 6 Aqueous Colloidal Silica
10 nm	Polysciences Silica Microspheres
20 nm	Sigma-Aldrich Ludox TM-40 Colloidal Silica
50 nm	Polysciences Silica Microspheres
100 nm	Polysciences Silica Microspheres

The nanoparticles are available in aqueous solution at pH ~9.0. These nanoparticles are negatively charged and therefore play the role of the anion in the assembly. They arrive at different stock concentrations depending on the supplier (usually within the range of 5-40wt%) and are diluted to a concentration of 0.03wt% in a pH 9.0 buffer. 0.1M NaCl is also added to the nanoparticle solution in order to increase the ionic strength and promote adsorption. The buffer solutions are very stable and can be prepared and stored for several weeks. The nanoparticles however tend to agglomerate and settle fairly rapidly and should not be added to the solution more than one day prior to dipping. Buffers were therefore stored up to one month and nanoparticles were added a few hours before the assembly process.

Poly(allylamine hydrochloride) (PAH) is used as the cation in the assembly. PAH (M_w = 120,000 – 200,000, 40% aqueous solution) was purchased from Polysciences. It is diluted to 0.01 M concentration and adjusted to pH 7.50. Polymer solutions such as PAH are relatively stable and were prepared up to one week in advance. The pH of the solution was always verified up to one hour before beginning the assembly.

Both cation and anion solutions are typically prepared in 1L batches. They are each allowed to stir for at least 1 hour before adjusting the pH. The rinsing solutions are all deionized water at neutral pH. The dip time for the anion (PAH)/cation (nanoparticles) and three rinse baths are 10, 2, 1, and 1 minutes respectively. The exact recipes used in this study are found in Tables 4-2 and 4-3 and the dipping sequence with dip times in each bath is shown in Figure 4-6.

Table 4-2 Negative LbL solution for nanoparticle assembly: 0.03wt% Si02 nanoparticles at pH 9.0

Component	**Quantity**	**Purpose**
Deionized Water	1L	Dilution
SiO_2 nanoparticles	Quantity required to obtain 0.03wt% (depends on stock concentration)	Source of SiO_2 nanoparticles
Boric acid	3.1 g	pH 9.0 buffer
KCl	3.7 g	
NaOH	0.86 g	
NaCl	5.845 g	Aid adsorption

Table 4-3 Positive LbL solution for nanoparticle assembly: 0.01 M PAH at pH 7.5

Component	Quantity	Purpose
Deionized Water	1L	Dilution
PAH (40% aqueous solution)	2.3425 g	Supply of positive polymer (cation)
1M NaOH	Quantity required to obtain solution pH 7.5	pH adjustment

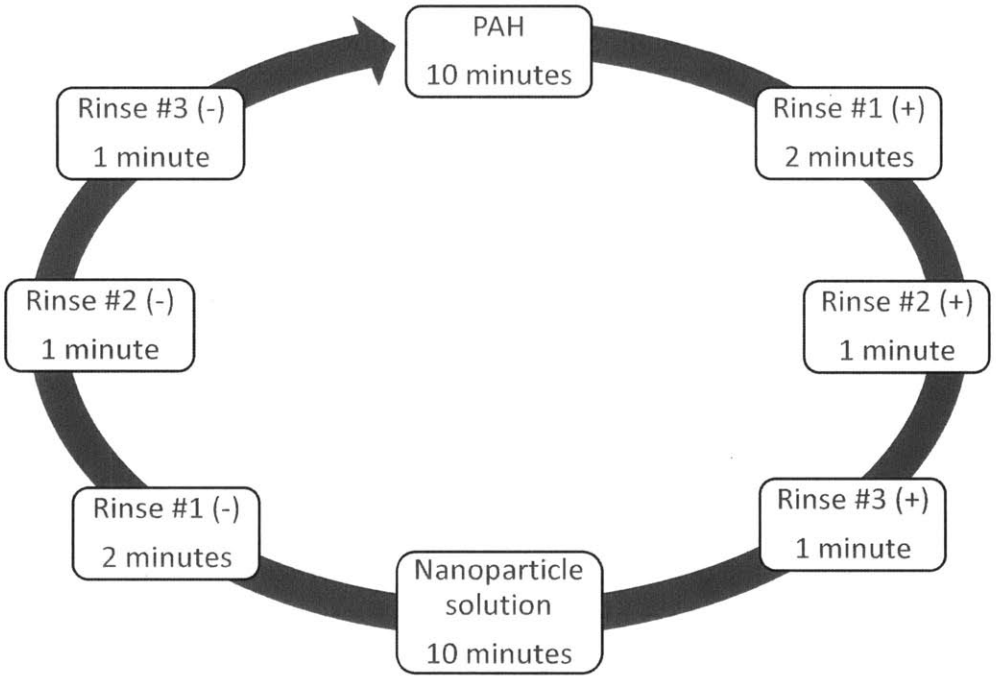

Figure 4-6 LbL detailed sequence for nanoparticle assembly.

Each coating in this part of the study is carefully engineered to a thickness of 1 μm. This thickness is obtained by depositing a specific number of bilayers (the number of times the sequence in Figure 4-6 is repeated) on a specific substrate. The growth rate per bilayer varies for each particle size and depending on the nature of the substrate. The number of bilayers required to obtain 1 μm-thick coatings for each particle size assembled on a heater substrate is therefore determined experimentally by trial and error. This process is discussed in more detail in Chapter 5.

4.2.1.4. Porous layer thickness

The porous layer thickness is controlled by varying the number of bilayers deposited on a substrate. The study was carried out using 50 nm particles and 20 nm particles and the same recipes as outlined in section 4.2.1.3. It was found that the 20 nm particles grow more rapidly and uniformly, and can be controlled more easily than 50 nm particle, despite being smaller. For this reason, the thickness was varied over a greater range using 20 nm particles.

4.2.1.5. Void fraction (porosity)

The void fraction was the most challenging parameter to control and vary since no precedent was found in varying the porosity of porous coatings in LbL assemblies and a new manufacturing method had to be developed.

Several approaches were first considered. The first was to decrease the porosity by combining two particle sizes to obtain a bimodal particle distribution. Smaller particles would be expected to effectively fill the interstitial voids between the larger particles. However, experiments carried out by Phillips [40] have shown that the porosity of a bimodal system of 50 nm and 20 nm particles is 47%, which is a negligible decrease in porosity with respect to the reference porosity of 50-60%. Experiments with bimodal distributions of more extreme particle sizes (6 nm and 100 nm) also produced similar results. These results should in fact be expected since particles of different sizes grow at different rates onto a given substrate and do not deposit uniformly. This method was therefore discarded.

The second approach considered is for increasing the void fraction above the reference range of 50-60%. The idea proposed is to add polymer nanoparticles to the SiO_2 nanoparticle solutions. The polymer nanoparticles could then be dissolved with acids or burned out of the coating when exposed to high temperatures, creating additional voids in the porous layer. The concept is depicted in Figure 4-7. There are however several potential challenges to consider. Since there are two types of particles in the assembly, their growth rate may again be different and the polymer particles may not be distributed uniformly in the nanoparticle coating. In addition, once the polymer particles are dissolved or burned, it is hard to predict how and to what extent the remaining silica particles would settle. The final structure of the porous coating is not readily predictable. Although this approach for increasing the amount of voids in the coating could certainly be successful, extensive experimentation and characterization would be required to guarantee its success.

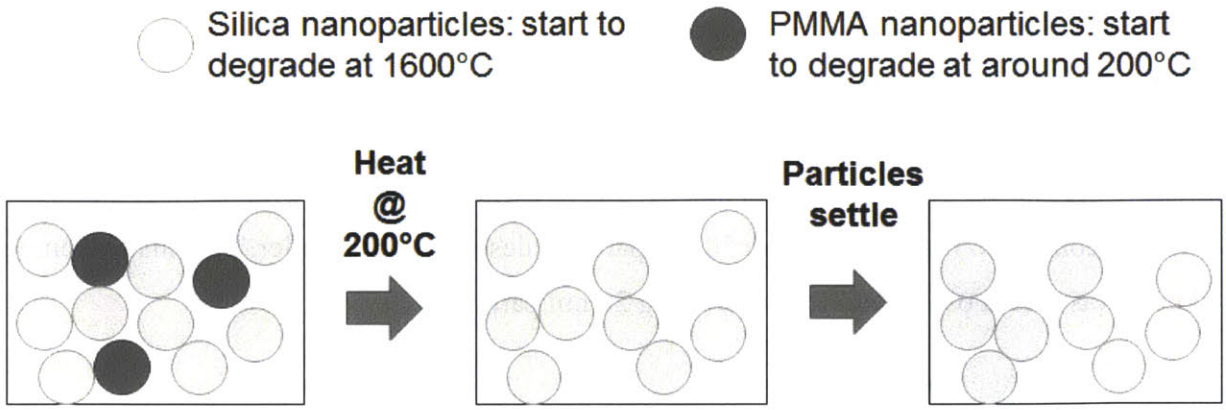

Figure 4-7 Diagram representing an alternate approach to varying porosity: A surface is coated with a mixture of silica and PMMA particles. The PMMA particles degrade at much lower temperatures than silica particles. They can therefore be burned off to create voids in the particle assembly.

The final approach selected was inspired by a study of polyelectrolyte multilayer deposition in confined geometries. In this study, DeRocher et al. [30] investigated layer-by-layer assembly of poly(allylamine hydrochloride) (PAH) and poly(styrene sulfonate) (SPS) used to conformally coat nanochannel walls to systematically change the nanochannel width to specific dimensions. This assembly method was applied to the nanoparticle coatings which are a type of confined geometry as well in which the PAH/SPS polymers are used to partially fill the voids in the porous coating as shown in Figure 4-8.

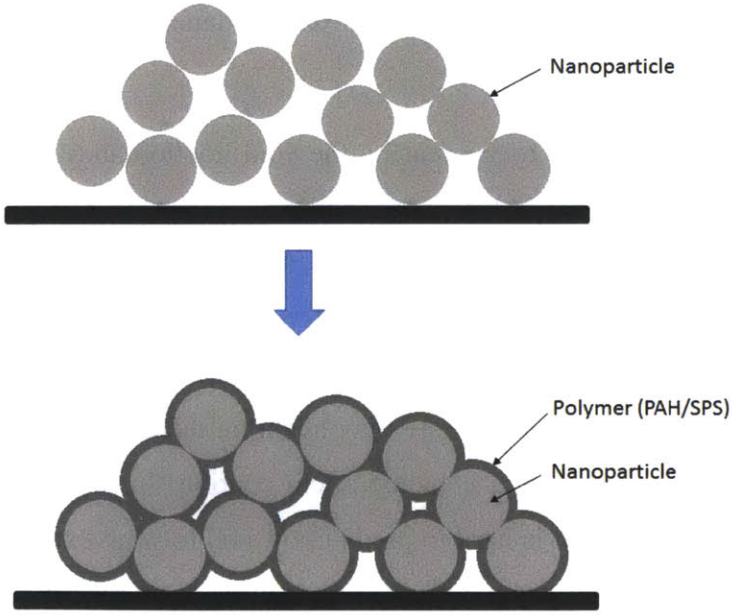

Figure 4-8 Basic concept of using polyelectrolyte multilayers to fill the voids in a porous coating to reduce the void fraction.

Poly(allylamine hydrochloride) (PAH) is used as the cation in the assembly. PAH (M_w = 120,000 – 200,000, 40% aqueous solution) was purchased from Polysciences. It is diluted to 0.01 M concentration and adjusted to pH 4.0. Poly(styrene sulfonate) (SPS) is used as the anion in the assembly. SPS (M_w = 70,000) was purchased from Sigma-Aldrich. It is diluted to 0.01 M concentration and adjusted to pH 4.0. In addition, the pH of the rinsing solutions were all adjusted to pH 4.0. The pH of each solution was always verified up to one hour before beginning the assembly. The dip time for the anion (PAH)/cation (SPS) and three rinse baths are 40, 10, 10, and 10 minutes respectively. These longer dip times are to ensure that the polymer solutions fully penetrate the porous layer. The exact recipes used in this study are found in Tables 4-4 and 4-5.

Table 4-4 Positive LbL solution for polyelectrolyte assembly: 0.01M PAH at pH 4.0

Component	Quantity	Purpose
Deionized Water	1L	Dilution
PAH (40% solution in water)	2.3425 g	Supply of positive polymer (cation)
1M NaOH or HCl solution	Quantity required to obtain solution pH 4.0	pH adjustment

Table 4-5 Negative LbL solution for polyelectrolyte assembly: 0.01M SPS at pH 4.0

Component	Quantity	Purpose
Deionized Water	1L	Dilution
SPS (dry powder)	2.07 g	Supply of negative polymer (anion)
1M NaOH or HCl solution	Quantity required to obtain solution pH 4.0	pH adjustment

The procedure to manufacture the lower void fraction coatings begins by preparing a standard reference coating, i.e. a LbL assembly with 20 nm SiO_2 nanoparticles and 1 μm-thick as described in Section 4.2.1.3. This typically requires 30 bilayers of PAH/20 nm-particles. The resulting porous coating has a void fraction of approximately 60%. The next step in the fabrication is to build an SPS/PAH assembly on top of the pre-existing porous coating. The polymers in this second assembly penetrate the pores and envelope the nanoparticles as illustrated in Figure 4-8, filling the voids and effectively reducing the porosity. Figure 4-9 presents SEM images of a porous coating before and after the addition of polymers to reduce the voids.

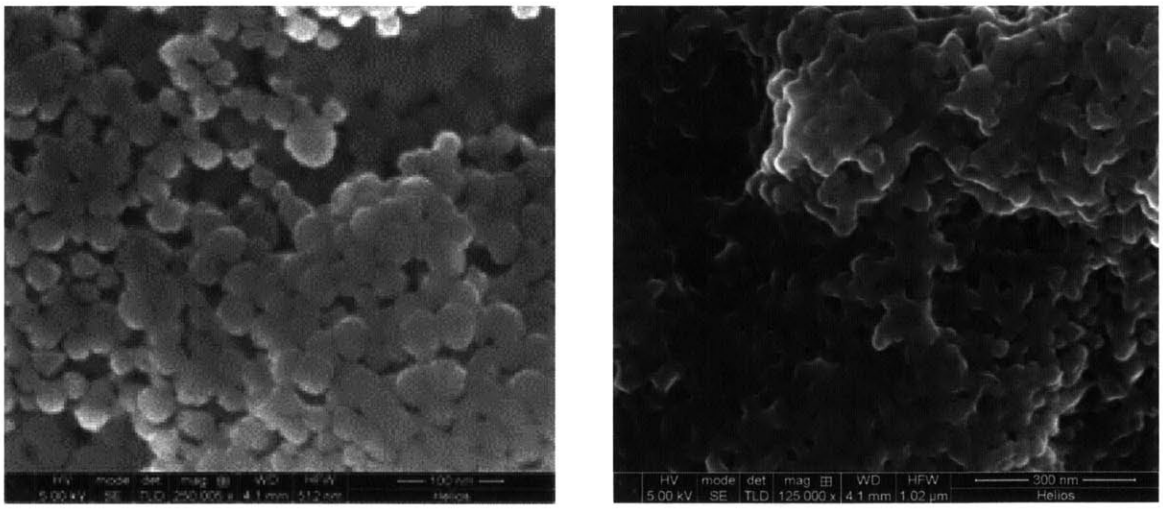

Figure 4-9 SEM images of a standard 60% void fraction porous coating (left) and a standard coating with polymers added to reduce the void fraction.

The number of bilayers required to obtain the desired void fractions were obtained by trial and error. The void fraction was measured with a spectroscopic ellipsometer for different numbers of SPS/PAH bilayers. The results are summarized in Table 4-6.

Table 4-6 Void fraction different numbers of SPS/PAH bilyers.

Number of SPS/PAH bilayers	Average void fraction (%)	Standard Deviation (%)
3	58	2
7	51	3
19	41	3
36	22	3

Based on these results, an assembly procedure was established and the corresponding dipping sequence with dip times in each bath is shown in Figure 4-10.

To determine the intrinsic wettability of the polymer assembly on a flat surface, an SPS/PAH assembly with 12 bilayers was prepared on bare silicon wafers. The measured average contact angle was 27°. Although SPS/PAH is hydrophilic, the contact angle remains higher than the desired contact angle for this study as we seek superhydrophilicity for all surfaces in the investigation. However, when the polymers are assembled on a porous structure, the Wenzel effect decreases the contact angle to an acceptable range <10 °. In addition, other more hydrophilic polymer assemblies

such as poly(acrylic acid) (PAA)/poly(styrene sulfonate) (SPS) were tested but were not compatible with the ITO-sapphire substrate used in the investigation.

The durability of PAH/SPS assemblies under boiling conditions has been evaluated by Forrest [37]. It was determined that these polymer assemblies do not have any noticeable degradation and can therefore be used under boiling conditions.

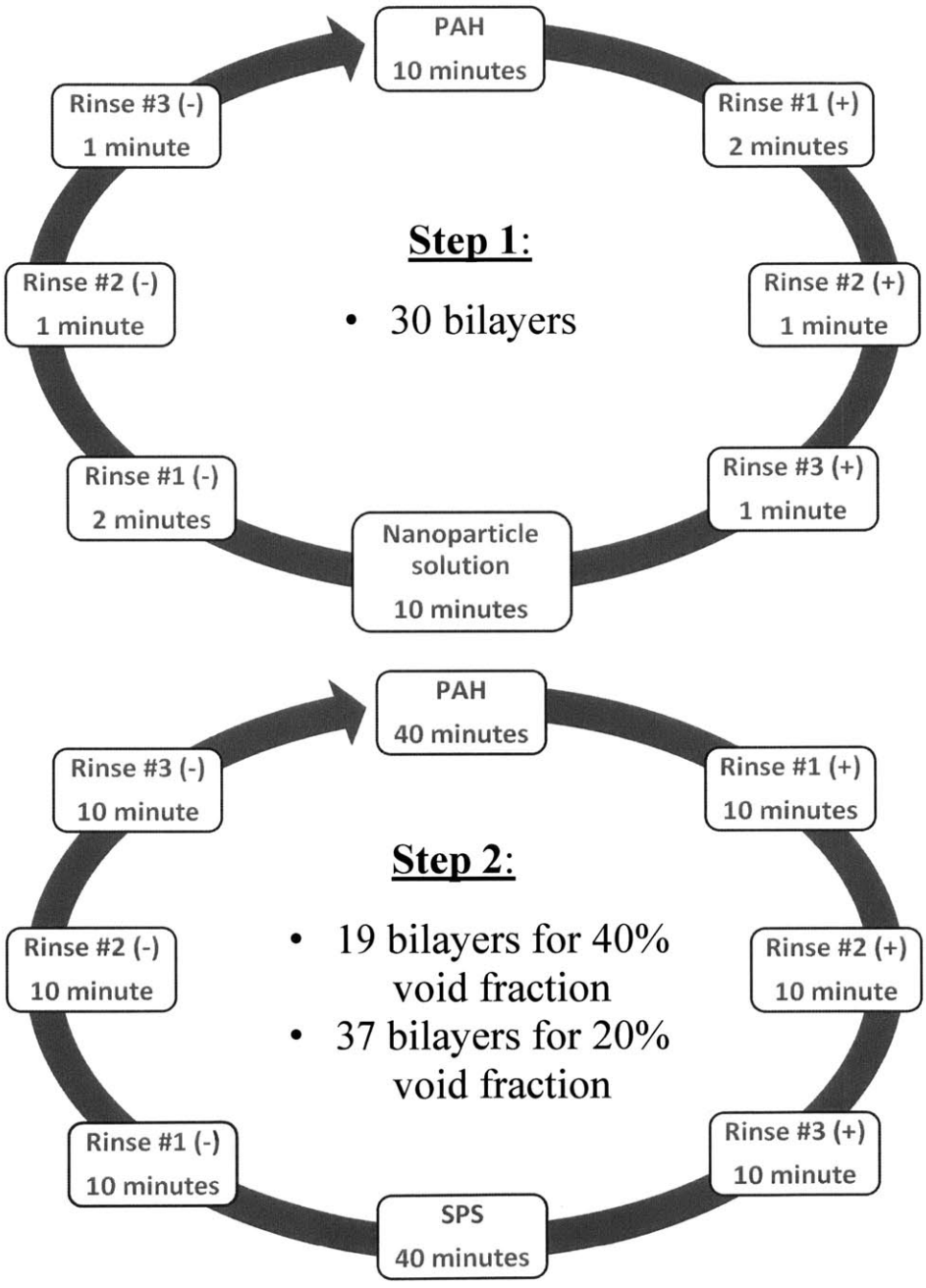

Figure 4-10 LbL detailed assembly process.

4.3. Surface feature verification

4.3.1. Dual Beam (SEM/FIB) for structure and pore size verification

High resolution instruments were required to characterize the nanoporous structures fabricated. These surface features were therefore inspected with the Helios Nanolab 600 Dual Beam Focused Ion Beam Milling System (FIB) (Figure 4-11) at the MIT Center for Materials Science and Engineering Shared Experimental Facility. The Dual Beam consists of a scanning electron microscope (SEM) and a focused ion beam (FIB) which allows one to perform nanoscale imaging and machining with a single instrument. The electron optics can reach a 0.9nm resolution at 15kV and the ion optics reach a resolution of 5nm at 30kV. Because the substrate and porous coatings analyzed are non-conductive, a thin layer of carbon (<10nm) was deposited via carbon evaporation. Thin layers of gold (10nm-20nm) deposited via sputtering were also used in certain cases. However, these coatings were found to be less suitable for this application due to visible non-uniformities at the nanoscale. The FIB function is used to mill small rectangular sections a few microns in length and width and 1-2μm in depth. The SEM function is used to characterize the nanoporous features (structure and pores) by obtaining top view images and cross-sectional images from the milled section of the porous coating.

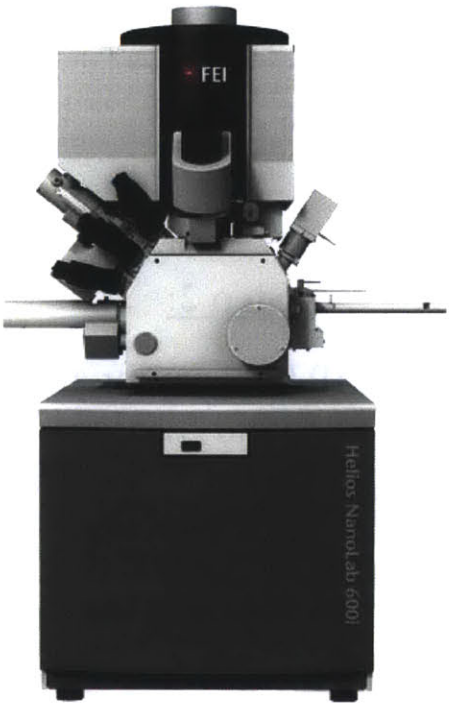

Figure 4-11 Helios Nanolab 600 Dual Beam Focused Ion Beam Milling System (FIB). Adapted from FEI [38]

4.3.2. Contact angle measurements for wettability verification

The wettability of the coatings is determined by measuring the static contact angle on each surface using a KSV Instruments CAM 101 (Figure 4-12). The measurements are carried out by depositing a water droplet onto the surface. A CCD camera connected to a computer captures images of the droplet, and the drop profile is then curve fitted with an image analysis software. An angle measurement is made on each side of the droplet which should be in good agreement. At least three measurements are made on each surface and the average of the measurements is reported. Since the surfaces studied are all expected to be superhydrophilic (contact angle less than 5°), more advanced contact angle measurements (e.g. advancing, receding, etc.) were not necessary and were beyond the scope of this research.

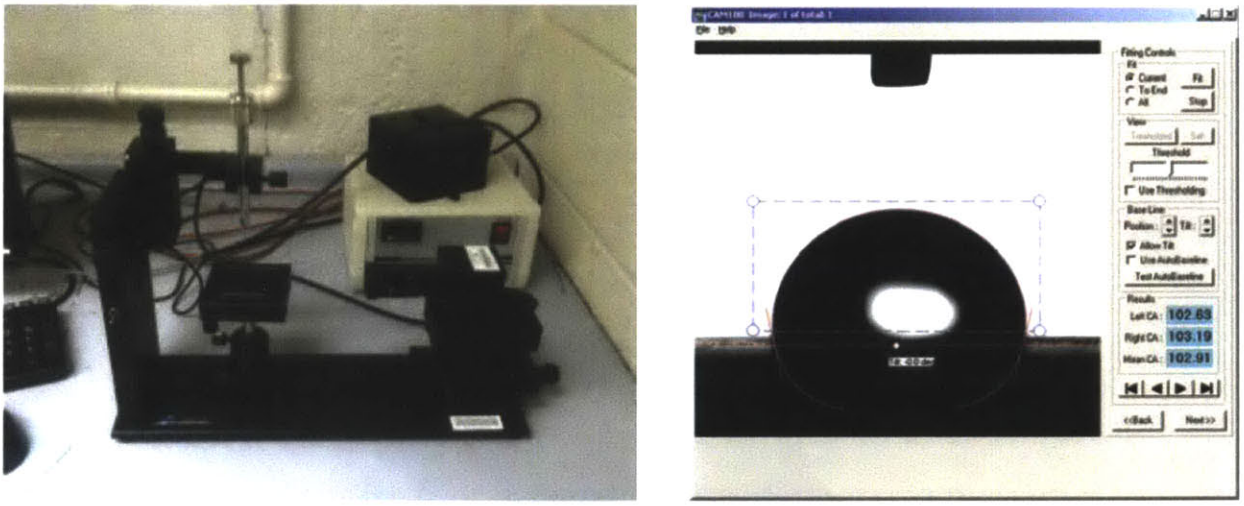

Figure 4-12 KSV Instruments CAM 101 (left) and image analysis software (right).

4.3.3. Surface Profilometer for thickness and roughness verification

The thickness and roughness of the porous coatings were verified using a Tencor P-16 Surface Profilometer (Figure 4-13) at the MIT Center for Materials Science and Engineering Shared Experimental Facility. The instrument uses a 2μm radius diamond tipped stylus to perform various surface metrology measurements such as step heights, roughness and curvature. The stylus force on the surface is 2mg and typical measurements range between 20 Angstroms to 1mm. Scan lengths taken range between 1μm and 2 μm. Ra measurements were obtained from a simple scan along the surface of the porous layer. The features cause vertical displacements of the stylus which are analyzed by a software. To calculate the thickness of the coatings, a razor blade was used to

create a thin scratch in the layer down to the surface of the substrate. Because coatings are typically assembled on silicon or sapphire substrates which are hard surfaces, the depth of the scratch through these surfaces due to the razor blade is considered negligible with respect to the thickness of the porous layer and does not contribute significantly to the overall thickness measurement. To obtain the final thickness measurement, the profilometer stylus measures the surface features along a line that travels through a section of the coating and through the scratch. The instrument software then calculates the step height between the surface of the coating and the surface of the substrate onto which the coating is assembled. A sample measurement is shown in Figure 4-14. For both roughness and thickness measurements, at least 4 measurements were obtained and averaged for each coating.

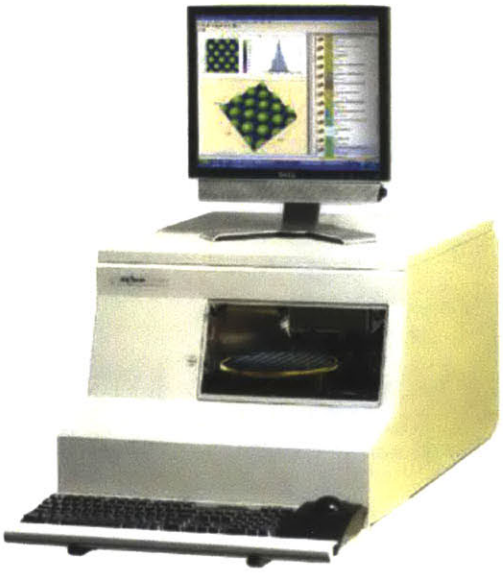

Figure 4-13 Tencor P-16 Surface Profilometer. Image adapted from ScienTec [39]

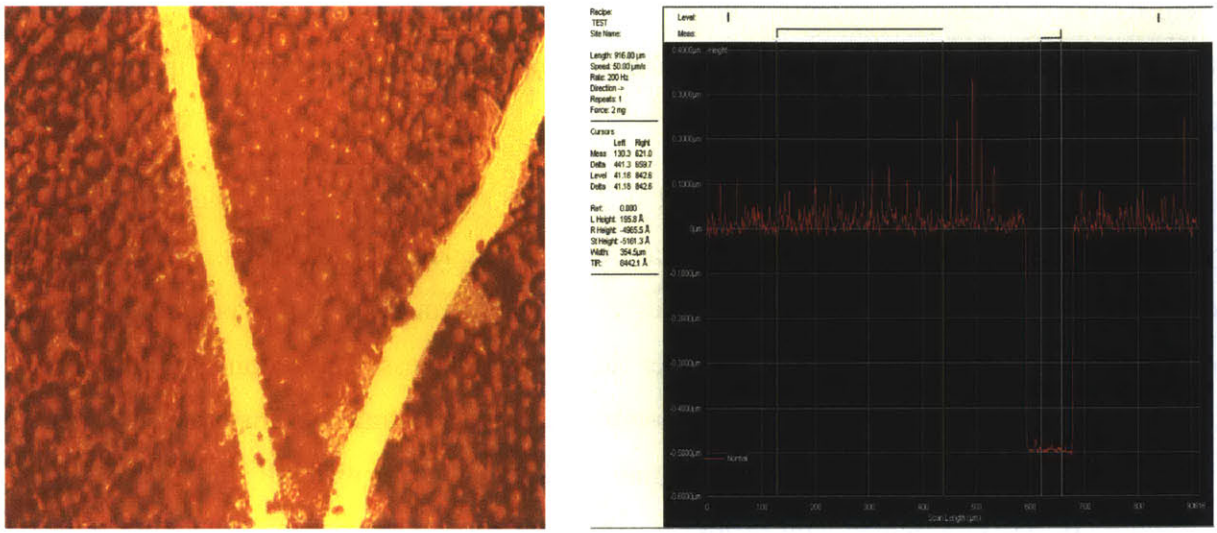

Figure 4-14 Sample thickness measurement obtained from profilometry. A typical scratch through the porous coating is shown on the left, and the data obtained from the profilometer on the right.

4.3.4. Spectroscopic ellipsometer for void fraction verification

Ellipsometry is an optical technique for characterizing thin film materials based on their index of refraction. Typically, incident light in a known state interacts with a material. The change in polarization due to the refractive index and the thickness is then measured and used to extract information to characterize the material. The method can be used to determine the composition, roughness, thickness, electrical conductivity, porosity, and other material properties using different modeling techniques.

In this study, ellipsometry was used to determine the porosity (void fraction) of the porous coatings using the J.A. Woollam Co., INC model XLS-100 (Figure 4-15) at the Institute for Soldier Nanotechnologies at MIT. The measurement is based on the difference in index of refraction of the porous coating immersed in air and in a liquid. An initial basic thickness measurement is made. The model obtained is verified by comparing the thickness measured on the ellipsometer with the thickness measured on the profilometer thickness. The porous layer is then immersed in a liquid which fills the pores (deionized water in this case). The volume fraction of the pores can then be obtained from the rule of mixtures [31] from the following equation

$$p = \frac{n_2 - n_1}{n_{water} - n_{air}} \tag{4.1}$$

Where n_2 is the measured refractive index of the film immersed in water, n_1 is the measured refractive index of the film immersed in air, and n_{water} and n_{air} are the refractive indices of water and air respectively.

Ellipsometry presents two major limitations. The first limitation is that the technique was developed for very thin films on the order of a few hundred nanometers. For this reason, measurements could only be made on porous coatings 500nm thick and it is assumed that the porosity remains approximately constant over the entire thickness. The second limitation comes from the substrate on which the coating is assembled. If the substrate is transparent, it will cause additional reflections and diffuse the signal, making it very difficult to obtain accurate measurements. This caused several problems when measuring the porosity on sapphire heaters. The measurements were taken for coatings assembled on silicon wafers which are not transparent and are assumed to have the same porosity as those assembled on sapphire. This is considered a reasonable assumption since only the initial growth rate and ~5 layers are expected to change for different substrates.

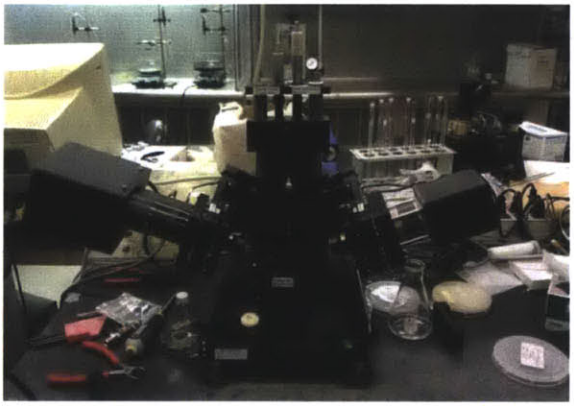

Figure 4-15 J.A. Woollam Co., INC model XLS-100 Spectroscopic Ellipsometer. Adapted from Phillips [40].

4.3.5. Additional feature verification techniques

Several of the above mentioned measurement techniques present certain limitations and modifications can either be made or alternative approaches can be used.

Because the substrates and porous layers used are non-conductive, conductive coatings need to be deposited on the surfaces of each sample in order to carry out SEM/FIB verifications. These

additional coatings are inconvenient since they mask some of the features and partially fill the voids. These undesirable effects become more significant when the surface features are on the order of (or less than) 10nm (the thickness of these conductive coatings). One way to resolve this problem would be to manufacture the LbL coatings on conductive surfaces which would eliminate the need for additional coatings such as gold or carbon. Further investigation would be required in this case in order to find a substrate that would closely match the growth rate and the final structure of the LbL assembly on the sapphire substrates.

Porosity measurements also present measurement limitations. Since ellipsometry is developed for thin films, the technique cannot be used for coatings greater than 1μm thick. Other instruments have been used to obtain porosity measurements for nanoscale porous layers such as the Quartz Crystal Microbalance (QCM). Measurements on this instrument are based on a vibrating quartz crystal sensor (acoustic resonator) which is used to detect changes in vibration frequency. These measurements provide insight about mass and structural changes. It is therefore possible to measure a substrate before and after it has been coated with an LbL assembly and to deduce the mass of the coating. The volume of the coating can be calculated from the surface area of the substrate and the thickness measurements obtained from profilometry. Finally, given the known mass of air, the mass of the material in the LbL coating (SiO_2 in this application), and the total volume of the coating, it is possible to calculate the porosity. This method can be used to measure the mass of coatings several microns thick. It is however much more time consuming than ellipsometry and is therefore not appropriate for applications which require a porosity characterization for a large amount of different coatings.

4.4. Heater Testing

The pool boiling facility is an aluminum bath with an isolated inner bath in the center which is open at the bottom to allow placement of the ITO-heater and for optical access. A 1500W heater positioned in an isothermal outer bath heats and maintains the water at atmospheric saturation conditions throughout the experiment. The test heater is attached to the bottom of a borosilicate tube which is lowered into the inner bath. The entire setup can be seen in Figure 4-16.

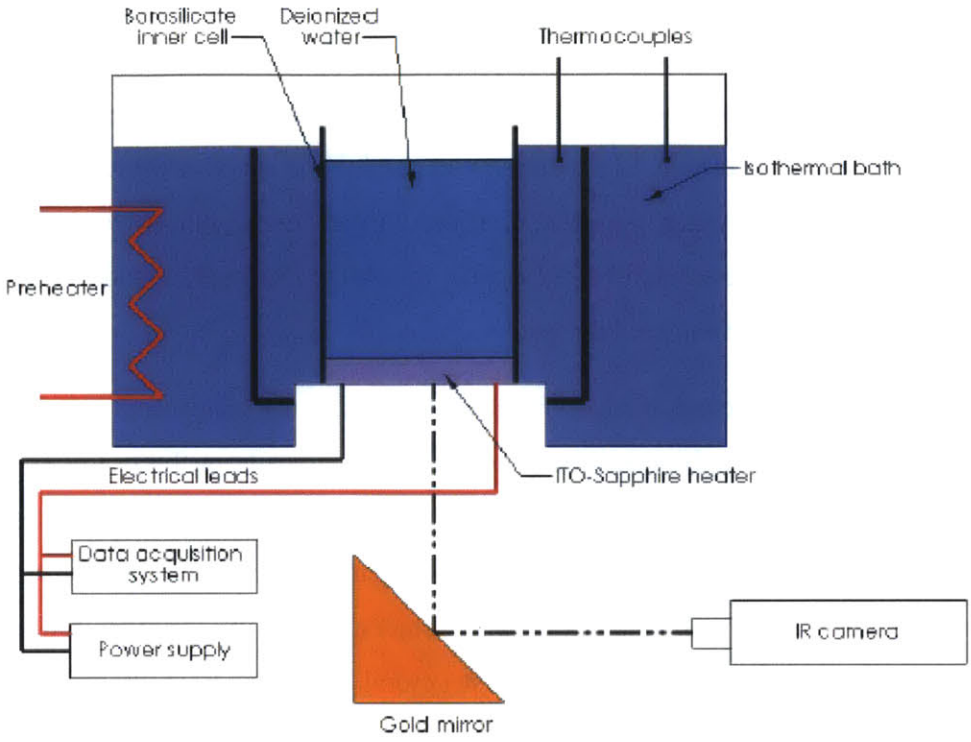

Figure 4-16 Schematic of the Pool Boiling Facility. Adapted from O'Hanley [6].

The heater is first prepared by cleaning the silver pads and the ITO with a cotton swab. The heater is then attached to the bottom of the borosilicate tube with silicone sealant such that the engineered boiling surface is on the inside of the tube facing up. Electrical leads are attached to the silver pads with silver epoxy. The epoxy is then allowed to cure for 24 hours. Once the epoxy has cured, the borosilicate tube and heater assembly are lowered into the inner bath with the electrical leads accessible through the bottom. The borosilicate tube is filled with DI water, and the inner and outer baths are filled with tap water. The electrical leads are connected to a DC power supply and a data acquisition system is also integrated in the circuit to monitor the power. A 45° angle gold mirror is positioned below the heater and an IRC800 LN2 infrared (IR) camera is directed towards the mirror. The 1500W heater in the outer bath first heats the water to saturation. The test is carried out once the water has reached saturation. The heat flux is gradually increased and IR images are captured at specific heat flux values. The heat flux can be calculated from the electrical power and the active heater area as $q" = P/A_{active\ heater}$, where $q"$ is the heat flux, P is the electrical power obtained from the data acquisition system, and $A_{active\ heater}$ is the active heater area. The images obtained from the camera are then analyzed using a Matlab script to obtain the area averaged

emission at a given heat flux value. Calibration methods are used to convert IR data into average temperatures. Finally, since the images captured are obtained for the opposite side of the boiling surface, a simple heat conduction calculation allows to obtain the temperature on the boiling surface. The following equation is used:

$$T_{upper} = T_{lower} - q"R_{sapphire},$$

where $q"$ is the heat flux, T_{lower} is the temperature captured by the IR camera, $R_{sapphire}$ is the thermal resistance through the sapphire, and T_{upper} is the temperature on the boiling surface. Finally, $R_{sapphire}$ is simply $t_{sapphire}/k_{sapphire}$, where $t_{sapphire}$ is the thickness of the sapphire and $k_{sapphire}$ is its thermal conductivity.

Phillips (2011) characterized the uncertainty associated with the pool boiling facility and heater testing. He reported that the uncertainty in the heat flux is 2% and at 175°C, the error in the temperature measurement is approximately 2.8% of the measurements readings. The full derivation for the uncertainty in the measurement can be found in [40]. We use these errors to determine the uncertainty in the heat transfer coefficient assuming that all the measured values are un-correlated:

$$h = \frac{q"}{\Delta T} \tag{4.1}$$

$$\delta h = \sqrt{\left(\frac{\partial h}{\partial q"}\delta q"\right)^2 + \left(\frac{\partial h}{\partial \Delta T}\delta \Delta T\right)^2} \tag{4.2}$$

$$\frac{\partial h}{\partial q"} = \frac{1}{\Delta T} \tag{4.3}$$

$$\frac{\partial h}{\partial T_w} = \frac{-q"}{(\Delta T)^2} \tag{4.4}$$

$$\delta q" = 2\% \tag{4.5}$$

$$\delta T_w = 2.8\% \tag{4.6}$$

$$\delta h = \sqrt{\left(\frac{0.02}{\Delta T}\right)^2 + \left(\frac{0.03q"}{(\Delta T)^2}\right)^2} = \frac{1}{\Delta T}\sqrt{(0.02)^2 + (0.028h)^2} \tag{4.7}$$

The maximum uncertainty calculated from the experimental data is approximately 11%.

Heater preparation, testing, and data analysis were carried out using the same procedure as O'Hanley [6]. The reader is therefore invited to read Section 4.4 of the aforementioned thesis for further details.

5. Separate effects investigation results

In this chapter, the results of the separate effects investigation are reviewed in depth. The surface analysis results are first discussed and provide significant insight on the fabrication method. Next, the boiling and heat transfer coefficient curves extracted from the IR imaging data are presented. Finally, the separate effects of thickness, pore size, and void fraction are presented. For each surface effect investigated, the CHF results, boiling curves, and HTC are compared and discussed.

5.1. SEM and FIB images

Nanoporous coatings were examined in an SEM in order to qualitatively analyze the structure of the porous coating and the size of the pores.

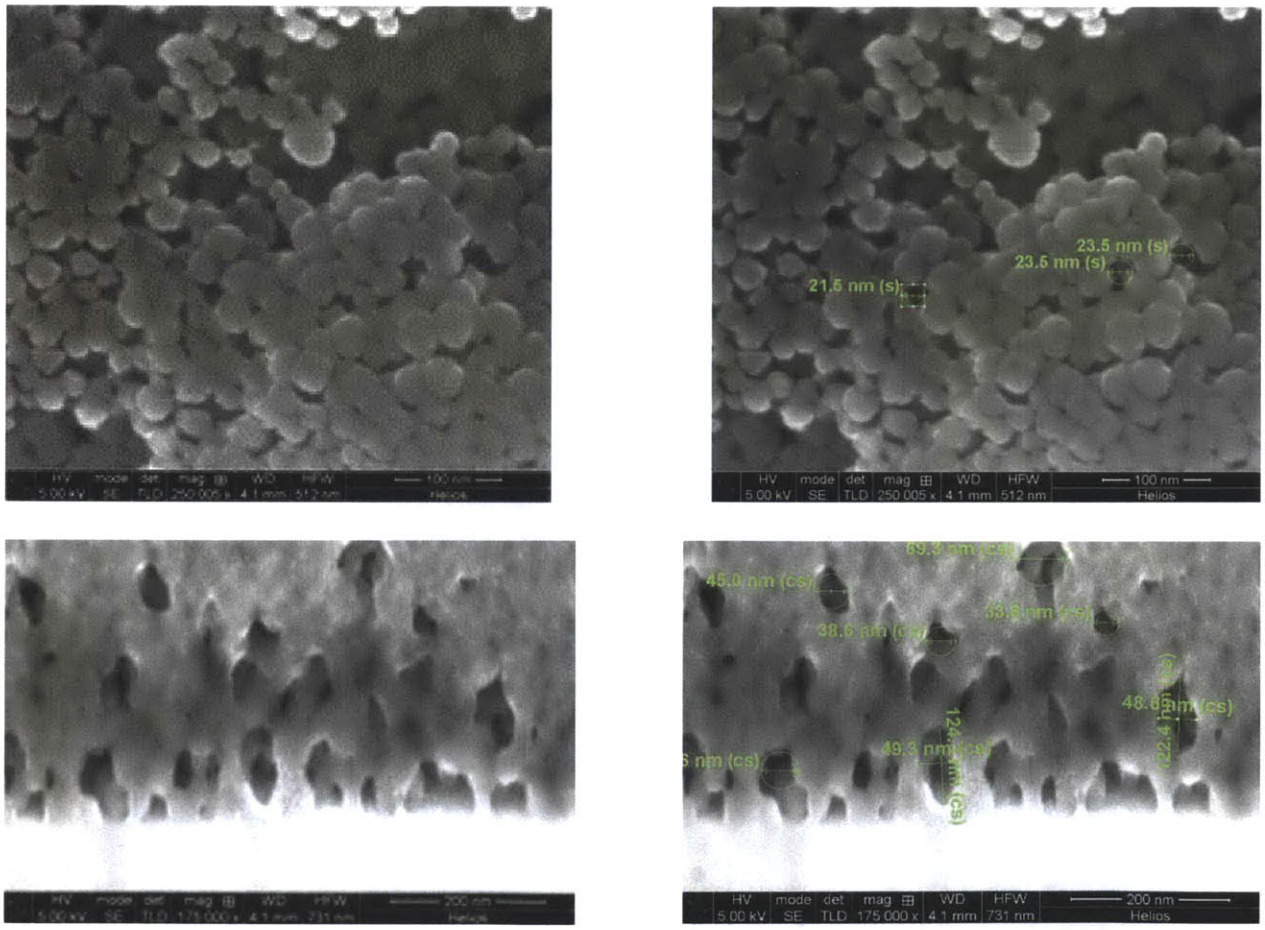

Figure 5-1 SEM images of 20 nm-diameter particle coatings. Top view (upper left), top view with sample void dimensions (upper right), cross-section (bottom left),cross-section with sample void dimensions (bottom right).

The first row of Figure 5-1 shows images of the surface of the coating where we can see that the particles are interspaced with voids approximately the size of the particles in the coatings. There also appears to be a larger void in the top right corner the size of several particle diameters.

The FIB was used to cut inside and obtain cross-sectional views of the coating. The "cutting" from the focused ion beam generated a smearing in the particles and a clear image could not readily be obtained. This is partially due to the nonconductive nature of the particles. Nevertheless it is possible to see the larger voids interspersed in the porous layer. From the measurements of a small sample of these voids, the larger cavities appear to be approximately ~40 μm which is approximately two particle diameters. One reason which could explain the presence of such voids is the potential for nanoparticles of a certain dimension to agglomerate and adsorb to the substrate in grape-like clusters, producing small irregularities in the porous layer.

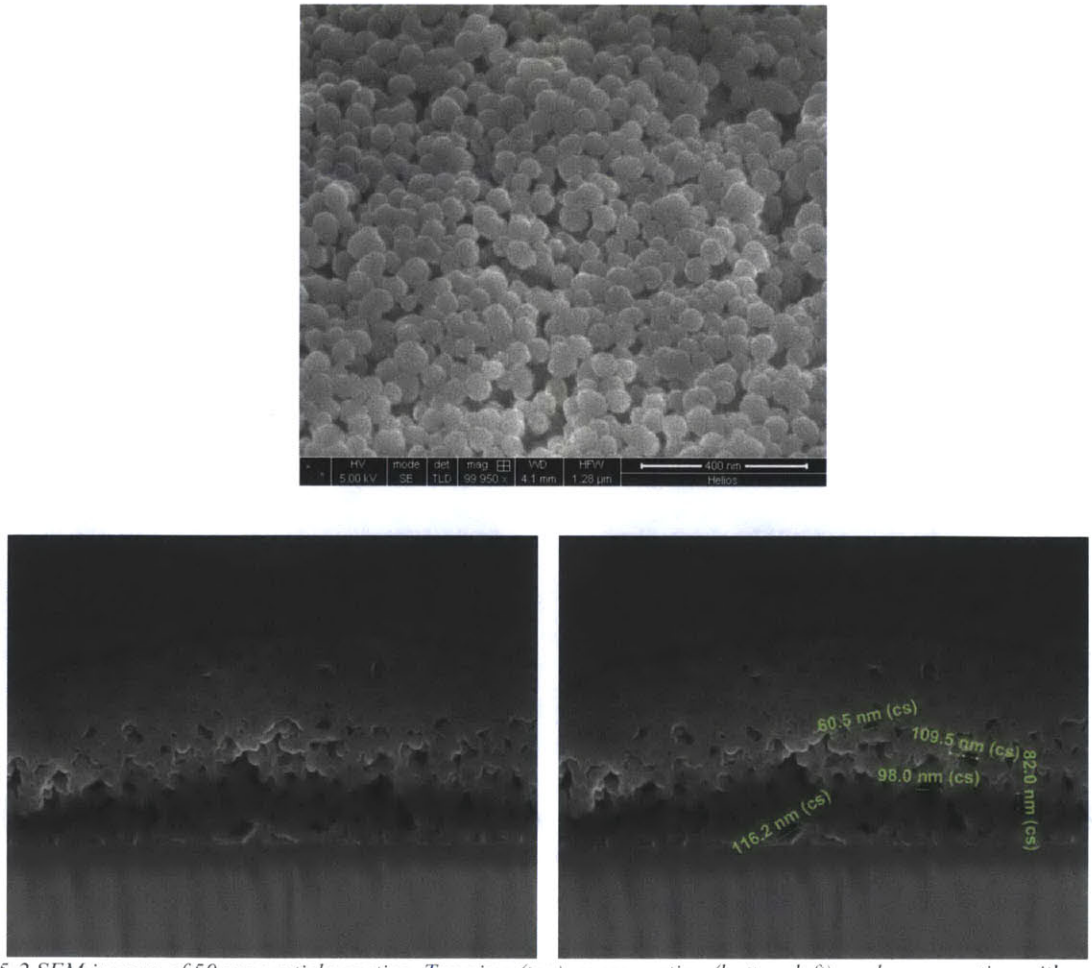

Figure 5-2 SEM images of 50 nm particle coating. Top view (top), cross-section (bottom left), and cross-section with sample void dimensions (bottom right).

Figure 5-2 shows a sample LbL coating with 50 nm particles. Similarly to the 20 nm particle coating, the 50 nm particles are interspersed with voids approximately the size of the particles with also larger voids approximately twice the size of the particle diameter. The porosity seems reduced near the surface of the coating which is likely due to the carbon coating which filled the voids in the upper layer.

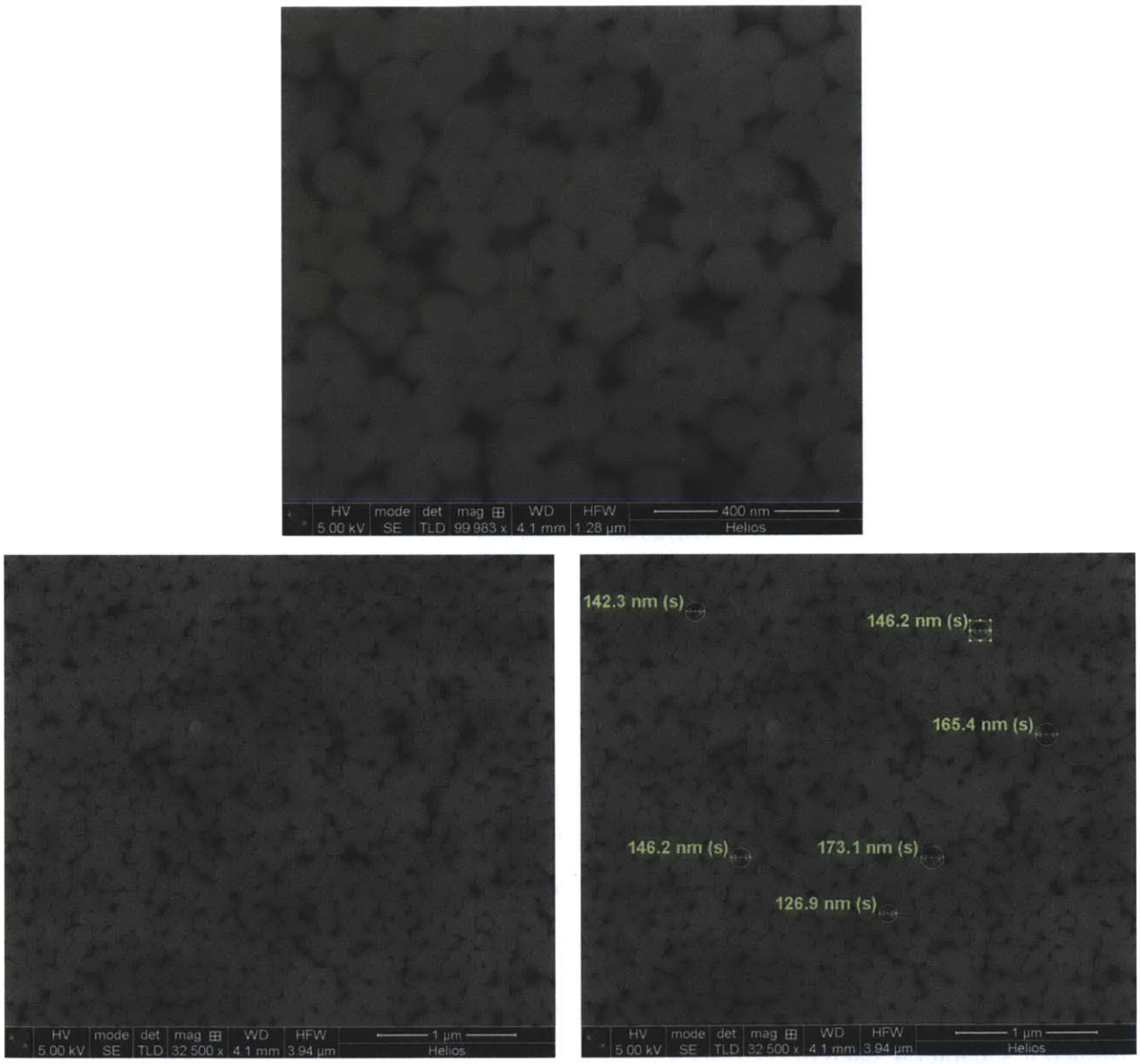

Figure 5-3 SEM images of 100 nm particle coating. Top view at high magnification (top), top view at lower magnification (bottom left), and top view with sample void dimensions (bottom right).

Figure 5-3 shows sample images of an LbL coating with 100nm particles. As with the previous coatings, voids appear to be on the order of the particle size, with some slightly large voids approximately twice the particle size. In addition, it can be seen in the image with the highest

magnification that the particles appear to have a texture on their surface and are not completely smooth. It should be noted that this particular porous coating was coated with gold rather than carbon and it was later found that gold does not appear as uniform as carbon at the nanometer scale. For this reason, it is generally recommended to use carbon for this type of application. However, gold was still used in certain cases since the coating application process is much more simple compared to carbon coating.

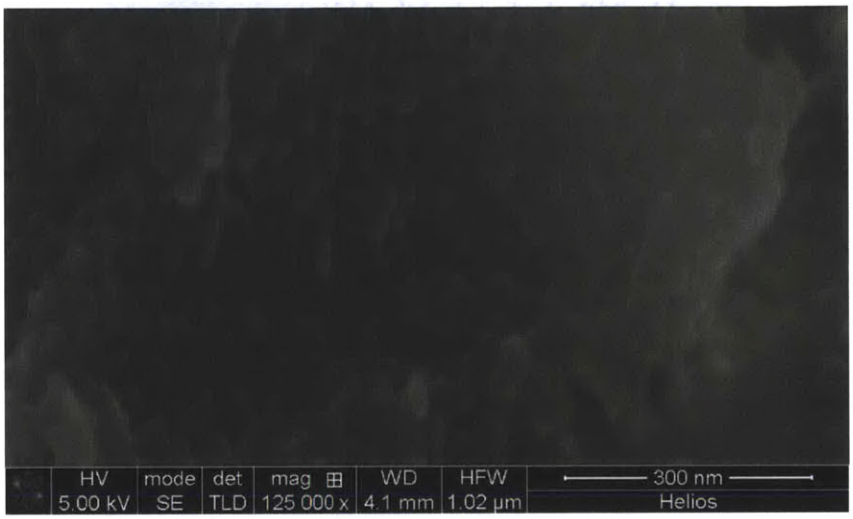

Figure 5-4 SEM images of 10 nm particle coatings.

Figure 5-4 is a surface image of a coating assembled with 10 nm particles. Since the particle size approaches the limit of the SEM's resolution, it was not possible to obtain very clear images and to make any qualitative observations for these coatings. Another potential reason for the poor image quality is the carbon coating used to make the surface conductive is several nanometers thick. Since the features in the porous layer are approximately the same size as the thickness of the carbon coating, the details are lost underneath the carbon layer. For the same reason, images of the 6 nm particle coatings were not obtained and are not discussed in this section.

Finally, Figure 5-5 shows images of porous layers with 60%, 40%, and 20% void fractions. As outlined in Chapter 4, each of the three coatings is composed of 20 nm particles and polymers are used to partially fill the pores to lower the standard 60% void fraction layers to 40% and 20%. The images show that the polymers uniformly coat each particle and fill mostly the smaller voids. Although some of the voids appear slightly smaller, they remain in general on the order of one to two times the particle diameter, i.e. 20 nm to 40 nm.

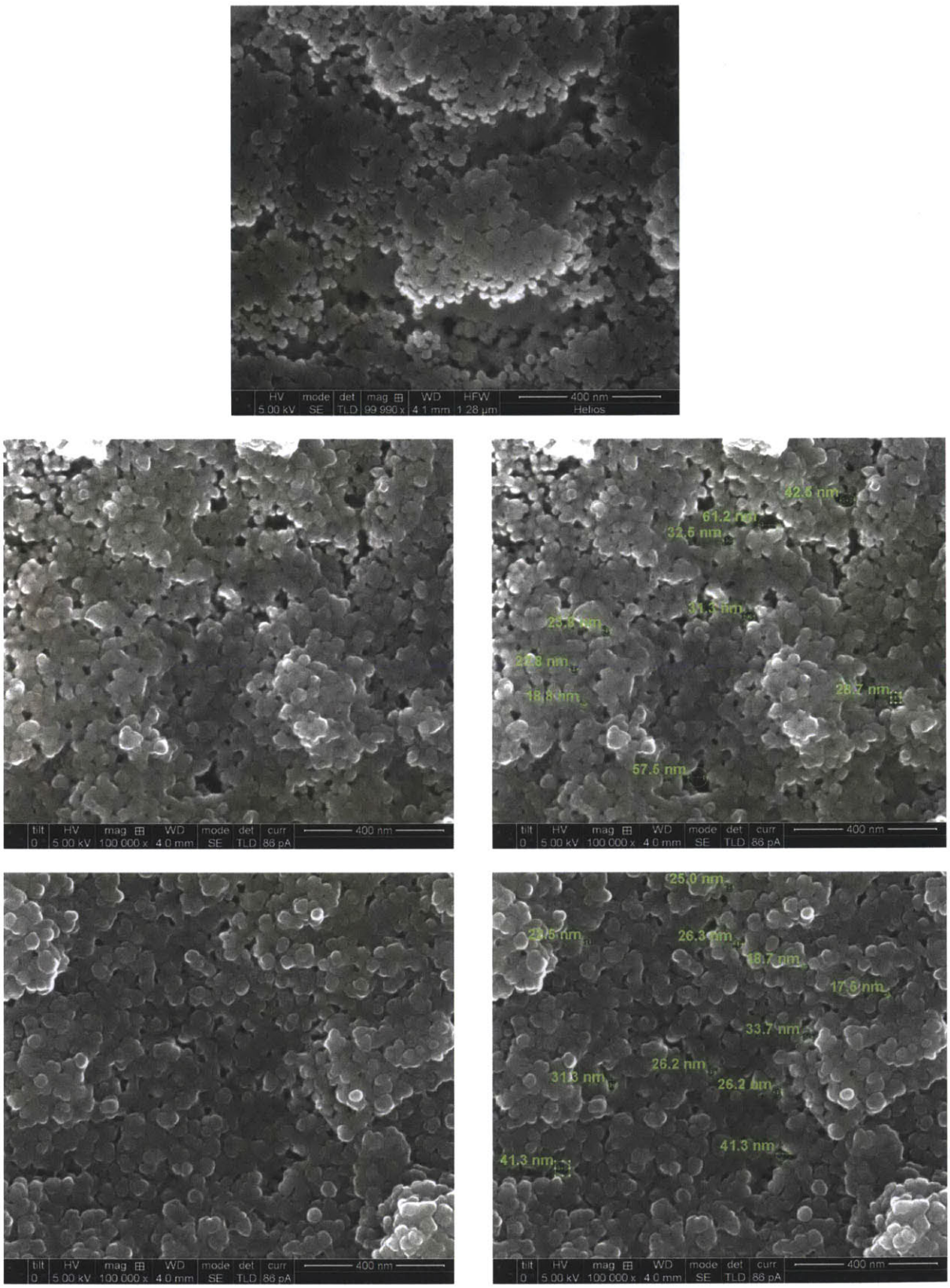

Figure 5-5 SEM images of porous surfaces with ~60% voids (top row), ~40% voids (middle row, left), ~40 voids with sample pore measurements (middle row, right), ~20% voids (bottom row, left), and ~20 voids with sample pore measurements (bottom row, right).

5.2. Profilometer measurements

5.2.1. Thickness measurements

The Stylus Profilometer was used to verify the thickness of the porous coatings. Since the growth rate varies for different particle sizes, the number of bilayers required to achieve a specific thickness was a trial-and-error process. The thickness data is summarized in Table 5-1.

Table 5-1 Thickness data obtained from Stylus Profilometer

Particle size (nm)	Number of Bilayers	Average Total Thickness (nm)	Thickness per Bilayer (nm)	Average Thickness per Bilayer (nm)	Standard Deviation (%)
100	52	1065	21	21	23.4
50	25	510	20	20	9.1
50	50	1071	21		1.4
50	110	2011	19		37.6
20	20	547	27	32	3.4
20	29	809	27		5.3
20	58	2016	35		3.2
20	77	2549	33		2.4
20	100	3693.6	37		7.6
10	56	1102	20	20	3.4
6	70	811	12	12	5.2
20 + 19 SPS/PAH bilayers	30	816	-	-	2.8
20 + 36 SPS/PAH bilayers	30	857	-	-	9.9

At least 4 measurements were obtained for each sample coating. Table 5-1 reveals that large variations in thickness per bilayer exist and there is no obvious correlation between particle size and thickness per bilayer. For example, 6 nm particles are over and order of magnitude smaller than 100 nm particles. However, the thickness per bilayer of the former is only half the thickness per bilayer of the latter. A variety of reasons could potentially explain these variations. One possibility may be that initial bilayers may not adsorb to the substrate as readily for large particles as they do for small particles. In addition, smaller particles tend to conglomerate and adsorb to the

substrate in small clusters rather than individually. Furthermore, the electrostatic forces present in the layer-by-layer assembly are not as effective at assembling larger, heavier particles.

The last two rows in Table 5-1 are allocated to the composite porous layer composed of a nanoparticle/polymer assembly and a polymer/polymer assembly. The thickness was engineered to match that of a system with only a nanoparticle/polymer assembly. It can be seen that the polymers do not contribute significantly to the overall thickness of the layer.

5.2.2. Roughness measurements

The Stylus Profilometer was also used to obtain roughness measurements. At least 4 measurements were obtained for each sample coating. The results are summarized in Table 5-2. In general, the roughness is less than 150 nm for all coatings. From the data for 50 nm particles and 20 nm particles, it can also be noted that the roughness increases with increasing thickness. This may be attributed to particles conglomerating over time in solution and adsorbing to the substrate in small clusters. This becomes more significant when a very large number of bilayers is applied. One potential way to obtain smoother surfaces and to maintain a more constant roughness at different thicknesses would be to change the nanoparticle solutions used every ~20 bilayers or so, but the method should be verified. Nevertheless, the roughness remains within an acceptable limit and is relatively smooth in all cases.

The roughness of the composite porous layers is greater than the roughness of the porous layers without the added polymer/polymer assembly. As the polymers assemble and penetrate the porous layer, some continue to build-up on the surface of the coating, which enhances the features contributing to the roughness at the surface.

Table 5-2 Roughness data obtained from Stylus Profilometer

Particle size (nm)	Number of Bilayers	Average Roughness R_a (nm)	Standard Deviation (%)
100	52	156	16.4
50	25	26	75.5
50	50	156	19.6
50	110	271	6.6
20	20	26	11.2
20	29	30	12.1
20	58	92	28.9
20	77	153	12.8
20	100	142	16.9
10	56	30	15.2
6	70	37	1.0
20 + 19 SPS/PAH bilayers	30	37	21.5
20 + 36 SPS/PAH bilayers	30	67	5.1

5.3. Porosity measurements (ellipsometry)

The Spectroscopic Ellipsometer was used to characterize the porosity (void fraction) of the surfaces. The Spectroscopic Ellipsometer is generally used to characterize thin films and its best range of accuracy is for films less than 500 nm. Measurements become increasingly difficult to obtain for thicker films. Since the thickness per bilayer does not vary significantly for different numbers of bilayers, it is assumed that the porosity remains approximately constant over the thickness range studied. In addition, the cross-sectional images acquired from the FIB/SEM do not appear to display any variations in porosity over the thickness. Thus, ellipsometry measurements were only obtained for film thicknesses of ~500 nm or less.

The results obtained from the porosity measurements are summarized in Table 5-3. The porosity varies between ~40% to ~60% in most cases and becomes significantly lower for the 6nm particles (36%). These particles may assemble more readily and uniformly than the larger particles and with less "pockets" inside the porous layers. The lower void fraction could also be attributed to residual PAH (cation in the nanoparticle/polymer LbL assembly) which remains trapped in the small pores

or assembles with a non-negligible thickness compared to the 6 nm particles. Higher resolution SEM images would be required to further understand these results.

Table 5-3 Void fraction data obtained from spectroscopic ellipsometry

Particle size (nm)	Average Porosity (%)	Porosity Standard Deviation (%)
100	65	6
50	57	10
20	63	1
10	42	5
6	36	5
20 +19 SPS/PAH bilayers	41	3
20 +36 SPS/PAH bilayers	22	3
6 nm + 100 nm	41	5

5.4. Contact angle measurements

The contact angle of all porous coatings with just the nanoparticle/PAH assembly (no SPS/PAH) was always less than 5°, therefore these surfaces were all superhydrophilic. The contact angle for the composite porous coatings with lower void fractions have slightly higher contact angles. As shown in Table 5-4, the contact angle for a bare surface coated with SPS/PAH polymers is 27°. When deposited on a porous surface, the texture of the surface further decreases the contact angle and the surfaces approach superhydrophilic states. There is however a significant standard deviation in the contact angle for these lower porosity coatings.

Table 5-4 Contact angle measurements for different porous coatings.

Sample description	Average contact angle (°)	Contact angle standard deviation (%)
Pure nanoparticle coating (6nm, 10nm, 20nm, 50nm, and 100nm particles)	<5.0°	0
Bare silicon wafer with 12 SPS/PAH bilayers	26.7°	7
20nm particles + 19 SPS/PAH bilayers (~40% void fraction)	4.5°	31
20nm particles + 36 SPS/PAH bilayers (~20% void fraction)	6.8°	38

5.5. Boiling curves

5.5.1. Pore size: ~100 nm / Layer thickness: ~1.0 μm / Porosity: ~50%

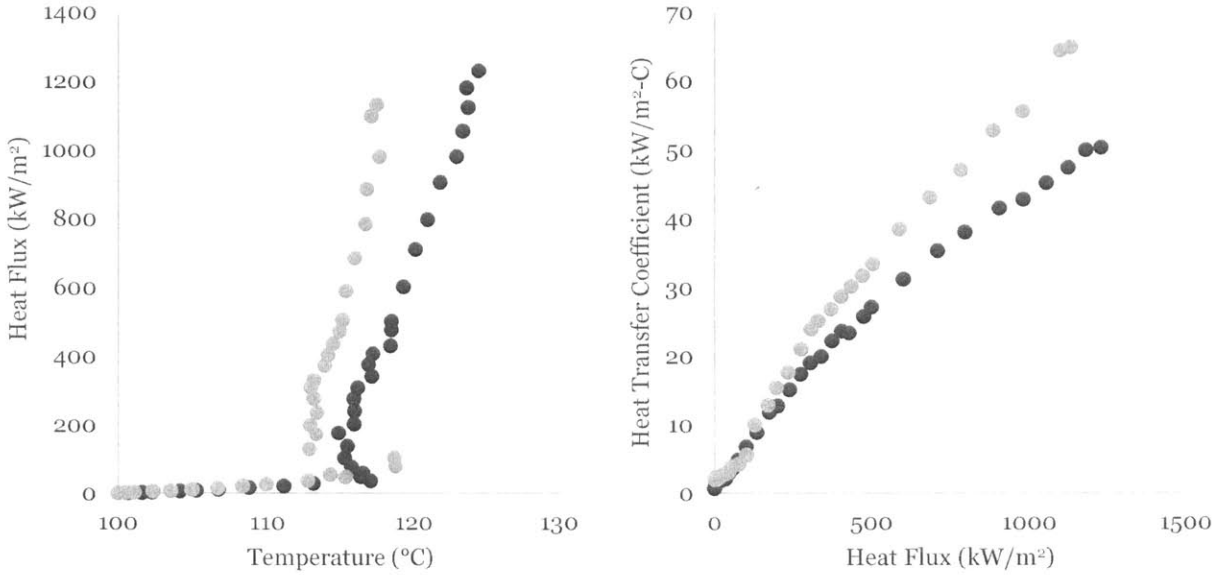

Figure 5-6 Boiling curve (left) and heat transfer coefficient (right) for ~100 nm pores, 1.0 μm thick, and ~50% void fraction. Maximum measurement uncertainties are: T≈2.8%, q"≈2%, and HTC≈11%.

5.5.2. Pore size: ~50 nm / Layer thickness: ~0.5 μm / Porosity: ~50%

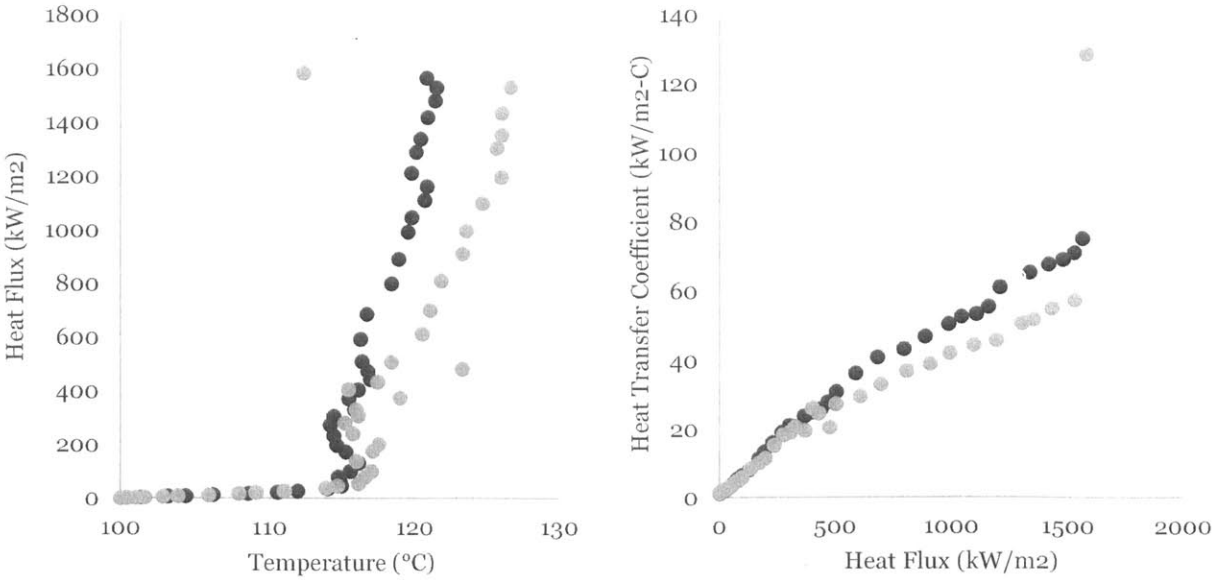

Figure 5-7 Boiling curve (left) and heat transfer coefficient (right) for ~50 nm pores, 0.5 μm thick, and ~50% void fraction. Maximum measurement uncertainties are: T≈2.8%, q"≈2%, and HTC≈11%.

5.5.3. Pore size: ~50 nm / Layer thickness: ~1.0 μm / Porosity: ~50%

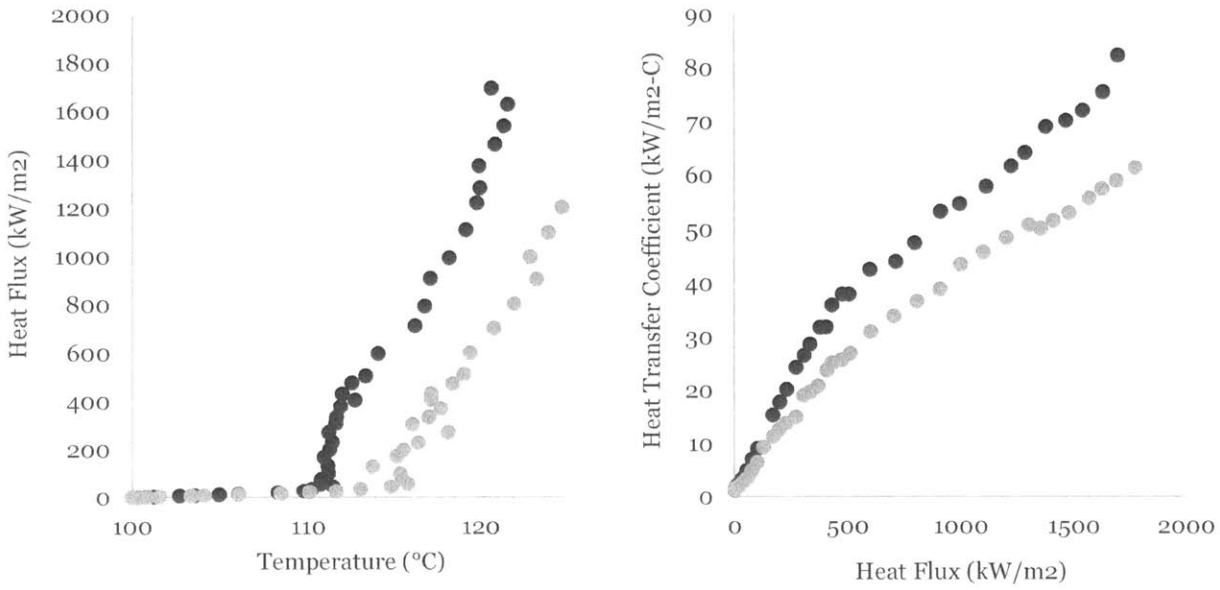

Figure 5-8 Boiling curve (left) and heat transfer coefficient (right) for ~50 nm pores, 1.0 μm thick, and ~50% void fraction. Maximum measurement uncertainties are: T≈2.8%, q"≈2%, and HTC≈11%.

5.5.4. Pore size: ~20 nm / Layer thickness: ~0.5 μm / Porosity: ~50%

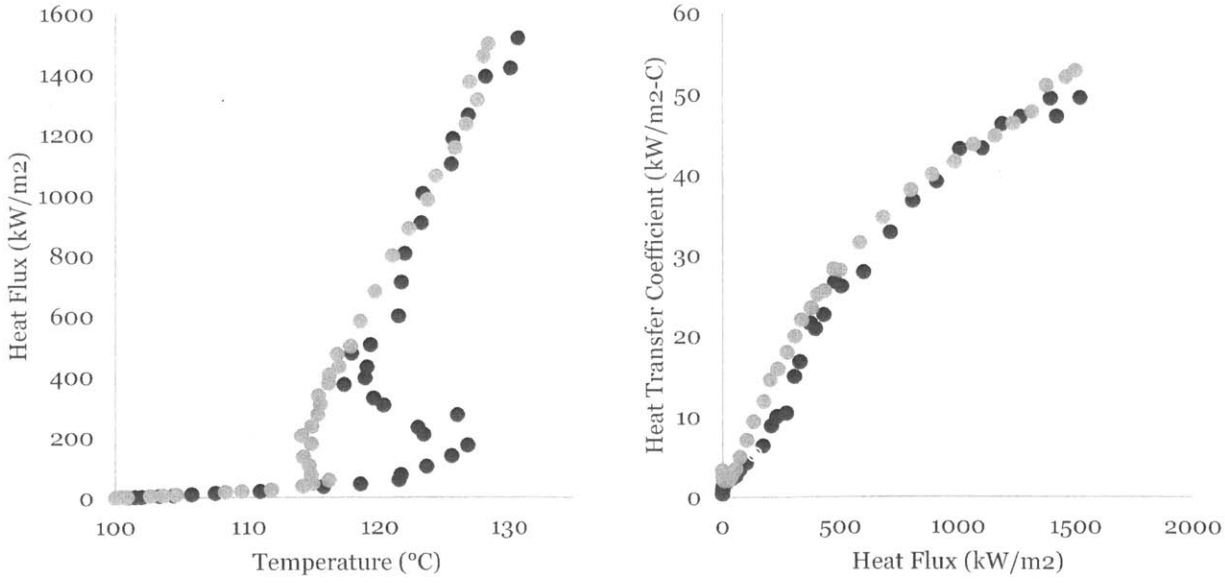

Figure 5-9 Boiling curve (left) and heat transfer coefficient (right) for ~20 nm pores, 0.5 μm thick, and ~50% void fraction. Maximum measurement uncertainties are: T≈2.8%, q"≈2%, and HTC≈11%.

5.5.5. Pore size: ~20 nm / Layer thickness: ~1.0 μm / Porosity: ~50%

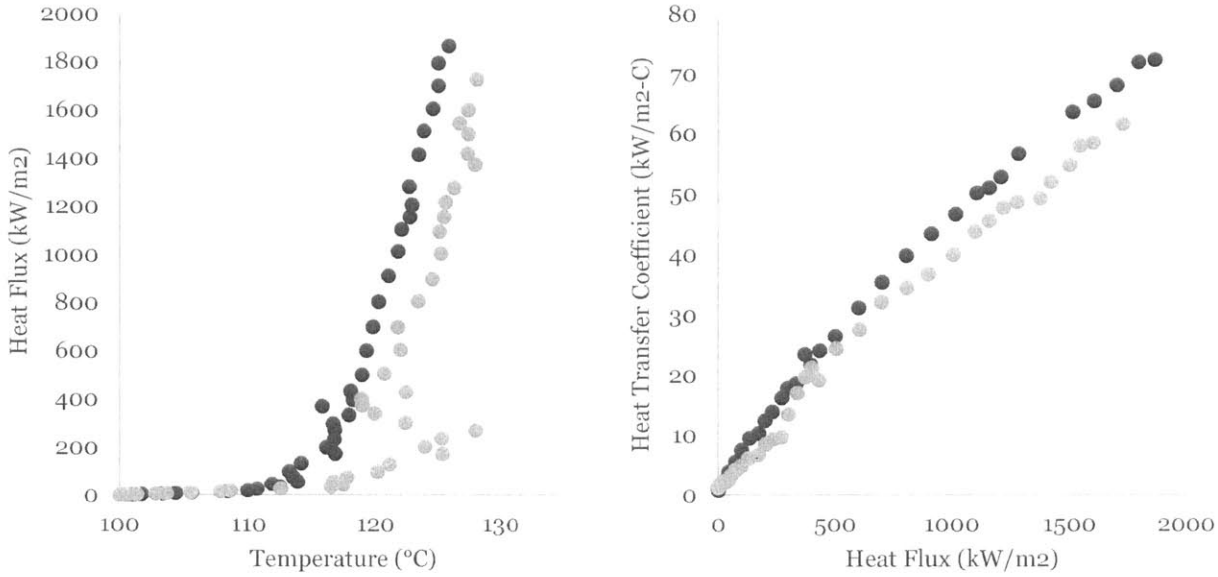

Figure 5-10 Boiling curve (left) and heat transfer coefficient (right) for ~20 nm pores, 1.0 μm thick, and ~50% void fraction. Maximum measurement uncertainties are: T≈2.8%, q"≈2%, and HTC≈11%.

5.5.6. Pore size: ~20 nm / Layer thickness: ~2.0 μm / Porosity: ~50%

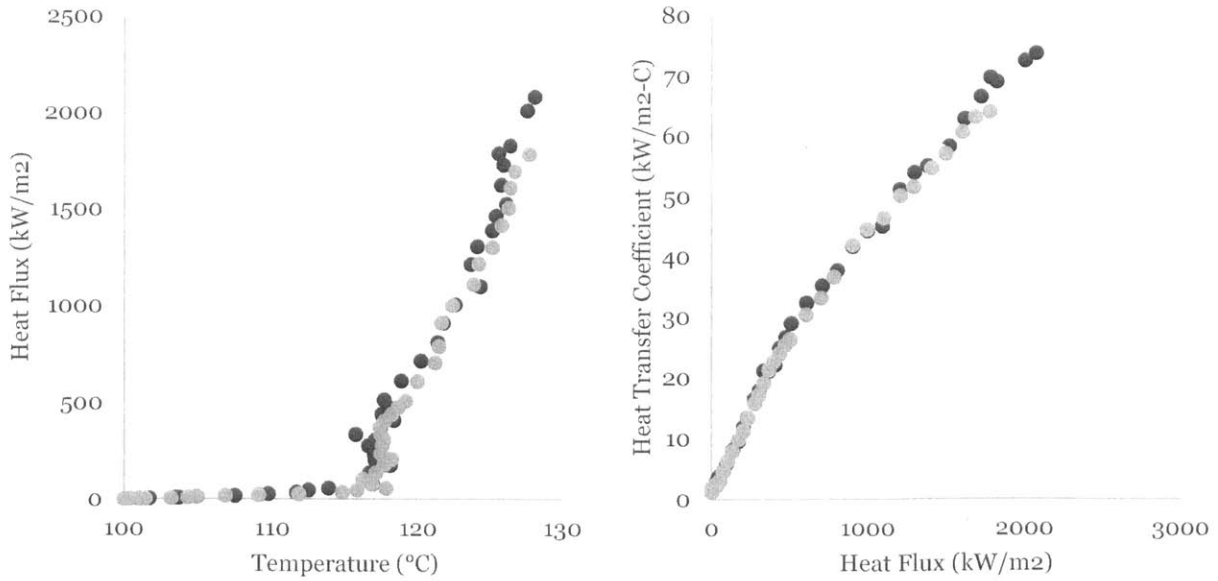

Figure 5-11 Boiling curve (left) and heat transfer coefficient (right) for ~20 nm pores, 2.0 μm thick, and ~50% void fraction. Maximum measurement uncertainties are: T≈2.8%, q"≈2%, and HTC≈11%.

5.5.7. Pore size: ~20 nm / Layer thickness: ~2.5 μm / Porosity: ~50%

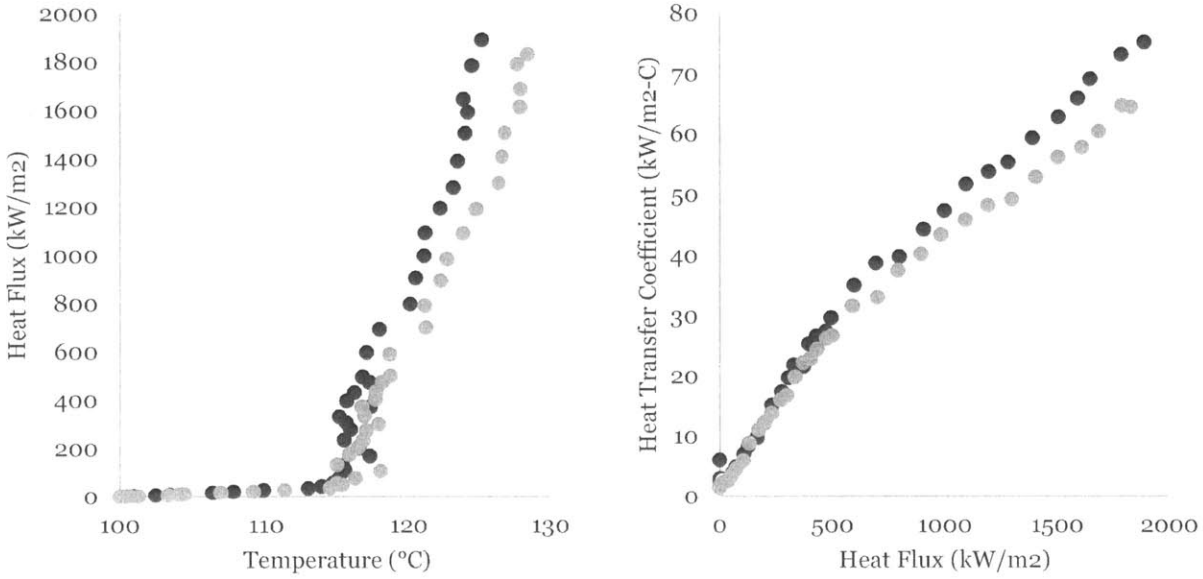

Figure 5-12 Boiling curve (left) and heat transfer coefficient (right) for ~20 nm pores, 2.5 μm thick, and ~50% void fraction. Maximum measurement uncertainties are: T≈2.8%, q"≈2%, and HTC≈11%.

5.5.8. Pore size: ~20 nm / Layer thickness: ~3.5 μm / Porosity: ~50%

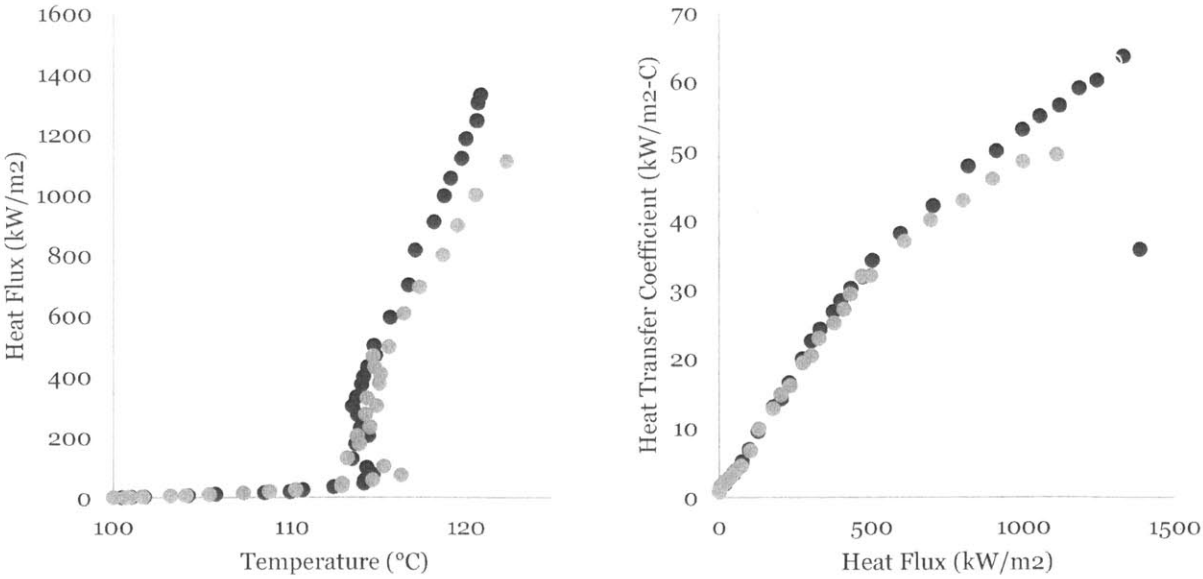

Figure 5-13 Boiling curve (left) and heat transfer coefficient (right) for ~20 nm pores, 4.0 μm thick, and ~50% void fraction. Maximum measurement uncertainties are: T≈2.8%, q"≈2%, and HTC≈11%.

5.5.9. Pore size: ~10 nm / Layer thickness: ~1.0 μm / Porosity: ~50%

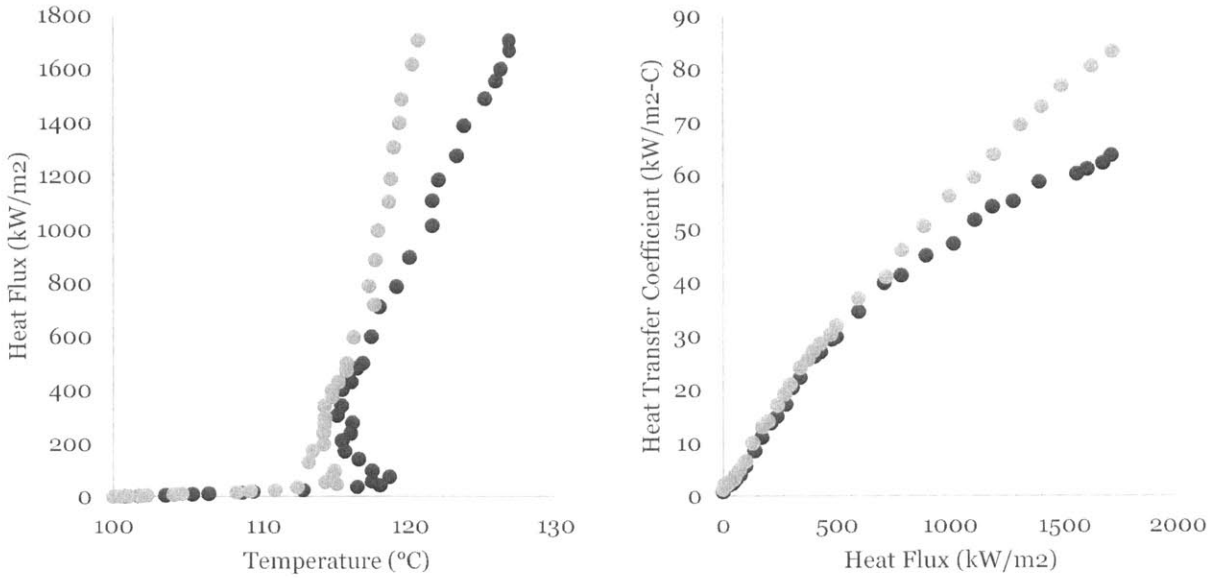

Figure 5-14 Boiling curve (left) and heat transfer coefficient (right) for ~10 nm pores, 1.0 μm thick, and ~50% void fraction. Maximum measurement uncertainties are: T≈2.8%, q"≈2%, and HTC≈11%.

5.5.10. Pore size: ~6 nm / Layer thickness: ~1.0 μm / Porosity: ~50%

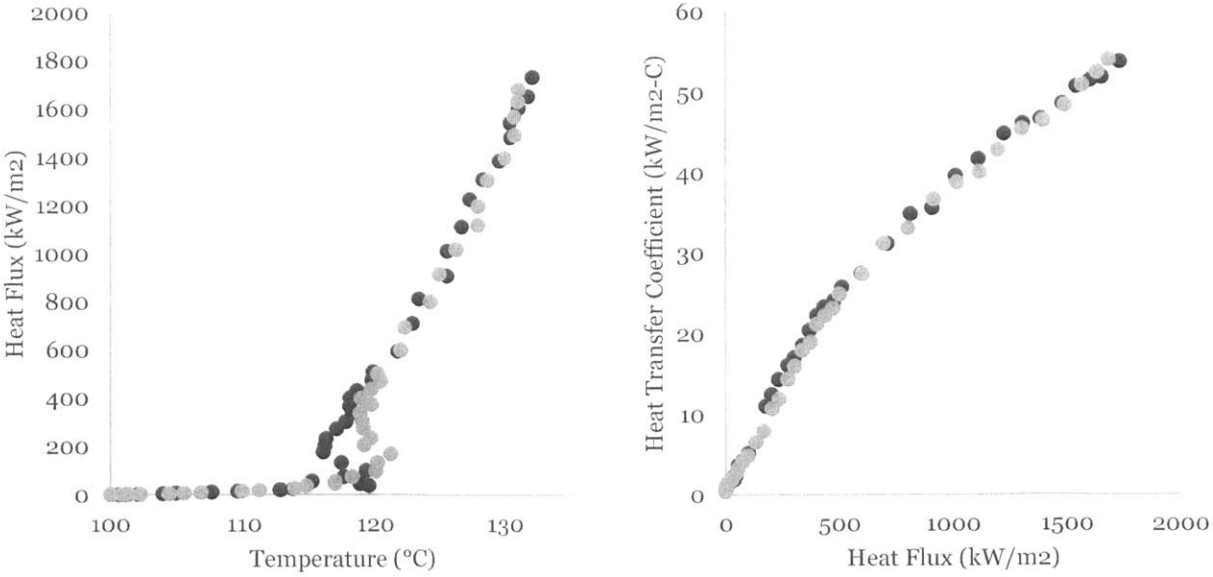

Figure 5-15 Boiling curve (left) and heat transfer coefficient (right) for ~6 nm pores, 1.0 μm thick, and ~50% void fraction. Maximum measurement uncertainties are: T≈2.8%, q"≈2%, and HTC≈11%.

5.5.11. Pore size: ~20 nm / Layer thickness: ~1.0 μm / Porosity: ~40%

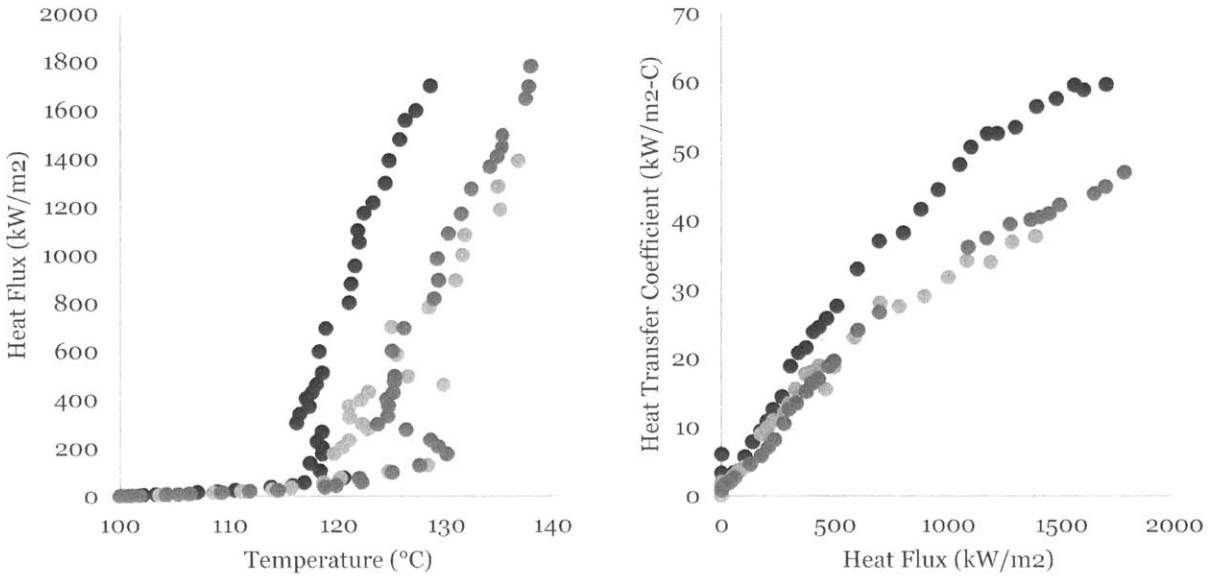

Figure 5-16 Boiling curve (left) and heat transfer coefficient (right) for ~20 nm pores, 1.0 μm thick, and ~40% void fraction. Maximum measurement uncertainties are: T≈2.8%, q"≈2%, and HTC≈11%.

5.5.12. Pore size: ~20 nm / Layer thickness: ~1.0 μm / Porosity: ~20%

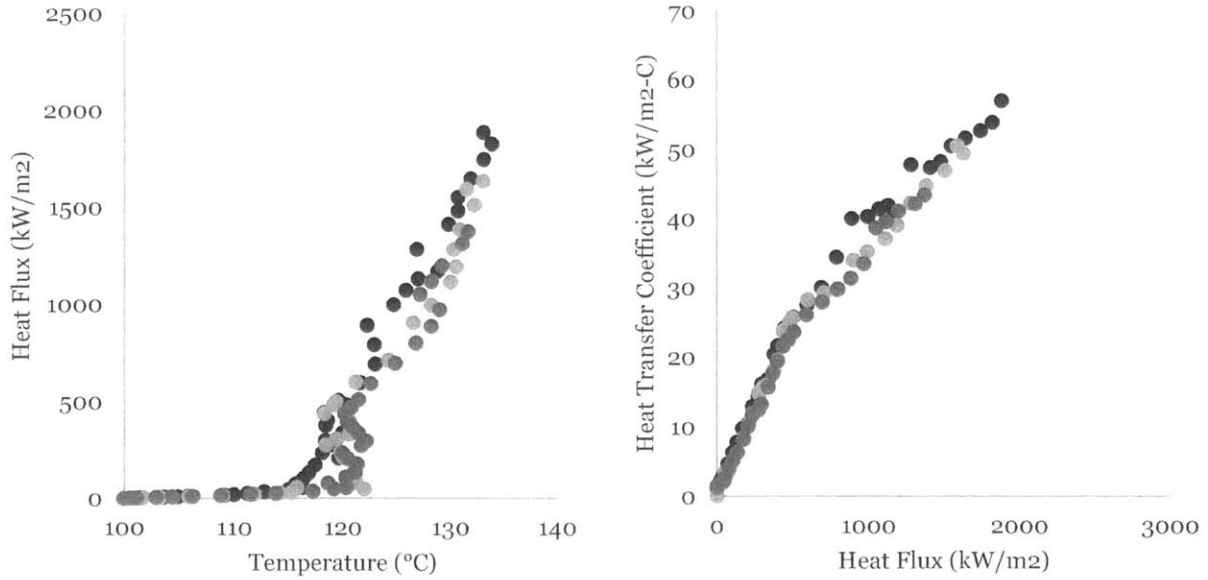

Figure 5-17 Boiling curve (left) and heat transfer coefficient (right) for ~20 nm pores, 1.0 μm thick, and ~20% void fraction. Maximum measurement uncertainties are: T≈2.8%, q"≈2%, and HTC≈11%.

5.6. Effect of porous layer thickness

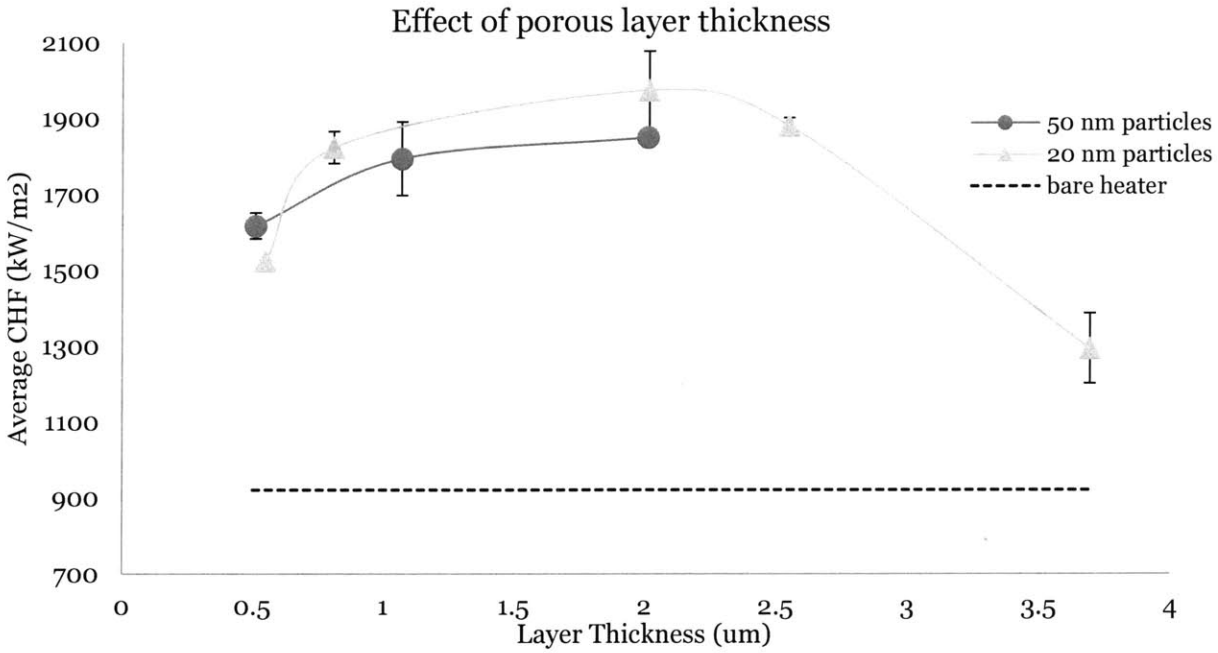

Figure 5-18 CHF versus porous layer thickness, all other parameters constant.

Table 5-5 Data summary for study of the effects of porous layer thickness on CHF. Bare heater data from O'Hanley [12].

Test #	Particle Size (nm)	Layer Thickness (um)	R_a (nm)	Void Fraction (%)	Static contact angle	CHF (kW/m²)		
						1	2	Average
0	none (bare heater)	-	-	-	74.7°	-	-	920
1	50	0.51	26	57	<5°	1582	1650	1616
2	50	1.07	156	57	<5°	1696	1890	1793
3	50	2.01	271	57	<5°	1837	1860	1849
4	20	0.55	26	63	<5°	1520	1525	1523
5	20	0.81	30	63	<5°	1780	1865	1823
6	20	2.02	92	63	<5°	1870	2076	1973
7	20	2.55	153	63	<5°	1859	1900	1880
8	20	3.69	142	63	<5°	1200	1385	1293

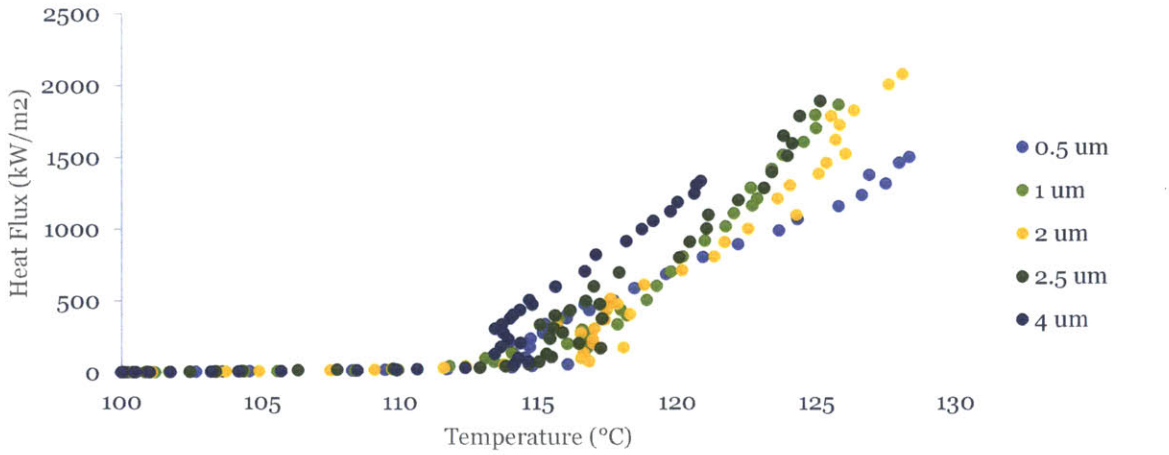

Figure 5-19 Comparison of boiling curves for porous layers with ~20 nm pores and different layer thicknesses (one characteristic curve is chosen for each porous layer type). Maximum measurement uncertainties are: T≈2.8% and q"≈2%.

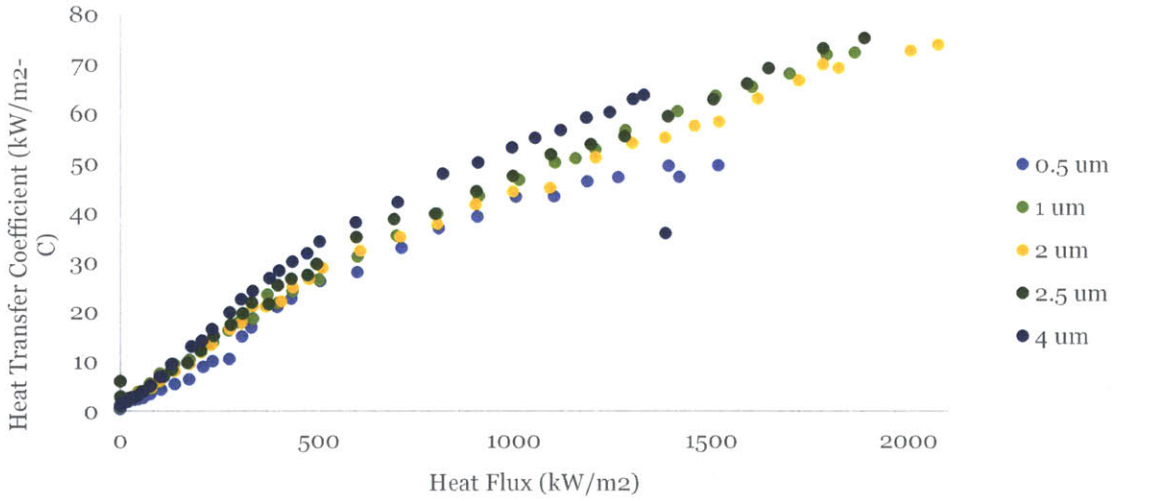

Figure 5-20 Comparison of heat transfer coefficient for porous layers with~20 nm pores and different layer thicknesses (one characteristic curve is chosen for each porous layer type). Maximum measurement uncertainties are: HTC≈11% and q"≈2%.

From Figure 5-18, it should be noted that the bars at each data point in this figure are not error bars, they are in fact range bars, with the point indicating the average and bars the maximum and minimum values obtained. The error bars are expressed in this way as experimental repeatability resulted in much more uncertainty than experimental equipment inaccuracies. It is clear that CHF increases with increasing thickness However, this effect saturates and CHF drops for very large thickness. For the 20 nm particles, the highest CHF is achieved with a 2 μm-thick porous layer at which point the average CHF is 1973 kW/m^2, a 114% enhancement. For the 50 nm particles, the highest CHF was also achieved with a 2 μm-thick porous layer, but since the porous layer was not further increased due to complications in the fabrication method, it is not possible to determine if

this is in fact the thickness at which the CHF peaks for this particle size or if it is reached at a greater thickness. Finally, Figure 5-20 shows that the HTC continues to increase with increasing thickness and does not peak like CHF does.

5.7. Effect of pore size

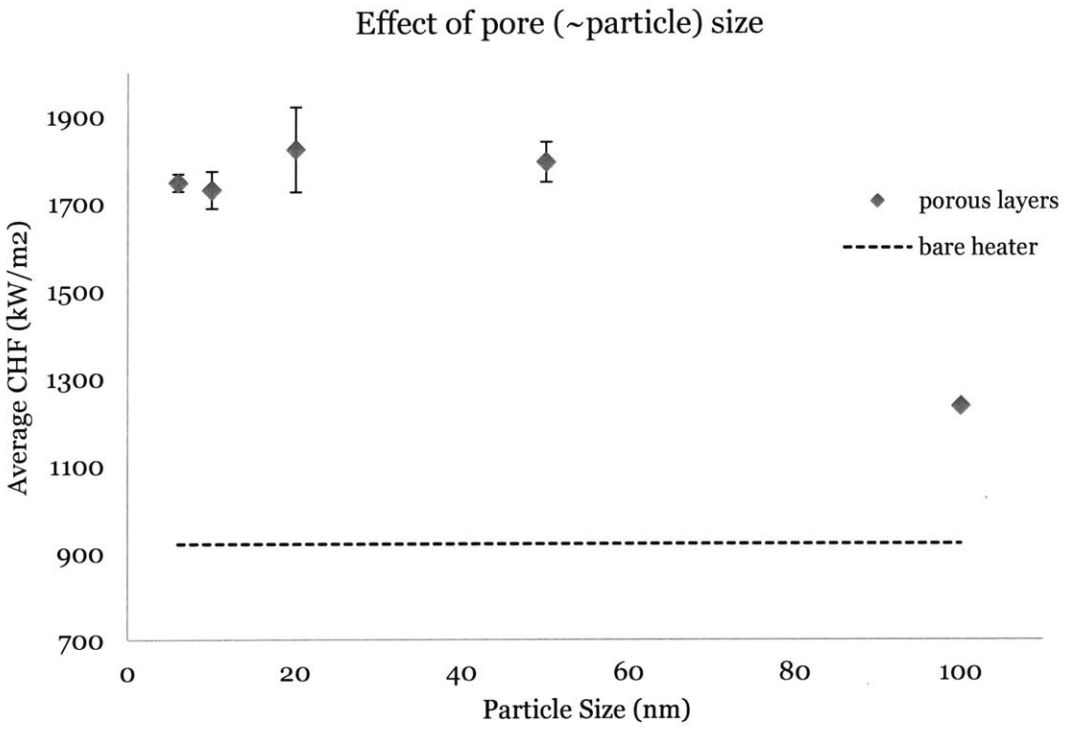

Figure 5-21 CHF versus pore size (~particle size), all other parameters constant (1 μm thickness).

Table 5-6 Data summary for study of the effects of pore size on CHF. Bare heater data from O'Hanley [12].

Test #	Particle Size (nm)	Layer Thickness (um)	R_a (nm)	Void Fraction (%)	Static contact angle	CHF (kW/m²)		
						1	2	Average
0	none (bare heater)	-	-	-	74.7°	-	-	920
1	6	0.81	37	36	<5°	1743	1750	1747
2	10	1.10	30	42	<5°	1710	1750	1730
3	20	0.81	30	63	<5°	1780	1865	1823
4	50	1.07	156	57	<5°	1696	1890	1793
5	100	1.07	156	65	<5°	1189	1280	1235

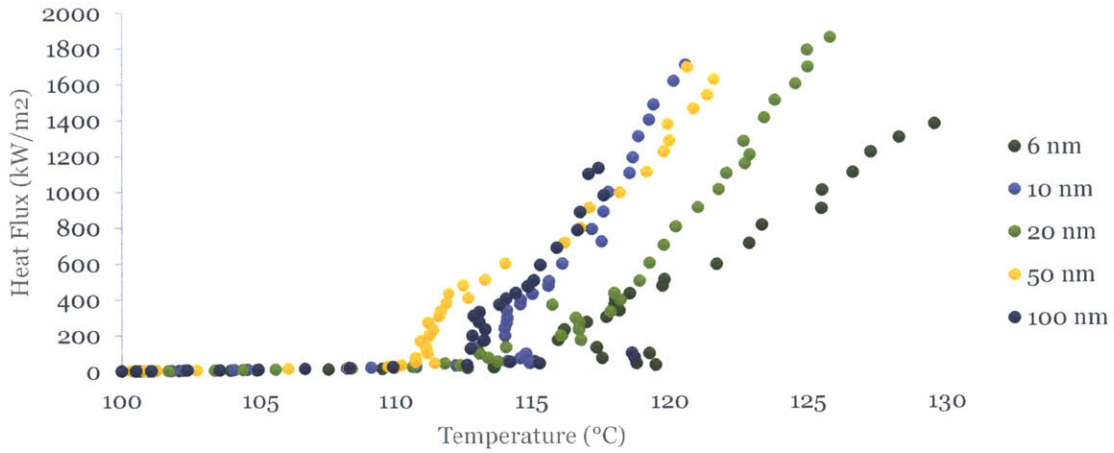

Figure 5-22 Comparison of boiling curves for porous layers ~1.0 μm thick and different pore sizes (one characteristic curve is chosen for each porous layer type). Maximum measurement uncertainties are: T≈2.8% and q"≈2%.

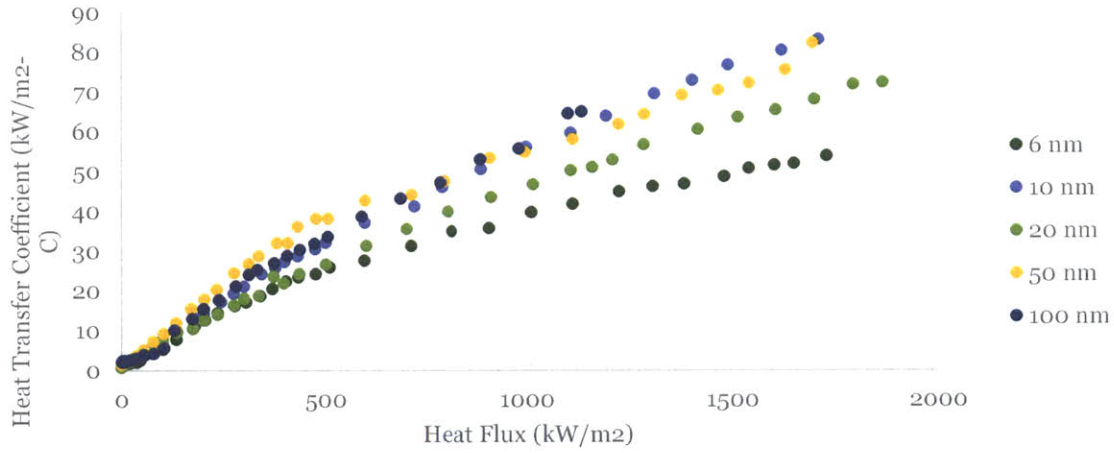

Figure 5-23 Comparison of heat transfer coefficient for porous layers ~1.0 μm thick and different pore sizes (one characteristic curve is chosen for each porous layer type). Maximum measurement uncertainties are: HTC≈11% and q"≈2%.

As previously noted, the bars at each point in Figure 5-21 are range bars, not error bars. In this case, the CHF reaches a peak for 20 nm particles and then decreases with increasing particle size. This suggests that the capillary wicking is heavily dependent on pore size. The CHF at this maximum is 1822.5 kw/m^2, a 98% enhancement. CHF for the 6 nm particles is slightly higher than for the 10 nm particles. However, the porosity is significantly lower for the 6 nm particles compared to all other particle sizes used, meaning that not all other parameters were kept constant and could explain the difference in the trend. Finally, Figure 5-23 shows that the HTC follows somewhat an opposite trend and in this case HTC increases with increasing particle size. However due to experimental error this trend is not clear.

5.8. Effect of void fraction

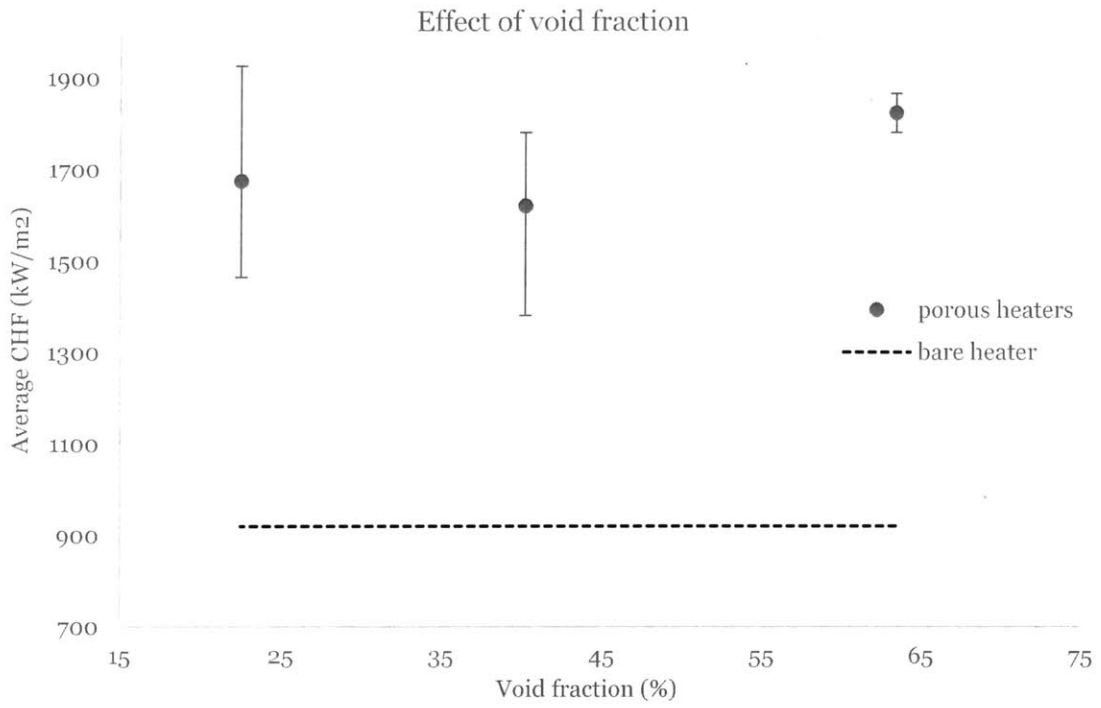

Figure 5-24 CHF versus void fraction, all other parameters ~constant.

Table 5-7 Data summary for study of the effects of void fraction on CHF. Bare heater data from O'Hanley [12].

Test #	Layer Thickness (um)	R_a (nm)	Void Fraction (%)	Static contact angle	CHF (kW/m^2)				
					1	2	3	Avg.	Std. dev. (%)
0	None (bare heater)	-	-	74.7°	-	-	-	920	-
1	0.81	30	63	<5°	1780	1865	-	1823	-
2	0.82	37	40	4.5°	1700	1381	1780	1620	211
3	0.86	67	22	6.8°	1925	1632	1465	1674	233

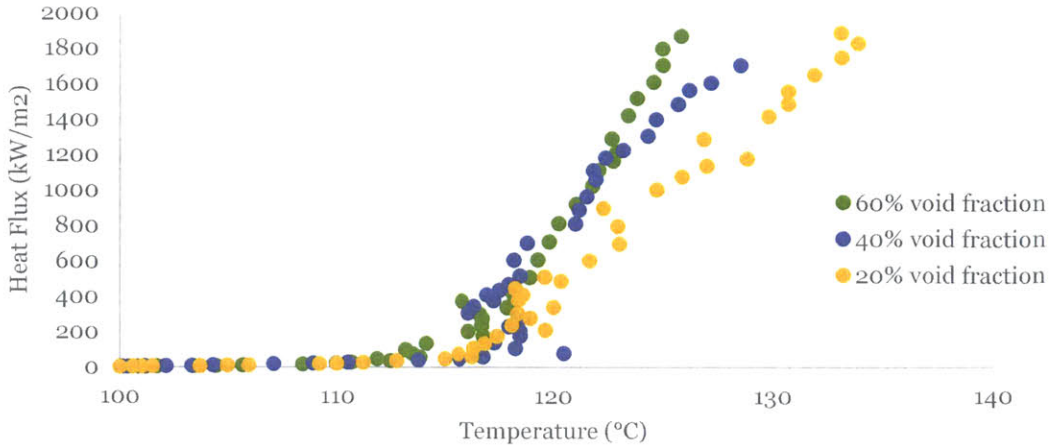

Figure 5-25 Comparison of boiling curves for porous layers ~1.0 μm thick, 20 nm particles, and different void fractions (one characteristic curve is chosen for each porous layer type). Maximum measurement uncertainties are: T≈2.8% and q"≈2%.

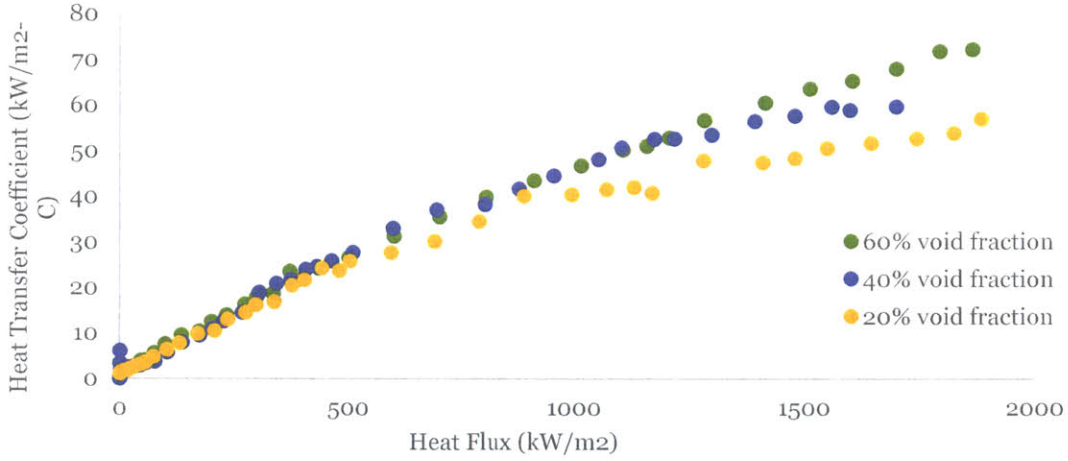

Figure 5-26 Comparison of heat transfer coefficient for porous layers ~1.0 μm thick, 20 nm particles, and different void fractions (one characteristic curve is chosen for each porous layer type). Maximum measurement uncertainties are: HTC≈11% and q"≈2%.

Figure 5-24 summarizes the results on the effects of void fraction on CHF. The highest CHF is achieved with the standard 60% void fraction (1822.5 kW/m^2, 98% enhancement). CHF is less for the 40% and 20% void fractions, but there is still significant enhancement of approximately 80% in both cases. There is also a large spread on the data for the two lower void fractions and additional experiments would be required to reduce the error. CHF is expected to decrease with decreasing void fraction as these surfaces approach smooth surfaces with no porosity or texture. The results agree with these expectations and suggest that it is possible to enhance CHF as long as there is interconnected porosity. From Figure 5-26, the HTC appears to be nearly identical for all void

fractions at heat fluxes below 1000 kW/m^2. Beyond this point, HTC increases with increasing void fraction.

5.9. Discussion and Model Development

Figure 5-27 demonstrates the postulated physical mechanisms which could explain some of the results observed. A substrate is coated with a porous material. The liquid is drawn in via capillary forces but is also opposed by viscous forces. The liquid then gets heated inside the pores, and finally escapes the porous layer as a vapor. The competition between the capillary forces and the viscous forces, which together characterize the permeability of the layer, may explain the peaks in the data for each parameter studied.

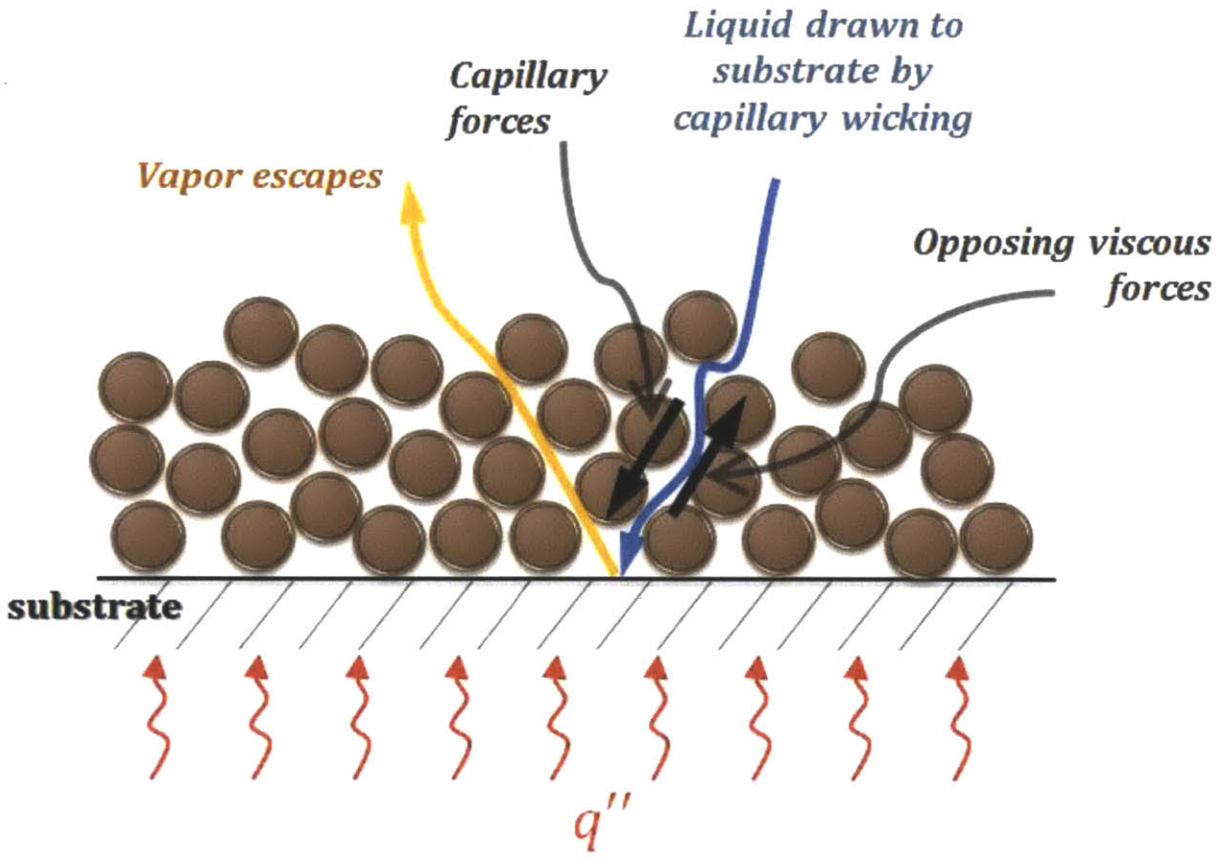

Figure 5-27 Postulated physical mechanisms involved in the effects of porosity on CHF.

We recall from Chapter 2 that O'Hanley [12] identified a set of non-dimensional parameters governing the wicking through the porous layer and that can be used to create a model for CHF. These governing parameters are ε and β, the ratio D_p/L, and the pore Reynolds number

$$Re_p \equiv \frac{\rho_f \sigma D_p}{\mu_f^2}, \tag{2.8}$$

where ε is the void fraction, D_p is the effective pore diameter, L is the effective pore length, β is the intrinsic contact angle , σ is the surface tension, μ_f is the fluid viscosity, and ρ_f is the fluid density. Table 5-8 summarizes all the surface parameters of all the porous layers tested, the corresponding non-dimensionalized parameters, and the CHF results. Figure 5-24 in Section 5.8 gives the effect of CHF versus ε, and Figure 5-21 in Section 5.7 gives the effects of CHF versus Re_p since Re_p is directly proportional to D_p. We now consider Figure 5-28 which gives the effect of the parameter D_p/L. This parameter allows to combine the effect of thickness and pore size on a single plot. We note that both effects demonstrate ascending and descending trends even though the curves do not entirely match together in the figure.

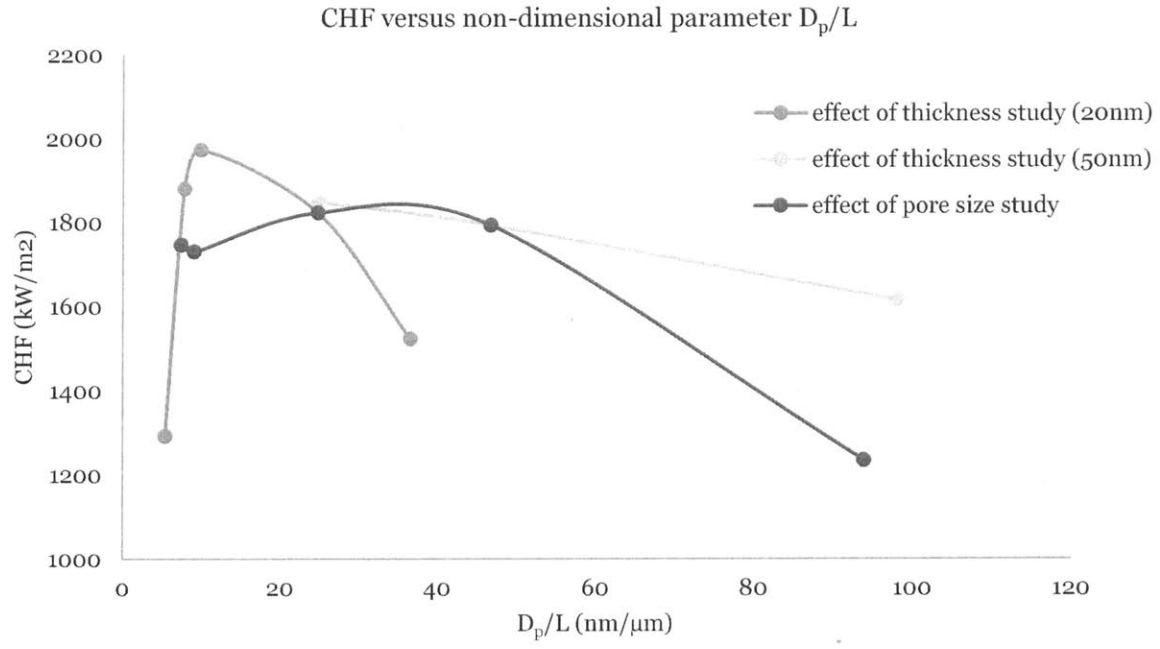

Figure 5-28 Effect of non-dimensional parameter D_p/L on CHF.

Table 5-8 Summary of porous layer surface characteristics measurements, non-dimensionalized parameters, and CHF results. D_p:pore diameter, L: Porous layer thickness, $Re_{p,f}$: Fluid Pore Reynolds number, $Re_{p,g}$: Gas Pore Reynolds number, ε: Void fraction (porosity)

	Case #	D_p (nm)	L (um)	D_p/L (nm/μm)	$Re_{p,f}$	$Re_{p,g}$	ε	Static contact angle β (°)	Static contact angle β rad	CHF_{avg} (kW/m²)	$\frac{CHF_{avg}}{CHF_{bare\ heater}}$
Effect of layer thickness	1	20	0.55	37	14	5	0.63	0	0	1523	1.65
	2*	20	0.81	25	14	5	0.63	0	0	1823	1.98
	3	20	2.02	10	14	5	0.63	0	0	1973	2.14
	4	20	2.55	8	14	5	0.63	0	0	1880	2.04
	5	20	3.69	5	14	5	0.63	0	0	1293	1.40
	6	50	0.51	98	36	12	0.57	0	0	1616	1.76
	7**	50	1.07	47	36	12	0.57	0	0	1793	1.95
	8	50	2.01	25	36	12	0.57	0	0	1848	2.01
Effect of pore size	9	6	0.81	7	4	1	0.36	0	0	1747	1.90
	10	10	1.10	9	7	2	0.42	0	0	1730	1.88
	2*	20	0.81	25	14	5	0.63	0	0	1823	1.98
	7**	50	1.07	47	36	12	0.57	0	0	1793	1.95
	11	100	1.07	94	71	23	0.65	0	0	1235	1.34
Effect of void fraction	2*	20	0.81	25	14	5	0.63	0	0	1823	1.98
	12	20	0.82	25	14	5	0.40	4.5	0.04	1620	1.76
	13	20	0.86	23	14	5	0.22	6.8	0.06	1674	1.82

We now consider a model based on the competing effects of capillary pressure and viscous pressure drops in a pore. We assume that the porous layer is composed of an array of parallel capillary tubes of equal diameter. We begin with the capillary pressure

$$P_{capillary} = \frac{2\sigma cos\theta}{r_p} = \frac{4\sigma cos\theta}{D_p} \tag{5.1}$$

The viscous pressure loss is the sum of the liquid friction and vapor friction. a is the location of the evaporation front inside the pore, such that $0 < a < L$. We obtain the equation for the viscous pressure losses

$$\Delta P_{viscous} = f_f \frac{a}{D_p} \frac{{G_p}^2}{2\rho_f} + f_g \frac{(L-a)}{D_p} \frac{{G_p}^2}{2\rho_g} = \frac{{G_p}^2}{2D_p} \left(\frac{f_f a}{\rho_f} + \frac{f_g (L-a)}{\rho_g} \right) \tag{5.2}$$

Where ρ_g is the vapor density, ρ_f is the liquid density, and G_p is the mass flux through the pore. Assuming laminar, fully developed flow in the pores, the friction factors are

$$f_f = \frac{64}{Re_{p,f}}, f_g = \frac{64}{Re_{p,g}} \tag{5.3}$$

And the liquid and vapor Reynolds numbers in the pore are

$$Re_{p,f} = \frac{G_p D_p}{\mu_f}, Re_{p,g} = \frac{G_p D_p}{\mu_g} \tag{5.4}$$

The viscous pressure drop can now be expressed as

$$\Delta P_{viscous} = \frac{32 G_p}{D_p^2} \left(\frac{\mu_f a}{\rho_f} + \frac{\mu_g (L-a)}{\rho_g} \right) \tag{5.5}$$

We assume steady-state flow inside the pores, therefore capillary pressure equals the total viscous pressure drop. Equating the two we have

$$\frac{32 G_p}{D_p^2} \left(\frac{\mu_f a}{\rho_f} + \frac{\mu_g (L-a)}{\rho_g} \right) = \frac{4\sigma cos\theta}{D_p} \tag{5.6}$$

and solving for G_p in Eq. 5.6, the mass flux in a single pore is therefore

$$G_p = \frac{D_p \sigma cos\theta}{8\left(\frac{\mu_f a}{\rho_f} + \frac{\mu_g (L-a)}{\rho_g}\right)} \tag{5.7}$$

The total mass flux per unit area through the porous layer becomes

$$G_{total} = \varepsilon G_p = \frac{\varepsilon (D_p/L)\sigma cos\theta}{8\left(\frac{\mu_f (a/L)}{\rho_f} + \frac{\mu_g (1-(\frac{a}{L}))}{\rho_g}\right)} \tag{5.8}$$

where ε is the porosity (void fraction).

We assume the heat generated at the surface (bottom of the porous layer) heats the fluid in the capillaries (pores) only, and vaporization takes place inside the porous layer from the surface of the stationary menisci. The heat flux required to vaporize the liquid becomes

$$q''_{vap} = h_{fg} G_{total} = \frac{h_{fg} \varepsilon (D_p/L)\sigma cos\theta}{8\left(\frac{\mu_f (a/L)}{\rho_f} + \frac{\mu_g (1-(\frac{a}{L}))}{\rho_g}\right)} \tag{5.9}$$

For the reference case, we have $D_p \approx 20x10^{-9}\, m$, $L = 0.81x10^{-6}\, m$, $\varepsilon = 0.63$, $\sigma =$ 0.05891 N/m, $\rho_f = 958.4\, kg/m^3$, $\rho_g = 0.5975\, kg/m^3$, $\mu_f = 0.000282 \frac{kg}{m-s}$, $\mu_g =$ $0.00001227 \frac{kg}{m-s}$, $h_{fg} = 2260\, kJ/kg$.

A preliminary parametric study for a/L and θ and the above values gives the results in Tables 5-9 to 5-11 and the heat fluxes from Table 5-9 are also shown in Figure 5-29. Table 5-11 indicates that the Reynolds number is much less than 2000 therefore the laminar flow assumption is valid. From the data, we conclude that mass flux and heat flux for vaporization increase with increasing liquid to vapor ratio in the pore, and decreases with increasing θ.

Table 5-9 Heat flux q''_{vap} (kW/m2) for vaporization for different combinations of a/L and theta

	θ	45°	55°	65°	75°	85°
a/L						
0		8914	7231	5328	3263	1099
0.1		9889	8021	5910	3620	1219
0.2		11103	9006	6636	4064	1368
0.3		12657	10266	7564	4633	1560
0.4		14716	11937	8795	5386	1814
0.5		17576	14257	10505	6433	2166
0.6		21816	17696	13039	7985	2689
0.7		28752	23322	17184	10524	3544
0.8		42154	34194	25194	15429	5196
0.9		78958	64047	47191	28901	9732
1		622122	504640	371825	227713	76681

Table 5-10 Mass flux G_{total} (kg/m2-s) for different combinations of a/L and theta

	θ	45°	55°	65°	75°	85°
a/L						
0		3.94	3.20	2.36	1.44	0.49
0.1		4.38	3.55	2.62	1.60	0.54
0.2		4.91	3.98	2.94	1.80	0.61
0.3		5.60	4.54	3.35	2.05	0.69
0.4		6.51	5.28	3.89	2.38	0.80
0.5		7.78	6.31	4.65	2.85	0.96
0.6		9.65	7.83	5.77	3.53	1.19
0.7		12.72	10.32	7.60	4.66	1.57
0.8		18.65	15.13	11.15	6.83	2.30
0.9		34.94	28.34	20.88	12.79	4.31
1		275.28	223.29	164.52	100.76	33.93

Table 5-11 $Re_{p,f}$ (kg/m2-s) for different combinations of a/L and theta

	θ	45°	55°	65°	75°	85°
a/L						
0		0.0064	0.0052	0.0038	0.0024	0.0008
0.1		0.0071	0.0058	0.0043	0.0026	0.0009
0.2		0.0080	0.0065	0.0048	0.0029	0.0010
0.3		0.0091	0.0074	0.0055	0.0033	0.0011
0.4		0.0106	0.0086	0.0063	0.0039	0.0013
0.5		0.0127	0.0103	0.0076	0.0046	0.0016
0.6		0.0157	0.0128	0.0094	0.0058	0.0019
0.7		0.0207	0.0168	0.0124	0.0076	0.0026
0.8		0.0304	0.0247	0.0182	0.0111	0.0037
0.9		0.0569	0.0462	0.0340	0.0208	0.0070
1		0.4487	0.3640	0.2682	0.1642	0.0553

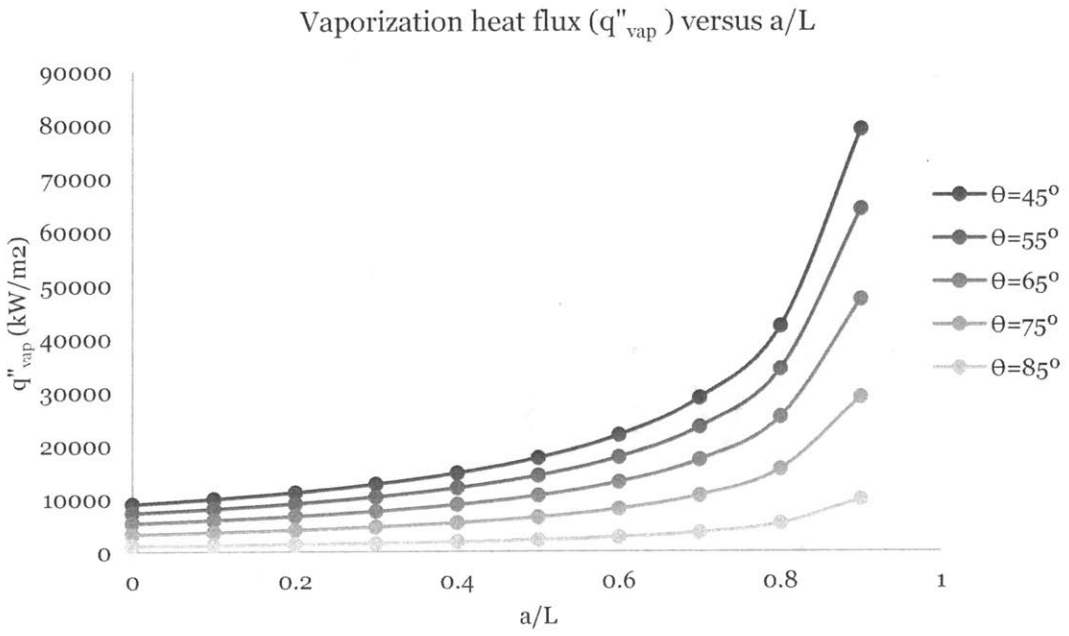

Figure 5-29 Vaporization heat flux for different combinations of a/L and theta

Finally, we also consider the permeability in a single pore which is the ability for a single pore to allow fluid to pass through it. We begin with Darcy's law

$$k_i = V_i \mu_i \frac{\Delta x_i}{\Delta p_i} \tag{5.10}$$

where the subscript i refers to the phase, either liquid or vapor. We recall that the pressure drop in each phase is given by the viscous pressure drops

$$\Delta p_i = f_i \frac{\Delta x_i}{D_p} \frac{{G_p}^2}{2\rho_i} \tag{5.11}$$

The velocity is simply $V_i = \rho_i G_p$, and the friction factor is expressed as

$$f_i = \frac{64}{Re_i} = \frac{64\mu_i}{D_p G_p} \tag{5.12}$$

Combining Equations 5.10-5.12, we obtain the permeability of a phase through a single pore as

$$k_i = \frac{D_p^2}{32} \tag{5.13}$$

Which is constant and does not depend on the phase. The effective permeability of a porous layer composed of parallel capillary tubes becomes

$$k_{eff} = \frac{\varepsilon D_p^2}{32} \tag{5.14}$$

These results suggest that for this simple model, the ability for a fluid to penetrate the porous medium should increase with both increasing pore diameter and increasing void fraction. It should be noted that this model does not account for the tortuosity of the porous layer.

The relationship between CHF and the governing parameters can be obtained from Eq. 5.9. We expect

$$q''_{CHF} \sim q''_{vap} \tag{5.15}$$

$$q''_{vap} \sim \varepsilon \tag{5.16}$$

$$q''_{vap} \sim D_p / L \tag{5.17}$$

$$q''_{vap} \sim Re_p \tag{5.18}$$

Since the vaporization heat flux is also directly proportional to the mass flux, the same trends are observed for the mass flux with respect to these parameters. The trends in Equations 5.11-5.13 capture sections of the results reported, but do not fully explain the initial increase in CHF versus D_p/L and Re_p. Further studies are therefore required to improve the accuracy of the model. To illustrate and compare the effects of porous layer thickness, pore size, and void fraction based on this model, all three are presented in Figures 5-30, to 5-32 for different ratios of a/L for the same parameter ranges used in the experimental study.

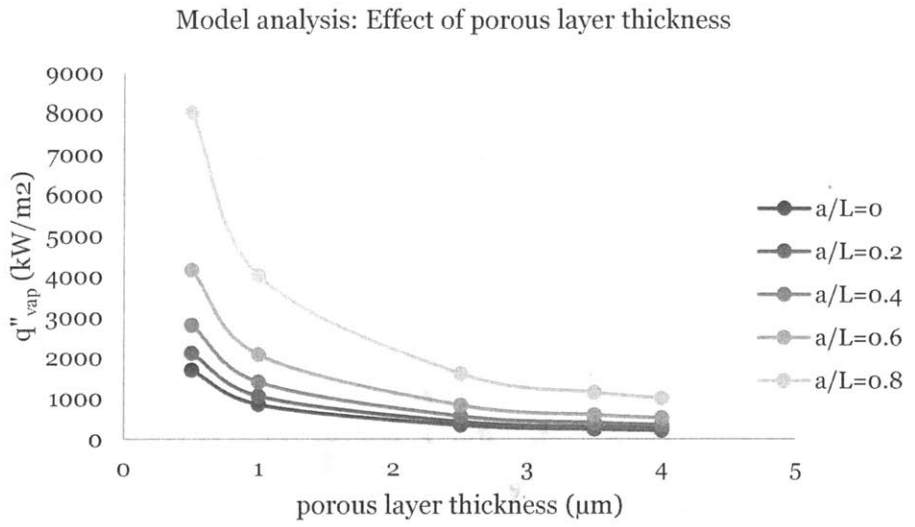

Figure 5-30 Effect of porous layer thickness based on Equation (5.9) with Θ=85°.

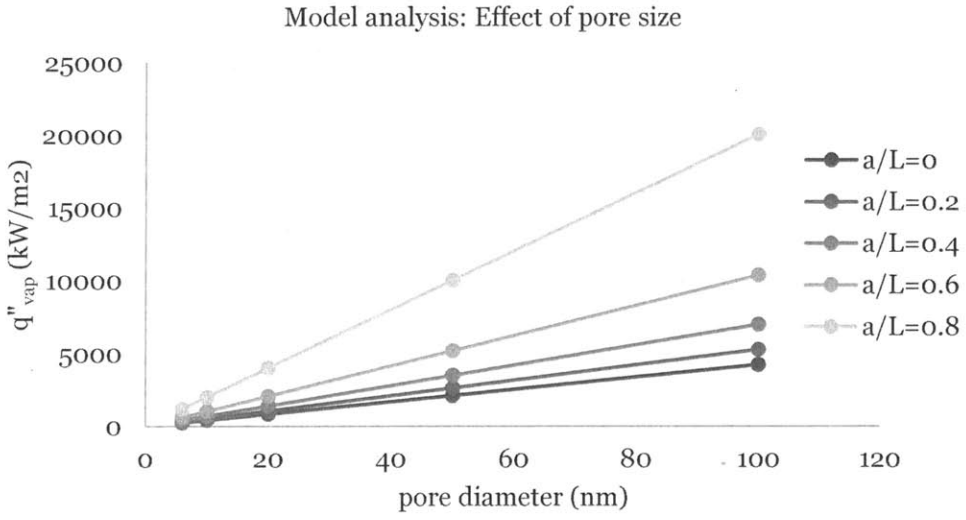

Figure 5-31 Effect of diameter based on Equation (5.9) with Θ=85°.

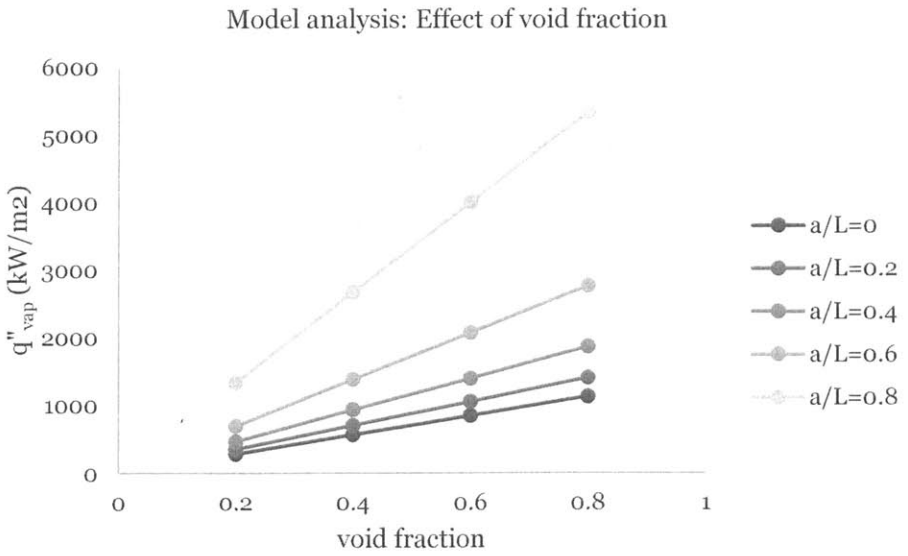

Figure 5-32 Effect of void fraction based on Equation (5.9) with Θ=85°.

6. Porous layer generated by nanofluid boiling

As previously discussed, CHF enhancement has been observed in nanofluid boiling experiments. In such cases, the nanoparticles in suspension deposit onto the boiling surface creating a porous hydrophilic coating. These highly non-uniform coatings have demonstrated very good boiling performances. In particular, Sharma [41] reported average CHF enhancements of 77% (ranging between 25% and 150% for various boiling and surface conditions) using 0.01 v% ZnO nanofluid. It is therefore of interest to reproduce these surfaces obtained by nanofluid boiling and to compare their surface characteristics and boiling performance with those fabricated using LbL techniques. The following chapter outlines the experimental procedure followed to carry out this comparative investigation.

6.1. Pool boiling experimental method

Sharma [41] performed nanofluid boiling experiments on initially smooth or sandblasted stainless steel surfaces. He investigated the dependence of the thickness of the deposited coating and CHF versus pre-boiling time. The pre-boiling time is the total time duration to which the surface undergoes boiling in the nanofluid. Once the pre-boiling phase was completed, the surface was removed and the coating is characterized using the same surface characterization methods used for the LbL surfaces. Finally, pool boiling experiments in DI water were carried out to determine their CHF performance. In Sharma's work, the best results were obtained using the initially sandblasted surfaces. For a pre-boiling time of 1 hour in DI water, the CHF value reported is 490 kW/m^2. For a pre-boiling time of 1 hour in ZnO nanofluid, the CHF value reported is 1158 kW/m^2. Thus, the addition of nanofluid during pre-boiling yielded a 136% CHF enhancement. These particular boiling conditions were therefore chosen for our investigation.

The concentrated nanofluid is manufactured by Nyacol Nano Technologies. The exact product used is Nyacol DP5370 with initial properties summarized in Table 6-1.

Table 6-1 Initial properties of Nyacol DP5370 nanofluid

Concentration	30 wt% ZnO
pH	9.5
Particle size (nm)	50 - 90

Sharma [41] fully characterized the properties of the concentrated nanofluid (density, particle size, composition, thermal conductivity, etc.). It should be noted that although the vendor specifies a particle size of 50 – 90 nm, Sharma's TEM results indicate that the particle average diameter could be closer to 15 – 25 nm.

Furthermore, he outlines the dilution calculations and process. The diluted nanofluid obtained is 0.01 v% and is sonicated for 2 minutes to ensure it is well dispersed. The final dilution has a pH ~9.76 (the acceptable pH range for the diluted nanofluid to remain colloidally stable is 8-10).

In the present study, nanofluid boiling was carried out in the same pool boiling facility described in the previous sections. The section above the ITO-sapphire heater inside the borosilicate tube is filled with nanofluid, and the rest of the facility is filled with tap water. The water contained in the entire facility is initially preheated to saturation temperature. The nanofluid is then boiled at 250 kW/m^2 for 1 hour.

To perform CHF tests, the nanofluid must first be emptied from the borosilicate tube section and replaced with DI water. The tests are then carried out as discussed in the previous sections.

For this study, 2 samples were first boiled in nanofluid and used for characterizing the surface features. Since profilometry is a destructive method, 2 additional samples are boiled in nanofluid for the CHF tests.

6.2. Results

6.2.1. Surface Analysis

Figure 6-1 shows images of the heater during nanofluid boiling and post-nanofluid boiling. It can be seen from the post-boiling image that the nanoparticle deposition is thicker at the nucleation sites, producing a surface coating much less uniform than those obtained from layer-by-layer deposition.

The thickness, roughness, and static contact angle are summarized in Table 6-2. For each surface feature (thickness, roughness, and wettability), at least six measurements were taken since the surface was significantly non-uniform.

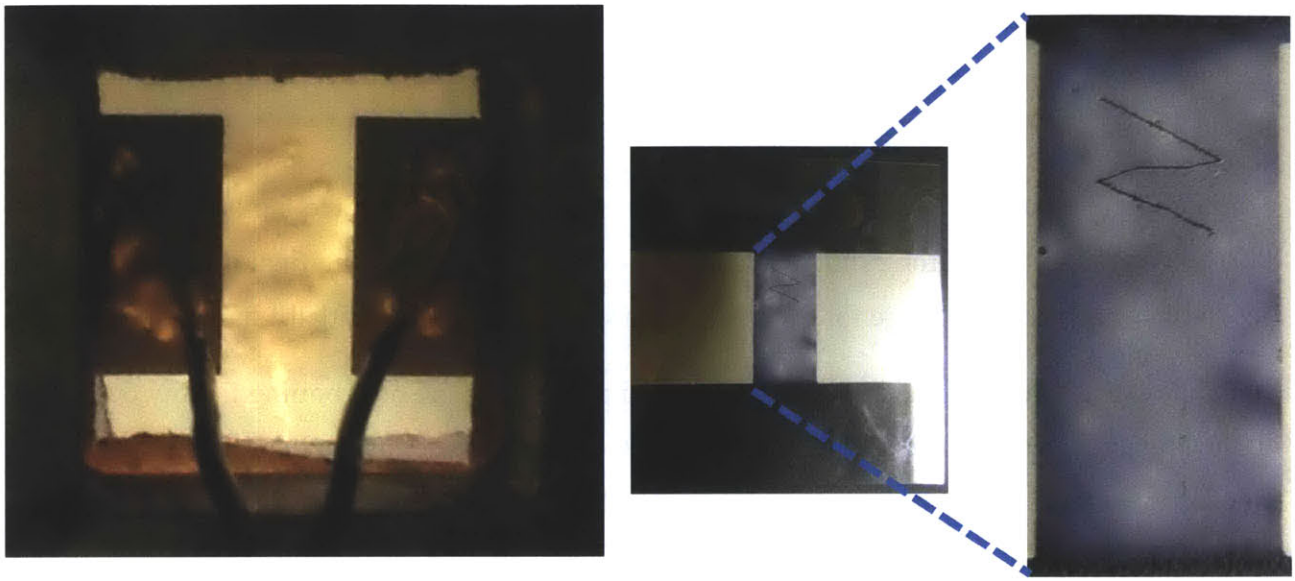

Figure 6-1 Images of heater during nanofluid boiling (left) and post-nanofluid boiling (right). The right image also shows the scratch made to obtain thickness data via profilometry.

Table 6-2 Summary of surface feature measurements obtained from stylus profilometer and goniometer for surfaces created by nanofluid boiling.

Sample #	Average Thickness (μm)	Thickness Standard Deviation (%)	Average Roughness- R_a (μm)	Roughness Standard Deviation (%)	Static Contact Angle
1	9.00	22.7	2.49	28.6	<5°
2	9.68	17.4	2.77	16.7	<5°
average	9.34	-	2.63	-	<5°

The void fraction of the coating could not be measured via ellipsometry for two reasons. First, the coatings are on the order of several microns in thickness but ellipsometry is used for thin films with thicknesses <500nm. Second, the surfaces are deposited on sapphire which is a transparent substrate that causes the ellipsometer signal to diffuse significantly.

SEM images were obtained and provide additional insight on the pore size and the void fraction of the coatings and are shown in Figure 6-2.

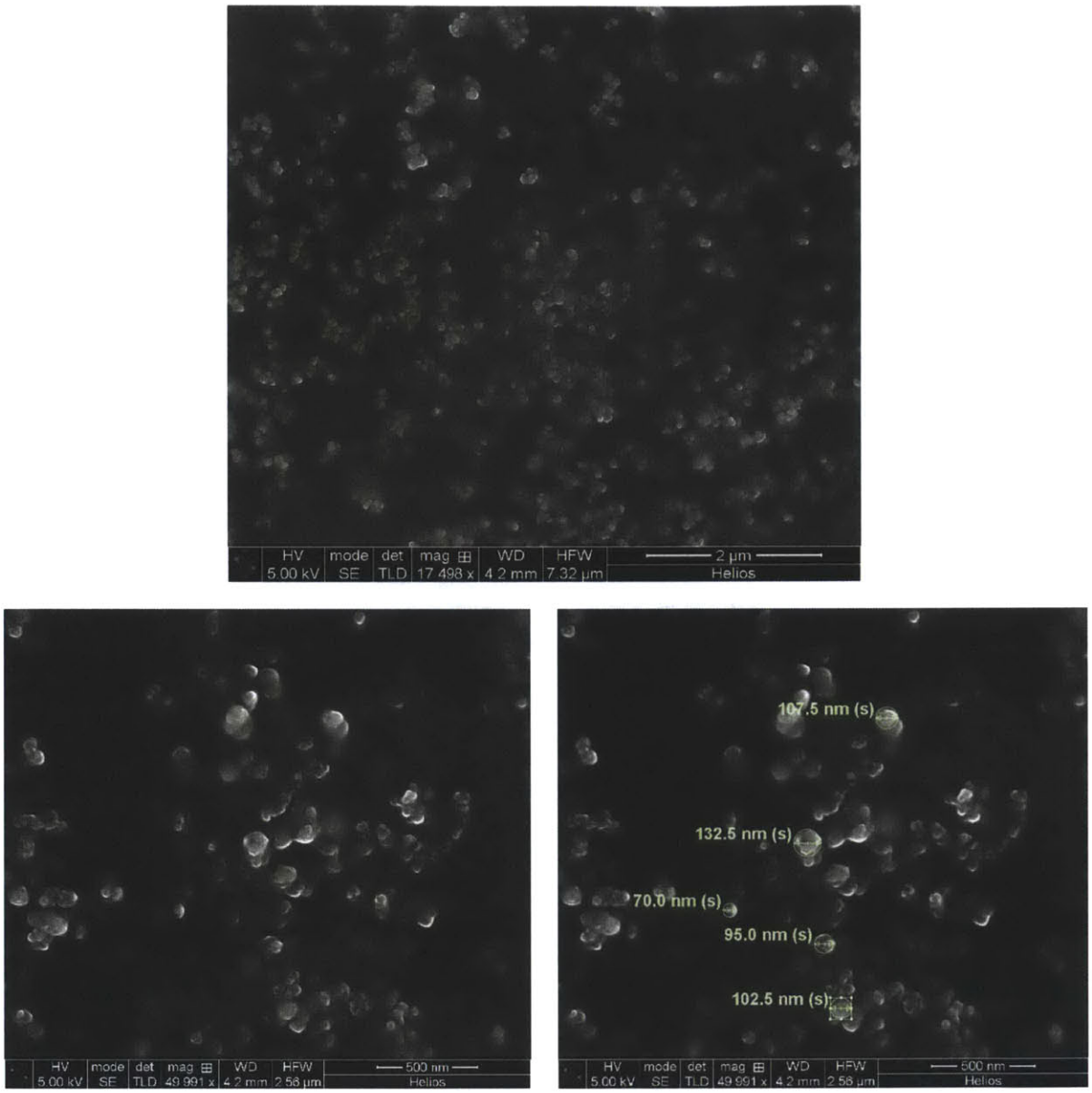

Figure 6-2 SEM/FIB images at different magnifications of surface coatings obtained from nanofluid boiling.

Since the surfaces are extremely rough, the visible particles are those at the top of the coating. The darker regions in the images are where the particles are far out of plane of view, deeper inside the porous structure. Due to the very irregular structure, it is difficult to estimate the size of the pores and the void fraction from these images. The structure also appeared to collapse from the focused ion beam therefore no cross-section FIB images were obtained. It would be of great value to obtain more SEM images and analyze them using an image processing program such as ImageJ to calculate quantitatively the size of the pores or to obtain a very rough estimate of the porosity. This was however beyond the scope of this research.

6.2.2. Boiling curves and CHF results

Table 6-3 summarizes the CHF results obtained for the nanofluid-generated surfaces. The average CHF is 2167 kW/m^2. The enhancement with respect to a bare heater is 135% which is very significant. The boiling curves, Figures 6-4 and 6-5, in each test follow the same shape, but there is a relatively large horizontal shift between the two boiling curves. In addition, the results suggest a relatively high onset of nucleate boiling temperature ~120°C. Furthermore, the results are similar to those obtained with the highest performing LbL surface. One of the curves is in fact nearly identical, up until the point where there appears to be a reversal in the trend for the nanofluid-generated surface since the temperature of the surface decreases as the heat flux is increased beyond ~1750 kW/m^2.

Table 6-3 Critical heat flux values for surfaces created by nanofluid boiling

Sample #	Average CHF (kW/m^2)
1	2200
2	2133
average	2167

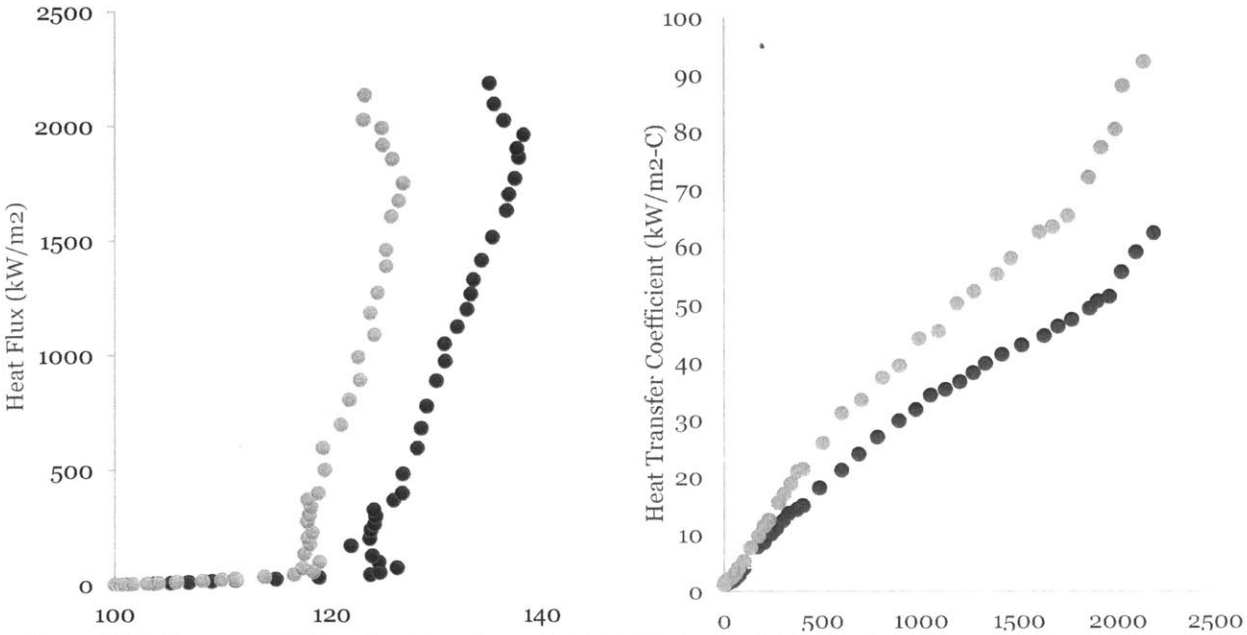

Figure 6-4 Boiling curve (left) and heat transfer coeffieint (right) for nanofluid-generated surfaces. Maximum measurement uncertainties are: T≈2.8%, q"≈2%, and HTC≈11%.

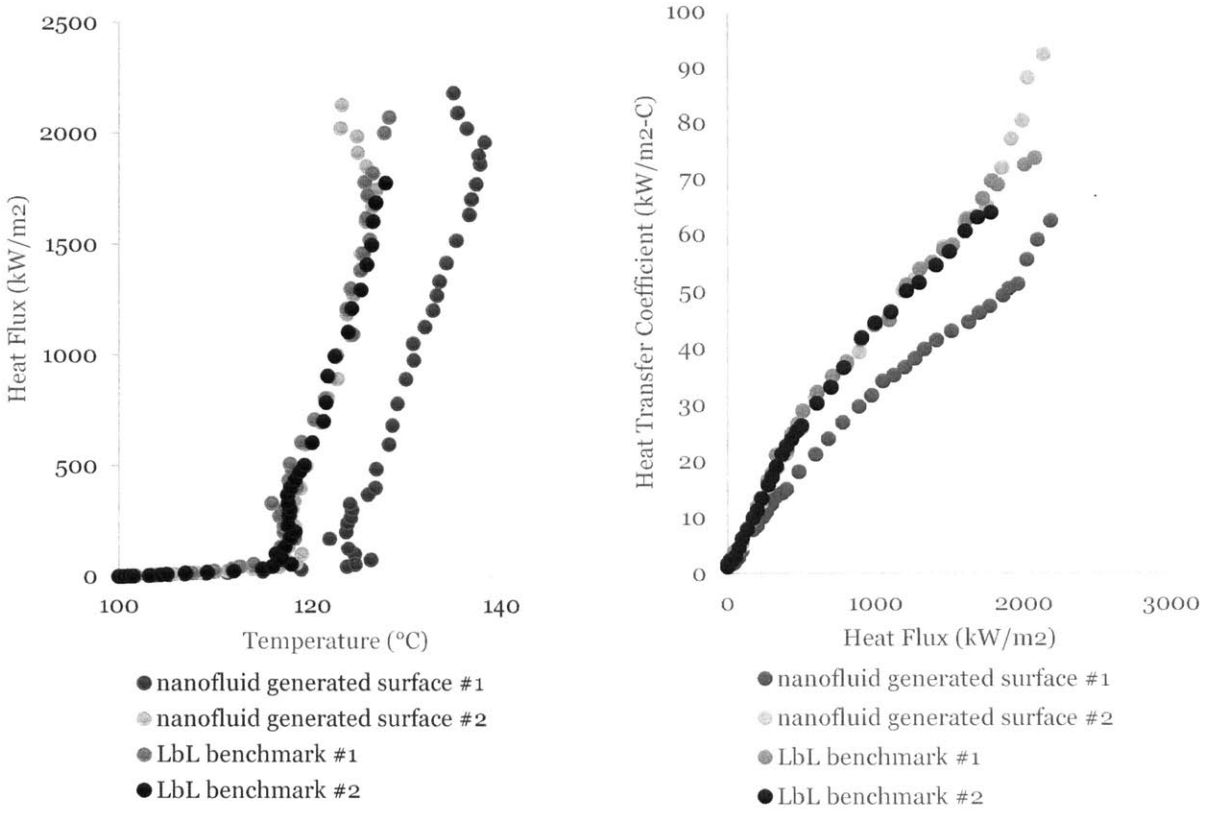

Figure 6-5 Boiling curve (left) and heat transfer coeffieint (right) for nanofluid-generated surfaces compared with LbL benchmark case (LbL surface with highest CHF enhancement). Maximum measurement uncertainties are: T≈2.8%, q"≈2%, and HTC≈11%.

6.3. Comparison with LbL surfaces

In the following section, the results obtained from nanofluid boiling are discussed and compared with those obtained from LbL. In particular, the results are compared with the surface created by LbL which displayed the highest CHF performance. The surface features and CHF performance of this benchmark are summarized in Table 6-4.

Table 6-4 Summary of LbL surface features with highest CHF value

Particle Size (nm)	# of bilayers	Layer Thickness (μm)	R_a (nm)	Void Fraction (%)	Static Contact Angle	Average CHF (kW/m^2)
20	58	2.0	92	63.4	<5°	1973

Table 6-5 presents a comparative analysis between the surface features and CHF for the nanofluid surfaces and the benchmark case. The thickness is 5 times greater and the roughness is 29 times greater for the nanofluid boiled surfaces with respect to the benchmark and the wettability is identical in both cases. Although the features are significantly enhanced, the CHF value is only 10% greater for the nanofluid boiled surfaces. The CHF value is therefore almost identical for surfaces with a completely different set of surface features. Based on the thickness study presented in Chapter 5, one would expect the CHF value to be much lower since the thickness is far beyond the peak observed in the results of the study. However, the porous structure is also entirely different since the roughness and pore size are not the same and the results therefore cannot be directly compared with those obtained from the previous section. Nevertheless, the nanofluid-generated coatings are much more open porous structures with more interconnected pores. Based on the physical mechanism describing CHF enhancement proposed in Chapter 5, the results suggest that the nanofluid-generated coatings promote wicking and vapor escape better than the LbL-engineered coatings.

Table 6-5 Comparison of surface features and CHF for benchmark case (20nm-particles, 2 microns thick, ~60% porosity) and nanofluid boiled surfaces

Surface feature	Enhancement with respect to benchmark LbL surface (%)
Thickness	376
Roughness	2754
Pore size	n/a
Wettability	0
CHF	10

7. Conclusion

A separate effect investigation was carried out to determine the effects of the porous layer thickness, pore size, and void fraction on boiling heat transfer and critical heat flux. Layer-by-layer (LbL) deposition was used to manufacture the porous surfaces. The fabrication technique was adapted and refined for this application using precise surface characterization methods. CHF appeared to increase with increasing thickness to some maximum CHF value where the thickness was optimal and then decreased as the thickness was increased beyond this point. Similarly, CHF also reached a peak value as the pore size was gradually increased and then decreased significantly. Finally, a new method was developed to vary the void fraction based on layer-by-layer assembly techniques. The new method was then used for the study of the effect of void fraction on CHF. The results indicated that CHF increases with increasing void fraction over the range of void fractions studied. The highest enhancement observed was 114% and was achieved with a 2μm-thick, 20 nm-diameter particles, 63% void fraction, smooth and superhydrophilic coatings. The results of the separate effects study suggest that CHF depends on the capillary pressure and the viscous pressure drops. A preliminary model based on these results was developed which captures the decreasing CHF trend with increasing layer thickness, and the increasing CHF trend with increasing pore size and void fraction.

A parallel investigation was carried out to compare the nanoengineered surfaces fabricated using LbL deposition with those obtained via nanofluid boiling. Nanofluid generated coatings were created on the same substrates as those used in the separate effects study and their surface features were characterized. Boiling tests in water were then carried out to determine their boiling performance. The nanofluid generated coatings performed approximately the same as the best nanoengineered coatings. The open and interconnected pore structure appeared to be responsible for the excellent boiling performance.

The results of these studies should provide insight into the effects of surface features on CHF and to further understand the underlying physical mechanisms. They should also allow to optimize the surface characteristics to enhance CHF which is beneficial to a wide variety of industries. Further research into understanding and improving CHF enhancement should include improving surface feature characterization techniques and expanding the test matrix to include a broader range of thicknesses, pore sizes, and void fractions. A method to increase void fraction would also greatly

improve the general understanding of this effect. Different pore shapes can be explored. Design of experiment techniques such as the Taguchi method can be used to optimize the combination of parameters to obtain the greatest CHF enhancement. Finally, a model which captures the trend of each parameter over the entire ranges investigated should be developed.

References

[1] J. G. Collier and J. R. Thome, *Convective boiling and condensation*: Oxford University Press, 1994.

[2] J. Buongiorno, *et al.*, "Nanofluids for enhanced economics and safety of nuclear reactors: An evaluation of the potential features, issues, and research gaps," *Nuclear Technology,* vol. 162, pp. 80-91, 2008.

[3] R. L. Webb, "The evolution of enhanced surface geometries for nucleate boiling," *Heat Transfer Engineering,* vol. 2, pp. 46-69, 1981.

[4] K.-H. Chu, *et al.*, "Structured surfaces for enhanced pool boiling heat transfer," *Applied Physics Letters,* vol. 100, p. 241603, 2012.

[5] S. Kim, *et al.*, "Surface wettability change during pool boiling of nanofluids and its effect on critical heat flux," *International Journal of Heat and Mass Transfer,* vol. 50, pp. 4105-4116, 2007.

[6] H. F. O'Hanley, "Separate effects of surface roughness, wettability and porosity on boiling heat transfer and critical heat flux and optimization of boiling surfaces," Master Thesis, Massachusetts Institute of Technology, 2012.

[7] S. G. Bankoff, "Ebullition from solid surfaces in the absence of a pre-existing gaseous phase.," *Trans. ASME,* vol. 79, 1957.

[8] W. Kast, "Bedeutung der Keimbildung und der instationären Wärmeübertragung für den Wärmeübergang bei Blasenverdampfung und Tropfenkondensation," *Chemie Ingenieur Technik,* vol. 36, pp. 933-940, 1964.

[9] N. Todreas and M. Kazimi, "Nuclear Systems I: Thermal Hydraulic Fundamentals.(1993)," ed: Taylor & Francis.

[10] (2010, 2013-11-17). *Pool Boiling Regimes*. Available: http://www.thermalfluidscentral.org/encyclopedia/index.php/Pool_Boiling_Regimes

[11] S. G. Liter and M. Kaviany, "Pool-boiling CHF enhancement by modulated porous-layer coating: theory and experiment," *International Journal of Heat and Mass Transfer,* vol. 44, pp. 4287-4311, 2001.

[12] H. O'Hanley, *et al.*, "Separate effects of surface roughness, wettability, and porosity on the boiling critical heat flux," *Applied Physics Letters,* vol. 103, p. 024102, 2013.

[13] V. Borishanski, *et al.*, "Investigation of heat transfer during nucleate boiling of liquids," *Convection Heat Transfer and Hydrodynamics in Two-Phase and Single-Phase Flows,* pp. 71-104, 1964.

[14] S. G. Kandlikar, "A theoretical model to predict pool boiling CHF incorporating effects of contact angle and orientation," *Journal of heat transfer,* vol. 123, pp. 1071-1079, 2001.

[15] Y. V. POLEZHAEV and S. Kovalev, "Modelling heat transfer with boiling on porous structures," *Thermal engineering,* vol. 37, pp. 617-621, 1990.

[16] J. Ramilison, *et al.*, "Surface factors influencing burnout on flat heaters," *Journal of heat transfer,* vol. 114, pp. 287-290, 1992.

[17] P. Berenson, "Experiments on pool-boiling heat transfer," *International Journal of Heat and Mass Transfer,* vol. 5, pp. 985-999, 1962.

[18] M. Jakob, *Heat Transfer*. New York: Wiley, 1949.

[19] S. Kim, *et al.*, "Effects of nanoparticle deposition on surface wettability influencing boiling heat transfer in nanofluids," *Applied Physics Letters,* vol. 89, p. 153107, 2006.
[20] G.-S. Hwang and M. Kaviany, "Critical heat flux in thin, uniform particle coatings," *International Journal of Heat and Mass Transfer,* vol. 49, pp. 844-849, 2006.
[21] J. Kim, *et al.*, "Mechanism of nucleate boiling heat transfer enhancement from microporous surfaces in saturated FC-72," *Journal of heat transfer,* vol. 124, pp. 500-506, 2002.
[22] H. S. Ahn, *et al.*, "Pool boiling experiments on multiwalled carbon nanotube (MWCNT) forests," *Journal of heat transfer,* vol. 128, pp. 1335-1342, 2006.
[23] S. Ujereh, *et al.*, "Effects of carbon nanotube arrays on nucleate pool boiling," *International Journal of Heat and Mass Transfer,* vol. 50, pp. 4023-4038, 2007.
[24] R. Chen, *et al.*, "Nanowires for enhanced boiling heat transfer," *Nano letters,* vol. 9, pp. 548-553, 2009.
[25] D. Lee, "Surface engineering using layer-by-layer assembly of pH-sensitive polymers and nanoparticles," Massachusetts Institute of Technology, 2007.
[26] J. Cho, *et al.*, "Fabrication of highly ordered multilayer films using a spin self-assembly method," *Advanced Materials,* vol. 13, pp. 1076-1078, 2001.
[27] J. B. Schlenoff, *et al.*, "Sprayed polyelectrolyte multilayers," *Langmuir,* vol. 16, pp. 9968-9969, 2000.
[28] S. S. Shiratori and M. F. Rubner, "pH-dependent thickness behavior of sequentially adsorbed layers of weak polyelectrolytes," *Macromolecules,* vol. 33, pp. 4213-4219, 2000.
[29] D. Yoo, *et al.*, "Controlling bilayer composition and surface wettability of sequentially adsorbed multilayers of weak polyelectrolytes," *Macromolecules,* vol. 31, pp. 4309-4318, 1998.
[30] J. P. DeRocher, *et al.*, "Layer-by-layer assembly of polyelectrolytes in nanofluidic devices," *Macromolecules,* vol. 43, pp. 2430-2437, 2010.
[31] D. Lee, *et al.*, "Multilayers of oppositely charged SiO2 nanoparticles: effect of surface charge on multilayer assembly," *Langmuir,* vol. 23, pp. 8833-8837, 2007.
[32] D. Lee, *et al.*, "pH-dependent structure and properties of TiO2/SiO2 nanoparticle multilayer thin films," *Chemistry of materials,* vol. 19, pp. 1427-1433, 2007.
[33] F. Ç. Cebeci, *et al.*, "Nanoporosity-driven superhydrophilicity: a means to create multifunctional antifogging coatings," *Langmuir,* vol. 22, pp. 2856-2862, 2006.
[34] Z. Liang, *et al.*, "Covalent Layer-by-Layer Assembly of Conjugated Polymers and CdSe Nanoparticles: Multilayer Structure and Photovoltaic Properties," *Advanced Functional Materials,* vol. 16, pp. 542-548, 2006.
[35] R. Iler, "Multilayers of colloidal particles," *Journal of Colloid and Interface Science,* vol. 21, pp. 569-594, 1966.
[36] Y. Takata, *et al.*, "Evaporation of water drop on a plasma-irradiated hydrophilic surface," *International journal of heat and fluid flow,* vol. 25, pp. 320-328, 2004.
[37] E. C. Forrest, "Nanoscale modification of key surface parameters to augment pool boiling heat transfer and critical heat flux in water and dielectric fluids," Massachusetts Institute of Technology, 2009.
[38] FEI.com. (2014), *Helios NanoLab 600i.* Available: http://www.fei.com/products/dualbeams/helios-nanolab-600i-product/?ind=MS
[39] ScienTec. *KLA Tencor - P-16 + Surface Profiler.* Available: http://90plan.ovh.net/~scientec/contenu_en.php?cat=kla-tencor&sub=P16

[40] B. A. Phillips, "Nano-engineering the boiling surface for optimal heat transfer rate and critical heat flux," Massachusetts Institute of Technology, 2011.
[41] V. I. Sharma, "Experimental investigation of effects of surface roughness, wettability and boiling-time on steady state and transient CHF for nanofluids," Massachusetts Institute of Technology, 2012.